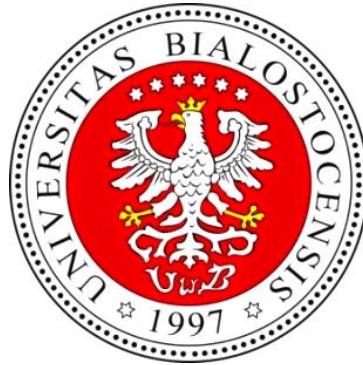


University of Bialystok

Faculty of Physics



**Statics and Dynamics of Magnetization in:
Patterned Permalloy and Ion-Irradiated Co
and FeAl Nanostructures**

Nadeem Tahir

Promotor: dr hab. Ryszard Gieniusz

Bialystok, 2015

Abstract

The understanding of magnetization reversal behavior and spin wave excitation spectrum in the micro- and nanometer length scale of ferromagnetic elements has attracted much attention in the recent years due to discoveries of fundamental new physics and their potential applications such as magneto-optical devices, magnetic recording media, and sensors. Especially interesting are patterned magnetic nanostructures, such as magnonic crystals (MCs), metamaterials where magnetic properties are modulated in periodic manners. In this dissertation, three topics related to the modification of magnetic properties were distinguished: through patterning (removal of magnetic material) in permalloy (Py) and ion irradiation in $\text{Fe}_{60}\text{Al}_{40}$ and cobalt (Co) thin films. These samples were studied by combining different experimental techniques such as magneto-optical Kerr effect microscopy (MOKE) and three spectrometries: Brillouin light scattering (BLS), X-band ferromagnetic resonance (FMR) and vector network analyzer ferromagnetic resonance (VNA-FMR). Initial chemically ordered B2-phase $\text{Fe}_{60}\text{Al}_{40}$ (paramagnetic) thin films was transformed to chemically disordered A2-phase (ferromagnetic) by Ne^+ ions-irradiations with varying energies in the range of 0-30 keV (keeping fluence constant 6×10^{14} ions cm^{-2}). The relationship of effective thickness (defined by energy of ions) with different magnetization processes and evolution of magnetic domains were sorted out. Spin wave excitations at Damon-Eshbach (DE) and standing spin waves (SSW) modes were identified in relation to ferromagnetic layer thickness/(energies of the irradiated ions). Depth varying magnetization set the pinning mechanisms for spin waves which accounts additional mode across A2/B2-phase boundary. The analytical calculations were in good agreement with the experimental results where spin-wave modes were directly related to the effective ferromagnetic thickness. In 1D reprogrammable stripe patterned $\text{Fe}_{60}\text{Al}_{40}$ sample, the existence of binary re-programmable magnetization configurations, demonstrated the possibility to apply disorder induced ferromagnetic structures for creation of MCs. Influence of complexity of the patterned Py nanostructures from square antidot lattice to wavelike on the magnetization reversal, magnetic anisotropies, and spin wave excitations spectra was studied. Magnetization reversal was strongly depended on the patterned geometry. Different spin waves modes including fundamental, bulk, and edge modes were distinguished. Experimental results were well reproduced by MuMax calculations. Ga^+ ions were employed to modify magnetic anisotropy in ultrathin Pt/Co/Pt films. Ions fluence driven changes in spin wave excitations with

oscillating behavior (connected with magnetic anisotropy changes) were observed. A new type of MCs can be fabricated based on magnetic anisotropy modulation by selecting proper fluence profile.

Contents

Abstract	2
Contents	4
Glossary	7
1. Introduction	8
1.1. Introduction.....	9
1.2. Objectives and structure of the thesis.....	11
2. Theory	13
2. Theory.....	14
2.1. Introduction to Magnetism.....	14
2.1.1. Origin of Magnetic Moment.....	14
2.2. Magnetic interactions.....	17
2.2.1. Magnetic dipolar interaction.....	17
2.2.2. Exchange interaction.....	17
2.2.2.1. Direct Exchange.....	18
2.2.2.2. Indirect exchange in Metals.....	20
2.2.2.3. Indirect exchange in ionic solids: superexchange.....	21
2.2.2.4. Double exchange.....	22
2.2.2.5. Anisotropic exchange interaction.....	23
2.3. The Energy Functional of a Magnet.....	24
2.3.1. Zeeman Energy.....	24
2.3.1.1. Magnetocrystalline anisotropy.....	24
2.3.2. Anisotropy Energy.....	25
2.3.2.1. Demagnetizing Energy.....	25
2.3.2.2. Surface and interface anisotropy.....	27
2.3.3. Exchange Energy.....	29
2.4. Magnetic Domains.....	29
2.4.1. Domain walls.....	30
2.5. Magnetization processes.....	31
2.5.1. Magnetic parameters.....	31
2.5.2. Magnetization reversal process.....	33
2.6. Magnetization Dynamics.....	34
2.7. Spin waves.....	36

3. Experimental	41
3. Experimental	42
3.1. Sample preparation.....	42
3.1.1. Fabrication of thin films	42
3.1.1.0. Chemical deposition	43
3.1.1.1. Physical processes	43
3.1.2. Tuning magnetic properties through ion irradiations	46
3.1.2.1. Establishing ferromagnetism through disorder.....	47
3.1.2.2. Tailoring the magnetic anisotropy.....	47
3.1.3. Patterning of nanostructures	48
3.1.3.1. Magnetic Patterning through ion irradiation	49
3.1.3.2. Magnetic patterning through photolithography	50
3.2. Statics measurements	53
3.2.1. Magneto-optical Kerr effect (MOKE).....	53
3.2.2. Magneto-optical millimagnetometer.....	55
3.2.3. Kerr Microscopy.....	56
3.2.3.1. The illumination Path	57
3.2.3.2. Domain observation	59
3.2.4. Study of magnetization reversal processes.....	60
3.3. Dynamics measurements	61
3.3.1. Ferromagnetic Resonance (FMR)	61
3.3.1.1. Experimental arrangement of FMR.....	63
3.3.2. Brillouin Light scattering (BLS) spectroscopy.....	65
3.3.2.1. Experimental arrangement.....	68
3.3.2.2. Tandem Fabry-Pérot (TFP) interferometer.....	69
4. Results and Discussions	73
4.1. Fe₆₀Al₄₀	74
4.1. Fe ₆₀ Al ₄₀	75
4.1.1. Sample fabrication.....	75
4.1.1.1. Uniformly irradiated thin films	75
4.1.1.2. Fabrication of 1D stripes	77
4.1.2. Statics measurements	80
4.1.3. Uniform films	80

4.1.3.1. Magnetization state.....	80
4.1.3.2. Magnetization reversal study.....	82
4.1.3.2. Magnetization reversal in reprogrammable 1D stripe	86
4.1.3.2.1. Magnetization reversal for uniformly irradiated stripe.....	86
4.1.3.2.2. Magnetization reversal study in 1D reprogrammable stripe.....	87
4.1.3. Study of magnetization dynamics	88
Summary	99
4.2. Patterned (antidot lattices) Py	101
4.2. Nanopatterns of Py	102
4.2.1. Sample fabrication.....	102
4.2.2. Structural analysis	103
4.2.2.1. SEM analysis.....	104
4.2.2.2. AFM analysis	105
4.2.3. Statics measurements	106
4.2.4. Dynamics measurements.....	117
4.2.4.1. FMR study.....	117
Summary	129
4.3. Thin films of Pt/Co/Pt	131
4.3.1. Sample fabrication:.....	132
4.3.2. Statics measurements	133
4.3.2.1. PMOKE measurements	133
4.3.2.2. LMOKE measurements.....	137
4.3.3. Dynamics measurements.....	138
Summary	144
5. Conclusions	145
6. References	147
6. List of publications	157
Acknowledgements.....	160

Glossary

Acronyms

Symbols

BLS	Brillouin Light Scattering	H_c	Coercive field
FMR	Ferromagnetic Resonance	H_{1eff}	Effective field
FWHM	Full width at half maximum	m_r	Magnetization remanence
hf	High frequency	\mathbf{B}	Vector of magnetic induction
LL	Landau-Lifshitz	d	thickness
LLG	Landau-Lifshitz-Gilbert	d_{eff}	Effective thickness
MOKE	Magneto-Optical Kerr Effect	f	Precessional frequency
LMOKE	Longitudinal Magneto-Optical Kerr Effect	J	Exchange integral
PMOKE	Perpendicular Magneto-Optical Kerr Effect	$M = M/M_S$	Reduced magnetization vector
MSSW	Magnetostatic Surface Wave	M_S	Saturation magnetization
MR	Magnetization reversal	$\omega = 2\pi f$	Angular frequency
Py	Permalloy ($Ni_{81}Fe_{19}$)	H_{sat}	Saturation field
VNA	Vector network analyzer	K_u	Uniaxial anisotropy
1D	One dimensional	M_{eff}	Effective magnetization
2D	Two dimensional	H_R	Reversal field
MCs	Magnonic crystals	$t_{1/2}$	Relaxation time
Antidot lattice	ADL	λ_{laser}	Wavelength of laser
EBL	Electron beam lithography	g	g -factor
CMOS	complementary metal-oxide-semiconductor	γ	gyromagnetic ratio
Spin waves	SW	μ_B	Bohr magneton
Py	Permalloy	μ_0	Permeability
DUV	Deep ultraviolet	A	Exchange constant
DMI	Dzyaloshinsky-Moriya interaction	α	Damping constant
DE	Damon Eshbach	K	Anisotropy constant
SSW	Standing spin waves	l_{ex}	Exchange length
PMA	Perpendicular magnetic anisotropy	f_{DE}	Frequency of DE mode
GMR	Giant magnetoresistance	f_{SSW}	Frequency of standing spin waves
CVD	Chemical vapor deposition	q_{\perp}	Wave-number across the film thickness
PVD	Physical vapor deposition	p_d	Pinning at certain depth
PLD	Pulse laser deposition		
MBE	Molecular beam epitaxy		
LEED	Low energy electron diffraction		
RHEED	Reflection high energy electron diffraction		
UHV	Ultra-high vacuum		
FIB	Focus ion beam		
VNA-FMR	Vector network analyzer-ferromagnetic resonance		

1. Introduction

1.1. Introduction

The modern research on fundamental properties of materials is increasingly driven by their anticipated potential for technological applications. Due to their intricate nanostructures, extremely small length scale, low dimensionality, and interplay among constituents, they often present new and enhanced properties over their parent bulk materials. Recent progress on magnetism and magnetic materials has made nanostructures a particularly interesting class of materials for both scientific and technological applications such as sensors, patterned media, and novel magnetic properties [Mar03, She02, Bad06, Ake04, Stu03, Sko03]. Magnetic nanostructures can be fabricated by means of many advances fabrication techniques, e.g. electron beam lithography (EBL), deep ultraviolet lithography, focused ion beam patterning or ion beam etching, etc..

By modulating magnetic thin film properties in proper order, one can form one dimensional (1D), two dimensional (2D) magnonic crystals (MCs)-a new class of metamaterials with periodically modulated magnetic properties which due to unique properties of spin waves can offer new functionalities that are currently unavailable in e.g. photonic and electronic devices [Gie05, Gie07, Her04, Khi07, Khi08, Lee08, Pod05, Pod06, and Vas07] as magnonic devices are easily manipulated by the applied magnetic field. Moreover, magnetic nano-structures are non-volatile memory elements, and therefore, their integration will enable programmable devices with the ultrafast re-programming at the sub-nanosecond time scale. At remanence, a mono-domain nanomagnet with uniaxial magnetic anisotropy has two energy minima for opposing orientations of the magnetization \mathbf{M} collinear with the easy axis. MCs can be also be designed via different quasi-static magnetic states of subcomponents of an MC or magnonic device. In general, to demonstrate the rich technological potential of magnonics, one has to design and to build nanoscale functional magnonic devices, in particular those suitable for monolithic integration into existing complementary metal-oxide-semiconductor (CMOS) circuits. In magnetic data storage media magnetic nano-structures have already been combined with nano- electronics (e.g. in read heads and magnetic random access memories) and optics (e.g. in magneto-optical disks). Hence, magnonic devices offer the integration with microwave electronics and photonic devices at the same time. Since for all practically relevant situations (at the GHz to THz frequency range), the wavelength of spin waves is several orders of magnitude shorter than

that of electromagnetic waves, magnonic devices offer better prospects for miniaturization at these frequencies.

Ferromagnetic metals show a spin wave (SW) damping that leads to decay lengths of typically several $10\mu\text{m}$. SW propagation in un-patterned Py was resolved over $80\mu\text{m}$ [Kru10]. Along with Py nanostructures (dots), antidots structures (the reverse of isolated nanostructures) form another class of magnetic nanostructures in which arrays of holes are embedded into contiguous magnetic materials. Antidots are artificially engineered “defects” in an otherwise continuous film. The antidote lattice (ADL) has also been proposed as a competitor for high density storage media, with characteristics of high stability while avoiding the superparamagnetic limit [Cow97]. In the antidot lattices, spin waves propagate through the continuous ferromagnetic medium between the antidots and have much higher propagation velocity and longer propagation distance as compared to other for type of MCs such as lattice formed by dots or stripes. Due to the advances in the fabrication technology the proper arrangement of these antidots can lead to change in magnetic properties of the thin films in controllable manner [Ade08]. Such structures can be regarded as an example of two-dimensional (2D) artificial MCs [Khi08, Sch08]. Effect of antidot shape (square, circular, elliptical), size, interspacing distance, and arrangement (square lattice, honeycomb lattice, rhombic lattice) on statics (magnetization reversal), and dynamics of magnetization (spin waves) have been carried out by different techniques [Tri10, Tac10, Wan06, Gue02, Gue03, Yu03, Man15, Len11, and Dem13]. There is still quest to know: how ADL structures tune the magnetization reversal, and spin wave excitation in geometrically perturbed magnetic thin films.

It has been quite known that magnetic properties of the magnetic thin films can be further tailored by processing capabilities such as ion irradiations, which have proven itself a powerful tool to modify and tune magnetic properties [Fas04, Fas08 and Maz12]. In general ion induced changes are related to the deformation of the chemical structures, hence the magnetic phase which lowers the magnetic patterning which is highly important for bit patterned media. Conversely ions irradiation can be used to induce ferromagnetism in certain alloys through creating chemical disorder in such system [Fas08a, Bal14, Tah14, Tah15, Tah15a, Men09 and Sor06].

1.2. Objectives and structure of the thesis

Within the framework of this thesis, detailed study to understand the effects of geometry of the nano-patterns, and ion irradiation on the statics and dynamics of magnetization in Py antidots structures, and irradiated $\text{Fe}_{60}\text{Al}_{40}$ and Pt/Co/Pt thin films respectively is carried out. The goals of the thesis were focused to the studies of:

1. Influence of complex antidot lattice geometry (from square lattice to wave-like patterns) on magnetic anisotropy, magnetization reversal mechanisms, and spin wave excitation spectra.
2. Effect of irradiation energy driven modification in $\text{Fe}_{60}\text{Al}_{40}$ thin films on combined magnetic properties: static (evolution of magnetic domain structures, magnetization reversal mechanisms) and dynamic (spin waves excitations). A very recently it was demonstrated that discrete magnetic patterning can be achieved in such system [Bal14], which makes this it a potential candidate for MCs.
3. Role of 30 keV Ga^+ -ions fluence on spin wave excitations in irradiated Pt/Co/Pt ultrathin films. Recently [Maz12] has reported possibilities of induced magnetic anisotropy modifications through ion irradiation fluence.

This thesis is divided into seven chapters (introduction being the first chapter). In this chapter brief introduction related to the importance of magnetic nanostructures, their potential use in scientific research and depth of the pertinent issues has been presented.

Chapter 2 provides brief information about the magnetic moment, magnetic interactions, magnetic anisotropy, magnetic domains, magnetization process, magnetization dynamics, and spin waves.

Chapter 3 comprises the overview of the experimental techniques such as sample fabrication, and their characterization.

Chapter 4 comprises the results and discussion. This chapter is further divided into sub-chapters depending on our study for different considered systems.

Chapter 4.1 We will show how energy of the irradiated ions is responsible for different magnetization reversal processes and evolving of domains structure. We shall demonstrate how energy of the irradiated ions affects the spin wave excitations. The reprogramability of 1D stripe patterned by Ne^+ ions will also be shown.

Chapter 4.2: Complexity effects of antidot lattice structures (from square lattice to wave-like patterns) on magnetization reversal, magnetic anisotropy, and spin wave excitations will be presented. In order to provide better understanding the experimental results will be supported with MuMax calculations.

Chapter 4.3: In this section role of Ga⁺ irradiated ions fluence (F) on spin waves excitations in Pt/Co/Pt thin films will be presented.

Chapter 5 summarizes the work presented in this thesis.

All the concerned literature will be summarized in **chapter 6**.

Chapter 7 will be based on list of published work and work presented in the conferences.

2. Theory

2. Theory

2.1. Introduction to Magnetism

Magnetism is enhanced by the fact that the field still undergoes dynamic developments. Ever new magnetic phenomena continue to be discovered in conjunction with our ability to atomically engineer new materials. As in throughout history, today's magnetism research remains closely tied to applications. It is therefore no surprise that some of the forefront research areas in magnetism today are driven by the “smaller and faster” mantra of advanced technology. The goal to develop, understand, and control the spin in metamaterials is furthermore accompanied by the development of new experimental techniques, that offer capabilities not afforded by conventional techniques.

2.1.1. Origin of Magnetic Moment

The magnetization of a matter is derived by electrons moving around the nucleus of an atom. The magnetism is related to spin angular momentum, orbital angular momentum and spin-orbit interactions angular momentum.

In classical electromagnetism the magnetic moment μ can be explained using the picture of a current loop. Assuming an electron is rotating from left to right on the table plane as shown in (Fig. 2.1). The rotating electron creates a current i on the circle with radius of r . The magnetic moment of a single electron is defined as:

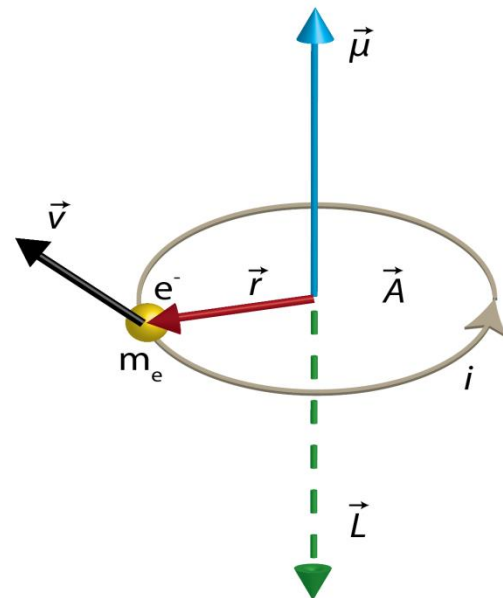


Figure 2.1: Schematic representation of the precession of a single electron on the table plane.

$$\vec{\mu} = i \cdot \vec{A} \quad (2.1)$$

Where, \vec{A} is the circle area. The magnetic moment is written as follows by using the current ($e = i \cdot t$), one cycle ($2\pi = v \cdot t$) and angular momentum ($L = m_e \cdot v \cdot r$) definition.

$$\vec{\mu} = -\frac{e}{2m_e}\vec{L} \quad (2.2)$$

where $\gamma = e/2m_e$ and \vec{L} is the gyromagnetic (magneto-mechanical or magneto-gyric) ratio and the angular magnetic moment respectively. Therefore, the moment $\vec{\mu}$ can be described as:

$$\vec{\mu} = -\gamma\vec{L} \quad (2.3)$$

The time derivative of Eq. (2.3) gives us following equation (γ is constant):

$$\frac{1}{\gamma} \frac{d\vec{\mu}}{dt} = \frac{d\vec{L}}{dt} = \vec{\tau} \quad (2.4)$$

This equation is related to $\vec{\tau} = d\vec{L}/dt$ in two dimensional motion on the plane and $\vec{F} = d\vec{P}/dt$ in one dimensional motion. The equation of motion of magnetic moment in an external field will be express as:

$$\frac{1}{\gamma} \frac{d\vec{\mu}}{dt} = \vec{\mu} \times \vec{H} \quad (2.5)$$

This expression is called the equation of motion for magnetic moment ($\vec{\mu}$). The motion of

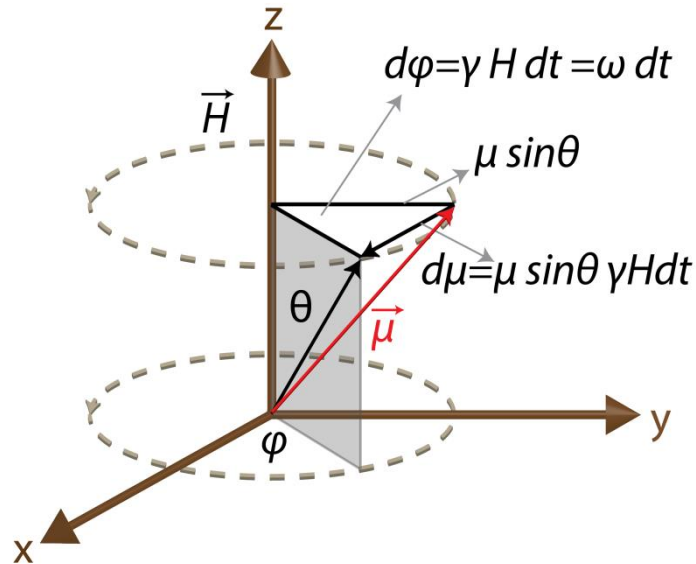


Figure 2.2: Schematic representation of precession of a single magnetic moment in the external magnetic field around the z-axis.

magnetic moment ($\vec{\mu}$) forms a cone related to \vec{H} when the angle θ of magnetic moment and external field does not change. The magnetic moment vector makes precession movement

around external field at a frequency of $\gamma H/2\pi$. This frequency, $\nu = \omega/2\pi = \gamma H/2\pi$, is called the Larmor frequency. In general this frequency used the form ($\omega = \gamma H$) in the literature.

The energy of a magnetic moment is given by:

$$E = -\mu_o\mu \cdot \mathbf{H} = -\mu_o\mu H \cos\theta \quad (2.6)$$

with θ being the angle between the magnetic moment μ and an external magnetic field \mathbf{H} and μ_o the magnetic permeability of free space.

The magnitude of the magnetization \mathbf{M} is defined as the total magnetic moment per volume unit:

$$M = \mu \frac{N}{V} \quad (2.7)$$

Usually, it is given on a length scale which is large enough that an averaging over at least several atomic magnetic moments is carried out. Under this condition the magnetization can be considered as a smoothly varying vector field. In vacuum no magnetization \mathbf{M} occurs.

The microscopic origin of magnetism can be described by quantum mechanical treatment. In solid states, magnetism mainly originates from the magnetic properties of the electrons. Partly, the magnetic moment of the electron is mediated by the angular momentum associated with its motion around the nucleus. The component of this *orbital* angular momentum along a distinct axis (usually one chooses the z-axis) is defined by the quantum number m_l and is given by $m_l\hbar$ where \hbar is Planck's constant divided by 2π . Associated with this angular moment the electron has a magnetic moment along the z-axis of

$$-g_l m_l \mu_B, \quad (2.8)$$

where $\mu_B = e\hbar/(2m_e)$ is the Bohr magneton and g_l being the g -factor for the *orbital* momentum. Moreover, in addition to the *orbital* angular momentum the electron possesses an intrinsic momentum called *spin*. It is accounted for by the spin quantum number $m_s = \pm 1/2$, which defines the component of the spin angular momentum along a fixed direction (again the z-axis) given by $m_s\hbar$. The associated magnetic moment along the z-axis reads

$$g_s m_s \mu_B, \quad (2.9)$$

where $g_s = 2$ is the g -factor of the electron spin.

Since magnetism is a collective phenomenon, the magnetic moments need to communicate with each other. The mechanisms responsible for the different possible interactions are described in the following subsections.

2.2. Magnetic interactions

There are several sources of magnetic interactions by emphasizing ferromagnetic ordering since the ferromagnetism is the subject of this research project.

2.2.1. Magnetic dipolar interaction

Consider two magnetic dipoles μ_1 and μ_2 , each immersed in the magnetic field generated by the other dipole. In this case the corresponding magnetic energy reads [Mat08].

$$E_{dipole} = \frac{\mu_o}{4\pi r^3} [\mu_1 \cdot \mu_2 - \frac{3}{r^2} (\mu_1 \cdot r)(\mu_2 \cdot r)], \quad (2.10)$$

where μ_o is the permeability. Since r is the vector connecting the two dipoles, the energy decreases with the 3rd order of their distance. For an estimation of this energy we choose typical values with $\mu_1 = \mu_2 = 1 \mu_B$ and $r = 2\text{\AA}$. Additionally, we assume $\mu_1 \uparrow \uparrow \mu_2$ and $\mu \uparrow \uparrow r$. This situation results in an energy of:

$$E = \frac{\mu_o \mu_B^2}{2\pi r^3} = 2.1 \times 10^{-24} J \quad (2.11)$$

The corresponding temperature ($E = kT$) is far below 1K. But, the order temperature typically reaches values of several 100K for a lot of ferromagnetic materials. Therefore, the magnetic dipole interaction is too small to cause ferromagnetism. However, this interaction is accountable for effects such as demagnetizing field and spin waves in the long wave length regime.

2.2.2. Exchange interaction

Magnetism can be divided into two groups, A and group B. In group A there is no interaction between individual moments and each moment acts independently of the others.

Group B consists of the magnetic materials most people are familiar with, like iron, nickel. Magnetism occurs on these materials because the magnetic moments couple to one

another and form magnetically ordered states. The coupling, which is quantum mechanical in nature is known as exchange interaction and is rooted in the overlap of electrons in conjunction with Pauli's exclusion principle. Exchange interactions lie at the heart of the phenomenon of long range magnetic order. Exchange interactions are nothing more than electrostatic interactions, arising because charges of the same sign cost energy when they are close together and save energy when they are apart. Whether it is a ferromagnet, Antiferromagnet or ferrimagnet the exchange interaction between the neighboring magnetic ions will force the individual moments into parallel (ferromagnetic) or antiparallel (antiferromagnetic) alignment with their neighbors. There are following types of exchange which are currently believed to exist are:

2.2.2.1. Direct Exchange

If the electrons on neighboring magnetic atoms interact via an exchange interaction, this is known as direct exchange. This is because the *exchange interaction* proceeds directly without the need for an intermediary. Though this seems the most obvious route for the exchange interaction to take, the reality in physical situations is rarely that simple.

Very often direct exchange cannot be an important mechanism in controlling the magnetic properties because there is insufficient direct overlap between neighboring magnetic orbitals. For example, in rare earths the 4f electrons are strongly localized and lie very close to the nucleus, with little probability density extending significantly further than about a tenth of the interatomic spacing. This means that the direct exchange interaction is unlikely to be very effective in rare earths. Even in transition metals, such as Fe, Co and Ni, where the 3d orbitals extend further from the nucleus, it is extremely difficult to justify why direct exchange should lead to the observed magnetic properties. These materials are metals which means that the role of the conduction electrons should not be neglected, and a correct description needs to



Figure 2.3: (a) Antiparallel alignment for small interatomic distances, (b) Parallel alignment for large interatomic distances.

take account of both the localized and band character of the electrons. Thus in many magnetic materials it is necessary to consider some kind of *indirect exchange interaction*.

The exchange energy forms an important part of the total energy of many molecules and of the covalent bond in many solids. Heisenberg showed that it also plays a decisive role in ferromagnetism. This indeed is an alternative way of formulating Pauli's exclusion principle, since it implies the probability to find two electrons with parallel spins in the same state to vanish. Therefore, the Coulomb energy of electrons with parallel spins is lowered on account of their spatial separation. The corresponding exchange energy of two electrons with spin operators \hat{S}_1 and \hat{S}_2 can be expressed as

$$E_{ex} = -2J_{12}S_1 \cdot S_2 = -2JS_1S_2\cos\varphi \quad (2.12)$$

where J_{12} is a particular integral, called the *exchange integral*, and φ is the angle between the spins. For $J_{12} > 0$ the interaction causes parallel alignment of the spins, which corresponds to ferromagnetic order. In a continuum approximation of the crystal lattice, the exchange energy of a cubic crystal is given by:

$$E_{ex} = A \int dV (\nabla m)^2 \quad (2.13)$$

With the exchange constant $A = 2JS^2 p/a$ and the normalized magnetization $\mathbf{m} = \mathbf{M}/M_S$ and

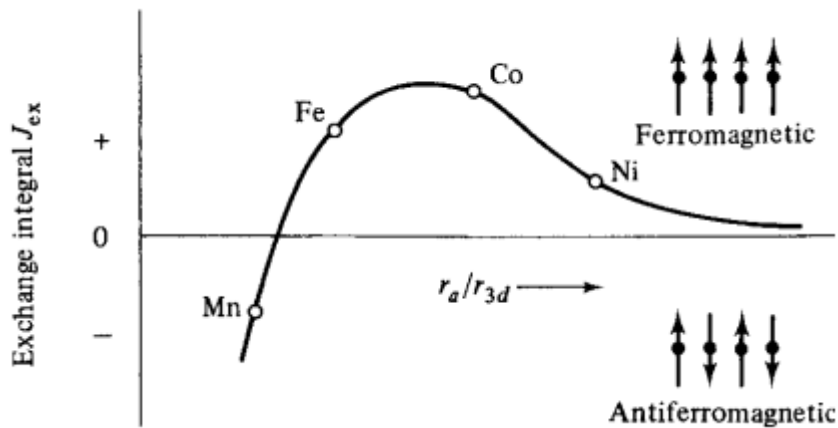


Figure 2.4: Bethe-Slater curve (schematic). Image is adopted from Ref. [Cul09].

M_S being the magnetization vector and the saturation magnetization respectively. The exchange integral is J , the distance between the nearest neighbors is a , and the number of sites in the unit cell is denoted by p . Since the exchange constant depends on the overlap of the

single electron wave functions, which is taken into account by a , J generally vanishes except for neighboring electrons.

The Bethe-Slater curve represents the magnitude of direct exchange as a function of interatomic distances. The curve of Fig. 2.4 [Cul09] can be applied to a series of different elements if we compute r_d/r_{3d} from their known atom diameters and shell radii. The points so found lie on the curve as shown, and the curve correctly separates Fe, Co, and Ni from Mn and the next lighter elements in the first transition series. (Mn is antiferromagnetic below 95K, and Cr, the next lighter element, is antiferromagnetic below 37°C; above these temperatures they are both paramagnetic.) Although the theory behind the Bethe–Slater curve has received much criticism, the curve does suggest an explanation of some otherwise puzzling facts. Thus ferromagnetic alloys can be made of elements which are not in themselves ferromagnetic; examples of these are MnBi and the Heusler alloys, which have approximate compositions Cu_2MnSn and Cu_2MnAl . Because the manganese atoms are farther apart in these alloys than in pure manganese, r_d/r_{3d} becomes large enough to make the exchange interaction positive.

Consequently, the exchange interaction is only very short ranged. However, due its magnitude which is of the order of 10^{-2} eV, it can exclusively account for magnetic long range ordering and causes a mutual alignment of the permanent magnetic moments below a critical temperature.

2.2.2.2. Indirect exchange in Metals

Indirect exchange couples moments over relatively large distances. It is the dominated exchange interaction in metals, where there is little or no direct overlap between neighboring electrons. It therefore acts through an intermediary, which in metals are conduction electrons (itinerant electrons). This type of exchange is better known as *RKKY* (the initial letters of the surnames of the discoverers of the effect, Ruderman, Kittel, Kasuya and Yosida) interaction. A magnetic ion induces a spin polarization in the conduction electrons in its neighborhood. This spin polarization in the itinerant electron is felt by the moments of other magnetic ions within the range leading to an indirect exchange coupling.

The coupling takes the form of an r -dependent exchange interaction $J_{RKKY}(r)$ given by

$$J_{RKKY}(r) \propto \frac{\cos(2k_F r)}{r^3} \quad (2.14)$$

at large r (assuming a spherical Fermi surface of radius k_F). The interaction is long range and has an oscillatory dependence on the distance between the magnetic moments shown in Fig.

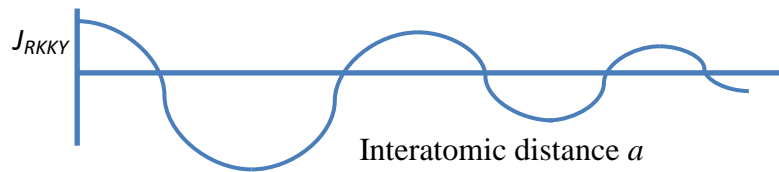


Figure 2.5: The coefficient of indirect (RKKY) exchange versus the interatomic spacing a .

(2.5). Hence depending on the separation it may be either ferromagnetic or antiferromagnetic. The coupling is oscillatory with wavelength π/k_F because of the sharpness of the Fermi surface.

2.2.2.3. Indirect exchange in ionic solids: superexchange

A number of ionic solids, including some oxides and fluorides, have magnetic ground states. For example, MnO and MnF₂ are both antiferromagnets, though this observation appears at first sight rather surprising because there is no direct overlap between the electrons

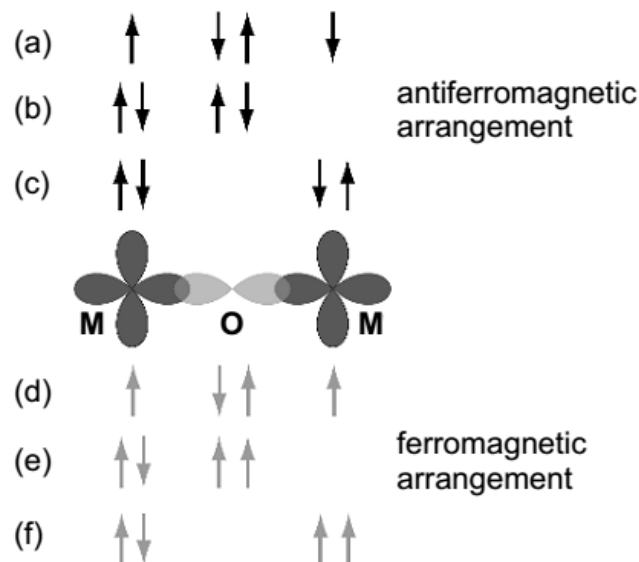


Fig. 2.6: Occurrence of a super exchange interaction in a magnetic oxide. The arrows represent the spins of the electrons being involved into the interaction between the metal (M) and oxygen (O) atom. Image is adopted from Ref. [Blu01].

on Mn²⁺ ions in each system. The exchange interaction is normally very short-ranged so that the longer- ranged interaction that is operating in this case must be in some sense 'super'.

For example in the case of antiferromagnetic ionic solid MnO, each Mn^{2+} ion exhibits 5 electrons in its d shell with all spins being parallel due to Hund's rule. The O^{2-} ions possess electrons in p orbitals which are fully occupied with their spins aligned antiparallel. There are two possibilities for the relative alignment of the spins in neighboring Mn atoms. A parallel alignment leads to a ferromagnetic arrangement whereas an antiparallel alignment causes an antiferromagnetic arrangement. That configuration is energetically favored which allows a delocalization of the involved electrons due to a lowering of the kinetic energy (see Fig. 2.6) [Blu01]. In the antiferromagnetic case the electrons with their ground state given in (a) can be exchanged via excited states shown in (b) and (c) leading to a delocalization. For ferromagnetic alignment with the corresponding ground state presented in (d) the Pauli Exclusion Principle forbids the arrangements shown in (e) and (f). Thus, no delocalization occurs. Therefore, the antiferromagnetic coupling between two Mn atoms is energetically favored. It is important that the electrons of the oxygen atom are located within the same orbital, i.e. the atom must connect the two Mn atoms.

2.2.2.4. Double exchange

In some oxides, it is possible to have a ferromagnetic exchange interaction which

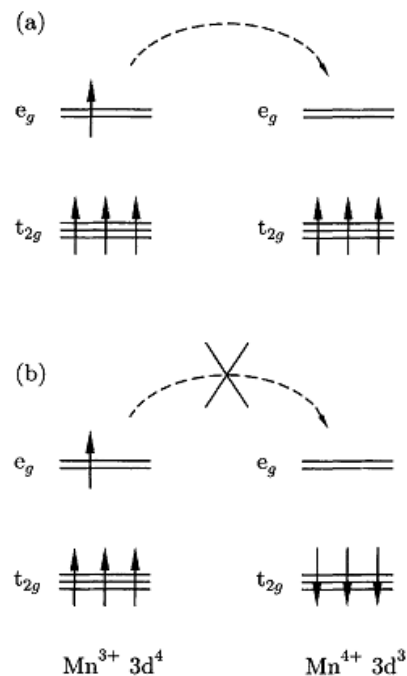


Fig. 2.7: Double exchange mechanism gives ferromagnetic coupling between Mn^{3+} and Mn^{4+} ions participating in electron transfer. The single-centre exchange interaction favors hopping if (a) neighboring ions are ferromagnetically aligned and not if (b) neighboring ions are antiferromagnetically aligned. Image is adopted from Ref. [Blu01].

occurs because the magnetic ion can show mixed valency, that is it can exist in more than one oxidation state. Examples of this include compounds containing the Mn ion which can exist in oxidation state 3 or 4, i.e. as Mn^{3+} or Mn^{4+} .

The ferromagnetic alignment is due to the double exchange mechanism which can be understood with reference to Fig. 2.7 [Blu01]. The e_g electron on a Mn^{3+} ion can hop to a neighboring site only if there is a vacancy there of the same spin (since hopping proceeds without spin-flip of the hopping electron). If the neighbor is a Mn^{4+} which has no electrons in its e_g shell, this should present no problem. However, there is a strong single-centre (Hund's rule number 1) exchange interaction between the e_g electron and the three electrons in the t_{2g} level which wants to keep them all aligned. Thus it is not energetically favorable for an e_g electron to hop to a neighboring ion in which the t_{2g} spins will be antiparallel to the e_g electron (Fig. 2.7(b)). Ferromagnetic alignment of neighboring ions is therefore required to maintain the high-spin arrangement on both the donating and receiving ion. Because the ability to hop gives a kinetic energy saving, allowing the hopping process shown in Fig. 2.7(a) reduces the overall energy. Thus the system ferromagnetically aligns to save energy. Moreover, the ferromagnetic alignment then allows the e_g electrons to hop through the crystal and the material becomes metallic.

2.2.2.5. Anisotropic exchange interaction

It is also possible for the spin-orbit interaction to play a role in a similar manner to that of the oxygen atom in superexchange. Here the excited state is not connected with oxygen but is produced by the spin-orbit interaction in one of the magnetic ions. There is then an exchange interaction between the excited state of one ion and the ground state of the other ion. This is known as the **anisotropic exchange interaction**, or also as the **Dzyaloshinsky-Moriya interaction** (DMI). When acting between two spins S_1 and S_2 it leads to a term in the Hamiltonian, \hat{H}_{DM} equal to: [Blu01]

$$\hat{H}_{DM} = \mathbf{D} \cdot \mathbf{S}_1 \times \mathbf{S}_2 \quad (2.15)$$

The vector \mathbf{D} vanishes when the crystal field has an inversion symmetry with respect to the centre between the two magnetic ions. However, in general \mathbf{D} may not vanish and then will lie parallel or perpendicular to the line connecting the two spins, depending on the symmetry. The form of the interaction is such that it tries to force \mathbf{S}_1 and \mathbf{S}_2 to be at right angles in a plane perpendicular to the vector \mathbf{D} in such an orientation as to ensure that the energy is

negative. Its effect is therefore very often to cant (i.e. slightly rotate) the spins by a small angle. It commonly occurs in antiferromagnets and then results in a small ferromagnetic component of the moments which is produced perpendicular to the spin-axis of the antiferromagnet. The effect is known as weak ferromagnetism. It is found in, for example, $\alpha\text{-Fe}_2\text{O}_3$, MnCO_3 and CoCO_3 .

2.3. The Energy Functional of a Magnet

The total internal magnetic field H_{eff} acting on the magnetic moments inside a solid results from the functional derivative of the total energy density $E_{tot} = E_{tot} / V$ with respect to the reduced magnetization $m(r) = M(r) / M_S$.

$$H_{eff} = -\frac{1}{\mu_0} \frac{\delta E_{tot}}{\delta m}, \quad (2.16)$$

where V is the sample volume. The free energy density of a magnetic system is given by

$$E_{tot} = E_{zee} + E_{ani} + E_{dem} + E_{ex} \quad (2.17)$$

where E_{zee} represents the Zeeman energy, E_{ani} the anisotropy, E_{dem} the demagnetizing, and E_{ex} the exchange energy density.

2.3.1. Zeeman Energy

The Zeeman term arises from the interaction of the magnetization M with an external field H_o and represented by the following equation

$$E_{zee} = \frac{1}{V} \int dV M \cdot H_o \quad (2.18)$$

It favors parallel alignment of the magnetization along the external field direction.

2.3.1.1. Magnetocrystalline anisotropy

The most important type of anisotropy is the magneto crystalline anisotropy which is caused by the spin orbit interaction of the electrons. The electron orbitals are linked to the crystallographic structure. Due to their interaction with the spins they make the latter prefer to align along well defined crystallographic axes. Therefore, there are directions in space which a magnetic material is easier to magnetize in than in other ones (easy axes or easy magnetization axes). The spin-orbit interaction can be evaluated from basic principles. However, it is easier to use phenomenological expressions (power series expansions that take into account the crystal symmetry) and take the coefficients from experiment.

In cubic systems the energy density due to crystal anisotropy reads

$$E_{ani} = K_0 + K_1(\alpha_x^2\alpha_y^2 + \alpha_y^2\alpha_z^2 + \alpha_z^2\alpha_x^2) + K_2\alpha_x^2\alpha_y^2\alpha_z^2, \quad (2.19)$$

where α_i are the directional cosines of the normalized magnetization \mathbf{m} with respect to the Cartesian axes of the lattice. K_i are the magnetocrystalline anisotropy constants, K_0 , K_1 , and K_2 are the crystalline anisotropy constants of zero, first and second order, respectively. In addition to the intrinsic ordering arising from the crystal lattice, atomic ordering may also be caused by surfaces and interface and hence is of particular importance in confined magnetic system. For crystals exhibiting uniaxial anisotropy, the energy density is

$$E_{ani} = K_U\alpha_x^2, \quad (2.20)$$

with the uniaxial anisotropy constant K_U .

2.3.2. Anisotropy Energy

Magnetic anisotropy is the directional dependence of material's magnetic properties. In the absence of external magnetic field, a magnetically isotropic material has no preferential directions for its magnetic moment while a magnetically anisotropic material will align its magnetic moments with one of the easy axis (the energetically favorable axis in which spontaneous magnetization aligns determined by the source of magnetic anisotropy). There could be several sources of magnetic anisotropy. Beside the stress anisotropy (also called magnetostriction), and induced magnetic anisotropy other sources such as magnetocrystalline anisotropy, shape anisotropy (demagnetizing or stray field), and surface and interface anisotropy are discussed in the following section being related to area of present study.

2.3.2.1. Demagnetizing Energy

Polycrystalline samples without a preferred orientation of the grains do not possess any magneto crystalline anisotropy. But, an overall isotropic behavior concerning the energy being needed to magnetize it along an arbitrary direction is only given for a spherical shape. If the sample is not spherical then one or more specific directions occur which represent easy magnetization axes which are solely caused by the shape. This phenomenon is known as shape anisotropy. In order to get a deeper insight we have to deal with the stray and demagnetizing field of a sample.

The relationship $B = \mu_o(H + M)$ only holds inside an infinite system. A finite system exhibits poles at its surfaces which leads to a stray field outside the sample. This occurrence of a stray field results in demagnetizing field inside the sample.

The energy of a sample in its own stray field is given by the stray field energy E_{dem}

$$E_{dem} = -\frac{1}{2} \int \mu_o M \cdot H_{dem} dV \quad (2.21)$$

The expression for the demagnetizing field of an arbitrary shaped element generally constitutes a very complex function of position. It is however, uniform in the case of an homogenously magnetized ellipsoid (possesses a constant demagnetizing field H_{dem}) which is given by:

$$H_{dem} = -NM \quad (2.22)$$

with N being the demagnetizing tensor. Thus, the stray field energy (demagnetizing energy) amounts to:

$$E_{dem} = \frac{1}{2} \cdot \mu_o \int MNM dV \quad (2.23)$$

$$E_{dem} = \frac{1}{2} V \mu_o MNM \quad (2.24)$$

with V being the volume of the sample. N is a diagonal tensor if the semi axis a, b, and c of the ellipsoid represents the axes of the coordination system. Then, the trace is given by

$$\text{tr}N = 1 \quad (2.25)$$

An arbitrary direction of the magnetization with respect to the semi axes can be characterized by the direction cosine α_a , α_b , and α_c . The tensor is given by:

$$N = \begin{pmatrix} N_a & 0 & 0 \\ 0 & N_b & 0 \\ 0 & 0 & N_c \end{pmatrix} \quad (2.26)$$

and the demagnetizing energy per volume amounts to”

$$E_{dem} = \frac{1}{2} \cdot \mu_o \cdot M^2 (N_a \alpha_a^2 + N_b \alpha_b^2 + N_c \alpha_c^2) \quad (2.27)$$

for sphere the tensor N amounts to:

$$N = \begin{pmatrix} 1/3 & 0 & 0 \\ 0 & 1/3 & 0 \\ 0 & 0 & 1/3 \end{pmatrix} \quad (2.28)$$

and the demagnetizing field energy density to:

$$E_{dem} = 1/2 \cdot \mu_o M^2 \cdot 1/3 (\alpha_a^2 + \alpha_b^2 + \alpha_c^2) \quad (2.29)$$

$$E_{dem} = 1/6 \cdot \mu_o M^2 \quad (2.30)$$

For an infinitely extended and very thin plate, we have $a = b = \infty$, and

$$N = \begin{pmatrix} 1/2 & 0 & 0 \\ 0 & 1/2 & 0 \\ 0 & 0 & 1/2 \end{pmatrix} \quad (2.31)$$

Now, the demagnetizing field energy density amounts to:

$$E_{dem} = 1/2 \cdot \mu_o M^2 \cos^2 \theta \quad (2.32)$$

This results is important for thin magnetic films and multilayers. Equation (2.32) can be rewritten as:

$$E_{dem} = K_o + K_{shape}^V \sin^2 \theta \quad (2.33)$$

with $K_{shape}^V \propto -M^2 < 0$. The demagnetizing field energy reaches its minimum value at $\theta = 90^\circ$. This means that shape anisotropy favors a magnetization direction parallel to the surface, i.e. within the film plane.

2.3.2.2. Surface and interface anisotropy

Due to the broken symmetry at interfaces the anisotropy energy contains terms with lower order in α which are forbidden for three-dimensional systems. Therefore, each effective anisotropy constant K^{eff} is divided into two parts, first term on right hand side describing the volume and second term the surface contribution

$$K^{eff} = K^V + 2K^S/d \quad (2.34)$$

with K^V being the volume dependent magneto crystalline anisotropy constant and K^S the surface dependent magneto crystalline anisotropy constant. The factor of two is due to the creation of two surfaces. The second term exhibits an inverse dependence on the thickness d of the system. Thus, it is only important for thin films.

In order to illustrate the influence of the surface anisotropy we will discuss the so-called “spin reorientation transition” (SRT). Rewriting (2.34) results in:

$$d \cdot K^{eff} = d \cdot K^V + 2K^S \quad (2.35)$$

Plotting this dependence as a $d \cdot K^{eff}$ diagram allows to determine K^V as the slope of the resulting line and $2K^S$ as the zero-crossing which is exemplarily shown for a thin Co layer with variable thickness d on a Pd substrate (Fig. 2.8). Due to the shape anisotropy K^V is negative. This can directly be seen by the negative slope which results in an in-plane magnetization. The zero-crossing occurs at a positive value K^S . This leads to a critical thickness d_c :

$$d_c = -\frac{2K^S}{K^V} \quad (2.36)$$

with $d < d_c$: perpendicular magnetization and for $d > d_c$: in-plane magnetization due to the change of sign of K^{eff} .

Thus, the volume contribution always dominates for thick films with a magnetization

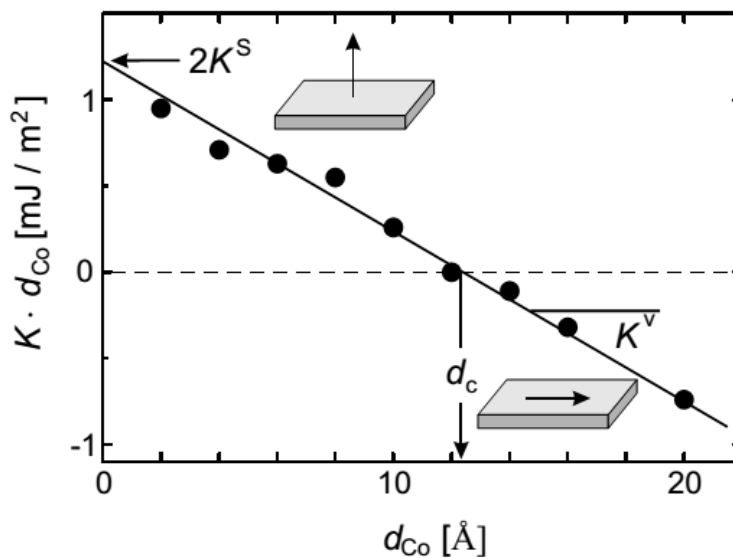


Fig. 2.8: Magnetic anisotropy of a Co thin film layer in a Co/Pd multilayer as a function of the Co thickness d_{Co} . The slope allows to determine K^V . The zero crossing amounts to $2K^S$ [Image adopted from [Bro02]].

being within the film plane. The relative amount of the surface contribution increases with decreasing thickness followed by a spin reorientation transition towards the surface normal below d_c .

2.3.3. Exchange Energy

The exchange term has already been discussed above in section 2.2.2, equation (2.13). The corresponding energy density reads:

$$\varepsilon_{ex} = A \int dV (\nabla m)^2 \quad (2.37)$$

2.4. Magnetic Domains

Since the beginning of the last century, it is a well known fact that the magnetization is not uniform in a ferromagnetic material, but possesses a number of small regions (“magnetic” domains) with different orientation of magnetization. This domain configuration minimizes the stray field energy. Within each domain, the magnetic moments are aligned parallel to each other and point into one direction of the preferential directions that are determined by the magnetic field anisotropies in the absence of an applied external magnetic field. Domains are separated by domain walls.

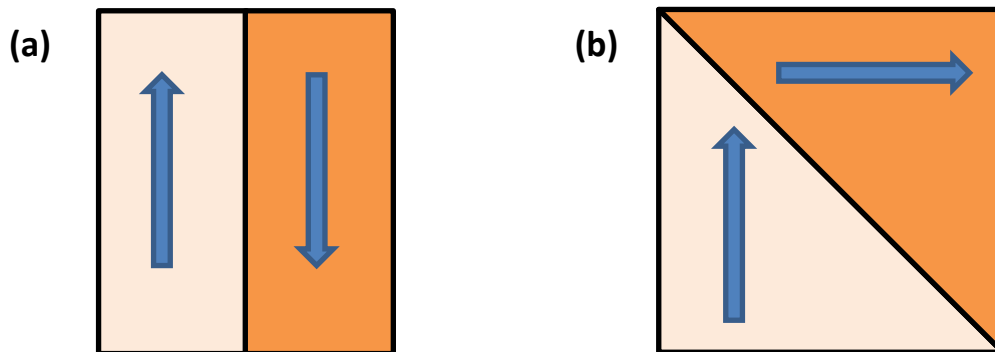


Figure 2.9: (a) 180° and 90° domain wall

These considerations allow to describe a lot of properties of different magnetic systems. Two examples are:

1. In soft magnetic materials smallest external fields ($\approx 10^{-6}$ T) are sufficient to reach saturation magnetization ($\mu_0 M \approx 1$ T) by application of a very weak magnetic field (as low as 10^{-6} T). Such low applied fields would have negligible effect on a paramagnet. The large effect in the ferromagnetic specimen is because the external field does not need to order all magnetic moments macroscopically (because in each domain they are

already ordered) but has to align the domains. Thus, a movement of domain walls only occurs which requires low energy.

2. It is possible that ferromagnetic materials exhibit a vanishing total magnetization $M=0$ below the critical temperature without applying an external field. In this situation each domain still possesses a saturated magnetization but due to the different orientations the total magnetization amounts to zero.

2.4.1. Domain walls

The change of the magnetization direction between the adjacent domains does not occur

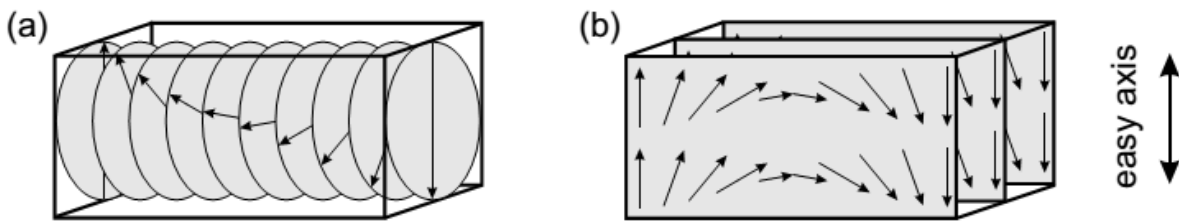


Figure 2.10: Rotation of the magnetization in a (a) Bloch wall and (b) Néel wall

abruptly but is characterized by a slight tilt of the microscopic magnetic moments in the boundary regions. These boundary regions are several tens of nanometers wide and called domain walls. The domain walls can be classified by the angle of the magnetization between neighbored domains with the wall as boundary. A large variety of domain patterns exists depending on the specific properties of the ferromagnetic sample under investigation [Hub09]. A 180° domain wall represents the boundary between two domains with opposite magnetization (see Fig. 2.9a) and 90° wall domain wall represents the boundary between two domains with magnetization being perpendicular to each other (see Fig. 2.9b). A 180° domain wall is a Bloch wall (Fig. 2.10a) in which the magnetization rotates in a plane parallel to the plane of the wall. Another possible configuration is the Néel wall (Fig. 2.10b) where rotation of the magnetization takes place in a plane which is perpendicular to the plane of the domain wall [Bat08]. Bloch walls are more common in bulk-like thick films, while Néel walls are often observed in thin films (Fig. 2.11), where a surface stray field is avoided by the rotation of the moments within the surface plane. The width of a domain wall is determined by the exchange and the anisotropy energy [Hub09].

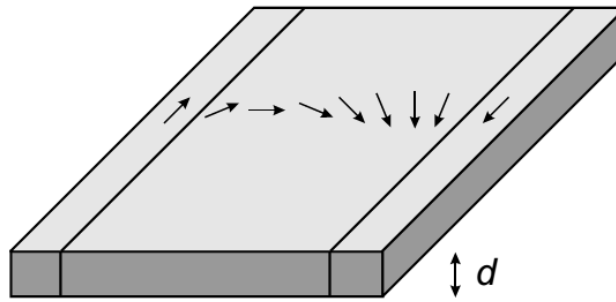


Figure 2.11: The Néel wall is energetically favorable in thin film systems exhibiting only a small thickness d with an in-plane magnetization due to the avoidance of stray fields

2.5. Magnetization processes

Magnetization processes are sensitive to the structures of magnetic materials. The existence of domains is hinted at by the observation that some magnetic properties, and in particular, coercivity and remanence. However, it must be noted that the coercivity is not an intrinsic magnetic property, which means that the value of the coercivity depends not only on the chemical composition, the temperature, and the magnetic anisotropy, but also strongly on the microstructure of the material [Wec87, Sch87, Mis87, Sch88, Mis88, Sag87, Ram88 and Fid96]. The necessary interplay between the microstructure and the intrinsic magnetic properties for the existence of coercivity in a given material is in general an intricate process. The understanding of the mechanisms of coercivity is essential for further improving hard magnetic properties. There are various methods of increasing or decreasing the coercivity of magnetic materials, which involve controlling the magnetic domains within the material. Depending on the H_c different regions can be classified:

1. Multidomain (MD). Magnetization changes by domain wall motion.
2. Single domain (SD). At critical thickness the system behaves as single domain and at this point coercivity reaches a maximum value. But this critical thickness coercivity decreases again but this time due to the randomizing effects of thermal energy.

2.5.1. Magnetic parameters

In an ideal crystal which does not contain any defects the magnetization of a demagnetized ferromagnet starts with reversible domain wall movements. This process ends when all domain walls are annihilated or all walls are oriented perpendicularly to the external magnetic field. If this is the only process until saturation is reached we obtain a magnetization as a function of the external magnetic field which is shown in Fig. 2.12.

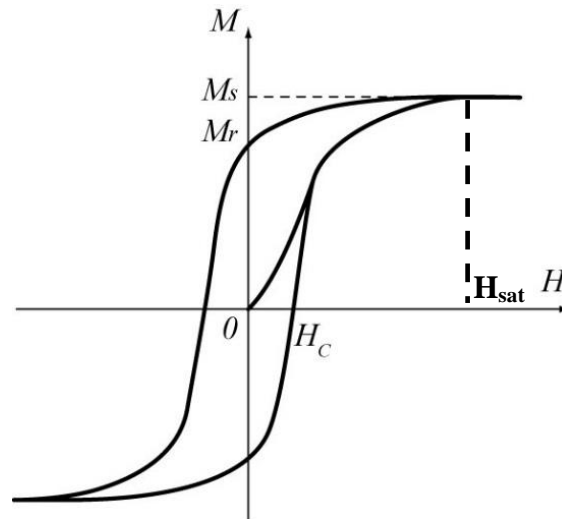


Figure 2.12: A typical magnetic hysteresis loop for a ferromagnetic material. Saturation magnetization (M_s), remanence (M_r), coercivity (H_c), and saturation field H_{sat} are illustrated on the curve.

One can see that initially magnetization curve increases with the increase in the applied external field to demagnetized sample. In the first quadrant the magnetization and the applied field are both positive, i.e they are in the same direction. The magnetization increases initially by the growth of favorably oriented domains, which will be magnetized in the easy direction of the crystal. When the magnetization can increase no further by the growth of domains, the direction of magnetization of the domains then rotates away from the easy axis to align with the field. When all of the domains have fully aligned with the applied field saturation is reached and the magnetization cannot increase further. If the field is removed the magnetization returns to the y-axis (i.e., $H = 0$), and the domains will return to their easy direction of magnetization, resulting in a decrease in the overall magnetization. If the direction of applied field is reversed (i.e., to the negative direction) then the magnetization will follow the solid line into the second quadrant. The magnetization will only decrease after a sufficiently high field is applied to: (1) nucleate and grow domains favorably oriented with respect to the applied field or (2) rotate the direction of magnetization of the domains towards the applied field. After applying a high enough field the magnetization reaches its saturation value in the negative direction. If the applied field is then decreased and again applied in the positive direction then the full hysteresis loop is plotted. If the field is repeatedly switched from positive to negative directions and is of sufficient magnitude then the magnetization will cycle around the hysteresis loop in an anti-clockwise direction. The area contained within the

loop indicates the amount of energy absorbed by the material during each cycle of the hysteresis loop.

The hysteresis loop is a means of characterizing magnetic materials, and various parameters can be determined from it. From the first quadrant (Fig. 2.12) the saturation magnetization, M_S can be measured. Most of the useful information, however, can be derived from the second quadrant of the loop, and, indeed, it is sometimes conventional only to show this quadrant. The magnetization retained by the magnet after the magnetizing field has been removed is called the remanence. The magnetization at zero field is called the coercivity (H_c).

Figure 1.14: Magnetization reversal curve for nucleation dominated (filled black squares) and domain wall motion dominated (filled red circles).

2.5.2. Magnetization reversal process

Magnetization reversal may be realized by changing applied field or by thermal activation. At constant field, thermal activation alone may lead to significant variation of magnetization in some cases. Time dependence of magnetization under constant field is referred as magnetic viscosity or magnetic aftereffect. The magnetic viscosity due to thermal activation is general properties of all ferromagnetic materials. Two magnetization reversal processes can be distinguished based on coercivity measurements. The first one is controlled by nucleation of reversed domains. The magnetization reversal is realized by spontaneous

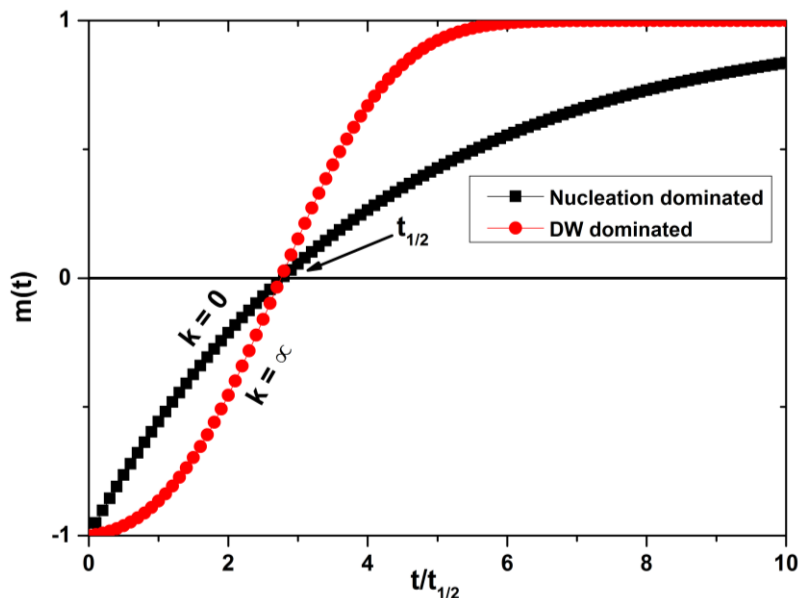


Figure 2.13: Time dependence magnetization relaxation curves: nucleation dominated (Black), and domain wall propagation (Red) reproduced from Fatuzzo and Lubrune model [Fat62, Lab89].

expansion of these nucleated domain walls. Compared to nucleation, the propagation of the

reversed domains occurs much easier. The other coercivity mechanism is controlled by the domain-wall propagation process. The domain wall is pinned by crystallographic defects or nonmagnetic precipitates (pinning centers). The magnetization reversal can only be realized by overcoming the maximum pinning force. The magnetization reversal processes can be described through the model (MR curves) proposed by Fatuzzo and Labrune [Fat62, Lab89] see (Fig. 2.13) in which two curves describe the two MR mechanisms. MR is processed through the curve (filled black squares) for nucleation dominated and the curve (filled red circles) domain wall motion dominated. More details are described in the appendix.

2.6. Magnetization Dynamics

When a magnetic material is exposed to an external magnetic field, its magnetic

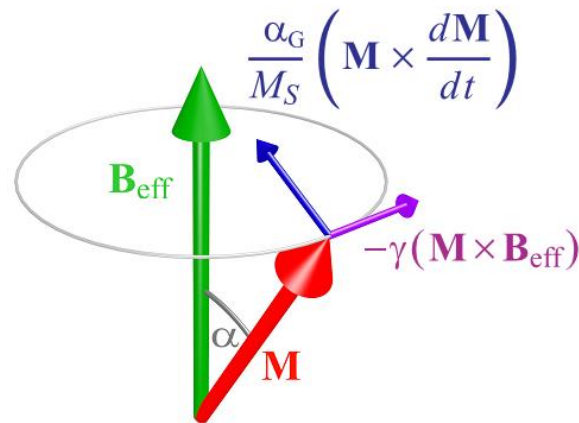


Figure 2.14: The precessional motion of the magnetization around the effective magnetic field direction, governed by the Landau-Lifshitz-Gilbert equation (2.43). The torque $-\gamma M \times B_{eff}$ provides the rotational motion around B_{eff} while the Gilbert damping term forces the magnetization to be aligned along the effective field B_{eff} .

Figure adopted from Ref [Obr13]

moments tend to align themselves along the external field to minimize their energy. The kinetic motion of the magnetic moments disturbs this alignment. Therefore, the moments do not align themselves directly to the magnetic field; instead, they execute a precessional motion around the direction of the external field. The precession of magnetic moments is referred to as magnetization dynamics. The crucial difference of magnetization dynamics compared to static phenomena (usually in the millisecond time range) is the time scale on which the magnetic system is disturbed by an external stimulus and of course on which time scale one in turn observes its response. When applying quasi static fields to a magnetic system, the magnetization appears to be always in equilibrium since the dynamic processes happen on the nanosecond timescale or faster. In contrast, when applying alternating magnetic

fields with a frequency equal to the resonance frequency of the system, the magnetization configuration is resonantly disturbed from its equilibrium position. This behavior of magnetization under the influence of an external magnetic field is described phenomenologically by the Landau-Lifshitz and Gilbert equation of motion [Gil04].

The Landau-Lifshitz-Gilbert (LLG) equation is a torque equation which was first introduced by Lev Landau and Evgeny Lifshitz in 1935 as Landau-Lifshitz equation [Lan35]. The Landau-Lifshitz (LL) equation was a damping-free equation. Later, Gilbert modified it by inserting a magnetic damping term [Gil04]. In this section, first the LL equation will be derived by a semiclassical approach. Later, this equation will be modified by introducing the Gilbert damping term.

When a magnetic moment μ_m is placed in an effective magnetic field B_{eff} , it experiences a torque:

$$\tau = \mu_m \times B_{eff} \quad (2.38)$$

In a semiclassical approach, the magnetic moment μ_m of an atom can be written in terms of its angular momentum J as

$$\mu_m = -\frac{g\mu_B}{\hbar}J = -\gamma J \quad (2.39)$$

where $\gamma = g\mu_B/\hbar$ is the gyromagnetic ratio. As $\tau = dJ/dt$, Eq. (2.38) can be re-written as

$$\frac{dJ}{dt} = -\frac{1}{\gamma} \frac{d\mu_m}{dt} = \mu_m \times B_{eff} \quad (2.40)$$

In the continuum limit, the atom magnetic moment can be replaced by the macroscopic magnetization M resulting in the equation of motion, i.e, Landau-Lifshitz (LL) equation:

$$\frac{dM}{dt} = -\mu_o\gamma M \times B_{eff} \quad (2.41)$$

Here, the effective magnetic field B_{eff} is a sum of all external and internal magnetic fields:

$$B_{eff} = B_0 + B_M(t) + B_{ex} + B_{dem} + B_{ani} + \dots \quad (2.42)$$

Here, B_0 is the static component of the applied magnetic field while $B_M(t)$ is the dynamic component. B_{ex} is a magnetic field originating from the exchange interaction. B_{dem} represents the demagnetization field created by the dipolar interaction of magnetic surface and volume charges. The field B_{ani} includes all kinds of anisotropic fields like shape anisotropy, crystalline anisotropy, etc.

The physical meaning of Eq. (2.41) explores two important features of the equation of motion. A dot-product of Eq. (2.41) with M results that the magnitude of M is conserved. Secondly, a dot product with B_{eff} concludes that the orientation of M with respect to B_{eff} will not vary over time. Further, the system is non-dissipative which means that the magnetization will continue to precess for infinitely long time. Definitely, in the real world no such system exists. To rectify this issue, Gilbert [Lan35] phenomenologically introduced a proper damping term to the LL equation leading to a Landau-Lifshitz-Gilbert equation as:

$$\frac{dM}{dt} = -\mu_o\gamma M \times B_{eff} + \frac{\alpha_G}{M_S} \left(M_S \times \frac{dM_S}{dt} \right), \quad (2.43)$$

here, α_G describe the dimensionless Gilbert damping parameter. An important feature of the Gilbert damping parameter is its viscous nature, i.e, an increase in rotation of magnetization dM_S/dt increases the damping of the system.

A schematic of the interplay between different torques on the magnetization is depicted in Fig. 2.14. The damping torque always acts perpendicular to the magnetization as well as the precessional term and tries to align the magnetization along the effective magnetic field. Therefore, the damping torque provides a dissipative mechanism which eventually, transfers the energy and the angular momentum of the spin system (magnon system) to the phonon system via spin-orbit (spin-lattice) interaction [Suh98]. Other than spin-orbital interaction, in metallic systems, magnon-electron scattering [Kam75, Kit53, Kam70] and eddy currents [Hri02] provide extra channels for magnetization relaxation. Additionally, damping channels like spin pumping [Kap13, Sun05,], multi-magnon scattering [Gur96, Jun13, Sch12], and Cherenkov scattering processes also exist in magnetic materials.

2.7. Spin waves

Within the macro-spin approximation, the Landau-Lifshitz-Gilbert equation describes the magnetization dynamics in homogeneously magnetized structures. A ferromagnet is perfectly ordered at $T = 0K$. An increase in the temperature causes thermal fluctuations and reduces the

magnetization. The magnetization vanishes at the critical temperature T_c . In order to explain the temperature dependence of the magnetization in ferromagnetic materials, Bloch introduced the concept of collective excitations of magnetic moments in magnetically ordered materials [Blo30]. At low temperatures these low-energetic magnetic excitations are known as spin waves. These spin waves are quantized by magnons. An analog are lattice vibrations in crystals which are quantized by phonons. Since the wavelength of a spin wave is determined by the phase shift of the precessing magnetic moments, the mutual interactions between the moments, discussed in Section 2.2.1, play a crucial role for spin waves. On the basis of these interactions—exchange interaction and dipolar interaction—spin waves are classified into two branches: dipolar-dominated spin waves, and exchange-dominated spin waves. For long-wavelength spin waves, the difference between neighboring moments is rather small; therefore, the impact of exchange interaction is negligible for these spin waves. The energy of long-wavelength spin waves is determined by the dipolar energy of the system; thus, these spin waves are known as dipolar-dominated spin waves. In contrast, the exchange interaction is very important for short-wavelength spin waves. The energy of these exchange-dominated

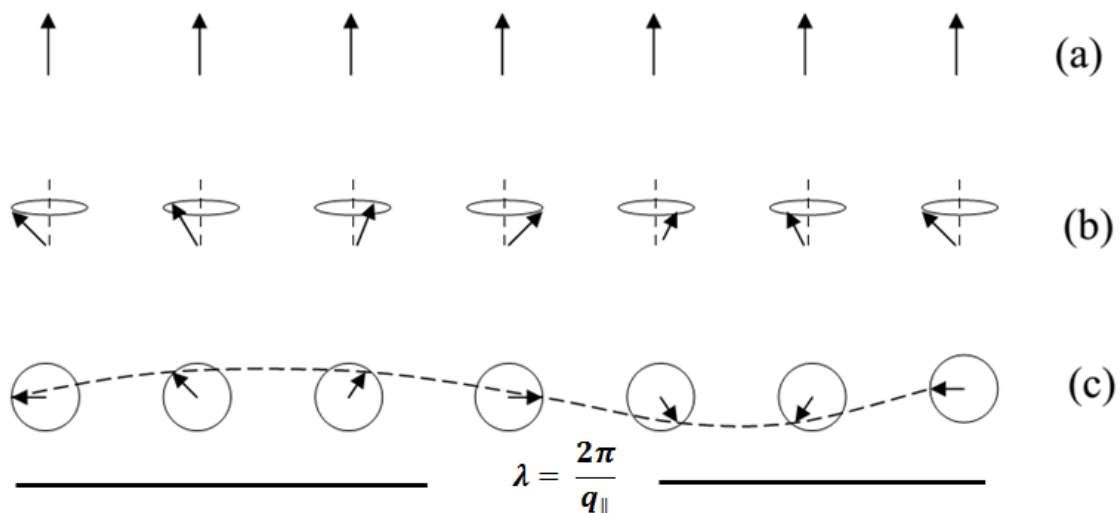


Figure 2.15: Semiclassical representation of spin wave in a ferromagnet: (a) the ground state (b) a spin wave of precessing spin vectors (viewed in perspective) and (c) the spin wave (viewed from above) showing a complete wavelength.

spin waves is determined by the exchange energy of the system and given as [Hei28, Pat84].

The semiclassical theory of the spin waves was further developed by Heller and Kramers [Hel34] in terms of precessing spins. Figure 2.16 shows the schematic view of spin wave in a ferromagnet. For a ferromagnetic material, there is interaction between neighboring

electronic spins, which gives rise to a parallel alignment in the ground state (Fig. 2.15a). With perturbation, the spins will deviate slightly from their orientation in the ground state (Fig. 2.15b), and with this disturbance propagating with a wavelike behavior (Fig. 2.15c) through the material.

Spin waves with wave-vector (q) in the range $30 < q < 10^6 \text{ cm}^{-1}$ are usually called dipolar magnetostatic spin waves or magnetostatic modes since it is almost entirely determined by magnetic dipole interaction. They were first reported by Damon and Eshbach [Dam61] in 1961. The frequency of the magnetostatic mode depends on the orientation of its wave-vector relative to that of the static magnetization due to the anisotropic properties of the magnetic dipole interaction. Spin waves with higher values of wave-vector, when the exchange interaction cannot be neglected, are called dipole- exchange spin waves.

Spin waves are the dynamic eigen-excitations of a magnetic system. They are used to describe the spatial and temporal evolution of the magnetization distribution of a magnetic medium under the general assumption that locally the length of the magnetization vector is constant. This is satisfied with if, first the temperature is far below the Curie temperature (T_c); and second, if no topological anomalies like vortices, are present. The latter is fulfilled for samples in a single domain state, i.e magnetized to saturation by an external bias magnetic field. Then the dynamics of the magnetization vector are described by the Landau-Lifshitz torque equation [Lax94]:

$$-\frac{1}{\gamma} \frac{d\mathbf{M}}{dt} = \mathbf{M} \times \mathbf{H}_{eff} \quad (2.44)$$

where $\mathbf{M} = \mathbf{M}_S + \mathbf{m}(\mathbf{R}, t)$ is the total magnetization, \mathbf{M}_S and $\mathbf{m}(\mathbf{R}, t)$ are the vector of the saturation and variable magnetization respectively, γ is the modulus of the gyromagnetic ratio for the electron spin ($\gamma/2\pi = 2.8\text{MHz/Oe}$). The effective magnetic field (\mathbf{H}_{eff}) is calculated as variational derivative of the total energy function E :

$$\mathbf{H}_{eff} = -\frac{\delta E}{\delta \mathbf{M}} = \mathbf{H}_o + \mathbf{H}_{dem} - \left(\frac{1}{M^2}\right) \nabla E_{ani} + \left(\frac{2A}{M_S}\right) \nabla^2 \mathbf{M} \quad (2.45)$$

where \mathbf{H}_o is the applied magnetic field, \mathbf{H}_{dem} the demagnetization field, E_{ani} the anisotropy energy, \mathbf{M}_S the saturation magnetization and A the exchange stiffness constant. All the relevant interactions (the Zeeman field \mathbf{H}_o , the dipole interaction \mathbf{H}_{dem} , the anisotropy

contribution ∇E_{ani} and the exchange interaction A) in the magnetic media have been considered.

Since the effective magnetic field \mathbf{H}_{eff} depends on the magnetization \mathbf{M} , Eq. (2.44) is basically nonlinear. However, if the amplitude of the variable magnetization $\mathbf{m}(\mathbf{R}, t)$ is small compared to the saturation magnetization \mathbf{M}_S , the variable magnetization $\mathbf{m}(\mathbf{R}, t)$ can be expanded as a series of plane waves of magnetization (or spin waves):

$$\mathbf{m}(\mathbf{R}, t) = \sum_{\mathbf{q}} \mathbf{m}_{\mathbf{q}}(t) \exp(i\mathbf{q} \cdot \mathbf{R}) \quad (2.46)$$

where \mathbf{q} is the 3-D spin wave wave-vector and Eq. (2.44) can be linearized. Such a linearized equation is used for the description of the linear spin waves.

The spectrum of dipole-exchange spin waves in an unlimited ferromagnetic medium is given by the Herring-Kittle formula [Her51]:

$$\omega = 2\pi f = \gamma \left[\left[\left(H + \frac{2A}{M_S} q^2 \right) \left(H + \frac{2A}{M_S} q^2 + 4\pi M_S \sin^2 \theta_q \right) \right] \right]^{1/2} \quad (2.47)$$

where ω is the angular frequency of the spin wave, f the frequency, and θ the angle between the directions of the spin wave wave-vector and the static magnetization. As $q \rightarrow 0$, ω has the limiting values: $\omega = \gamma H_0$ for $q \parallel \mathbf{M}$, and $\omega = \gamma(H_0 B)^{1/2}$ for $q \perp \mathbf{M}_S$, where $B = H_0 + 4\pi M_S$. Specifically when the external magnetic field is perpendicular to the normal to the film plane which is known as Damon-Eshbach (DE) dipolar surface spin wave, in the absence of exchange, the spin wave frequency is given by Eq. (11) in Ref [Dem01]:

$$\omega_{DE} = 2\pi f = \gamma [H(H + 4\pi M_S) + (2\pi M_S)^2 (1 - e^{-2q_{\parallel} d})]^{1/2} \quad (2.48)$$

where q_{\parallel} is the in-plane wave-vector, and d is the thickness of the film.

For the exchange-dominated, thickness- or perpendicular standing spin waves (PSSW) modes the frequencies are described by the following equation [Dem01]:

$$\omega_p = 2\pi f_p = \gamma \left[\left(H + \frac{2A}{M_S} q_{\parallel}^2 + \frac{2A}{M_S} \left(\frac{p\pi}{d} \right)^2 \right) \times \left(H + \left[\frac{2A}{M_S} + H \left(\frac{4\pi M_S / H}{p\pi / d} \right)^2 \right] q_{\parallel}^2 + \frac{2A}{M_S} \left(\frac{p\pi}{d} \right)^2 + 4\pi M_S \right) \right]^{1/2}, \quad (2.49)$$

$p = 0, 1, 2, \dots$ Is a quantization number for the so-called perpendicular standing spin waves.

3. Experimental

3. Experimental

3.1. Sample preparation

Thin films are grown by the depositing the material's atoms from target onto a substrate. The thin films are low-dimensional materials having thickness typically less than several micrometers. The basic properties of film, such as film composition, crystal phase and orientation, film thickness, and microstructure, are controlled by the deposition techniques and conditions. Thin films exhibit unique properties (e.g, increase in magnetic anisotropy, GMR effects in multilayers, exchange coupling at the interface between ferromagnetic and anti-ferromagnetic, etc. [Was12]) that cannot be observed in bulk materials. This section will provide brief introduction about the technology being employed to fabricate samples under investigation.

3.1.1. Fabrication of thin films

Thin films have shown great interest due to their technological applications. They can have thickness ranging from fraction of nanometer (monolayer) to several micrometers in thickness. Thin films are usually deposited (an act of applying a material to a substrate surface) through different techniques, Fig. (3.1):

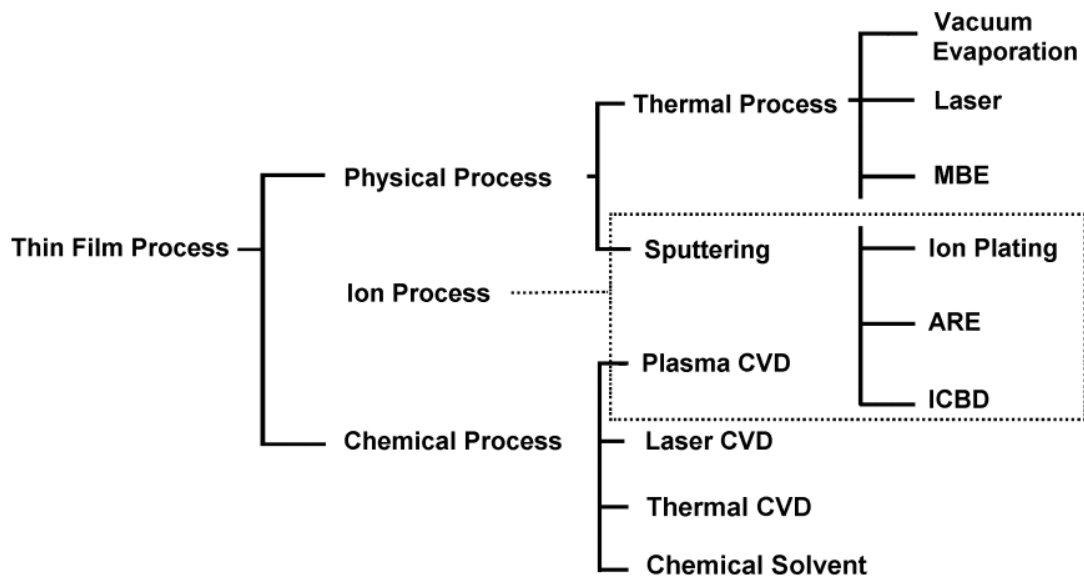


Figure 3.1: Thin film deposition processes. Fig. is adopted from Ref. [Was12].

3.1.1.0. Chemical deposition

In this method fluid known as precursor undergoes a chemical change at the surface of the substrate while leaving a solid layer. This technique is further characterized because of the phase of the precursor used such as:

- **Chemical vapor deposition (CVD)** which uses precursor in the gaseous phase. During this process volatile compound of the substance to be deposited is vaporized which is after thermally decomposed or reacted with other gases, vapors and liquids at the substrate yields to non-volatile product (thin film). This process is known as CVD.
- **Plasma-assisted CVD** is one of the modified CVD where electric power is supplied to reactor to generate the plasma. During this process, the degree of ionization reaches upto 10^{-4} , so reactor consists mostly neutrals.
- **Laser-assisted CVD** has been recently developed after modifying conventional CVD. During this process, CVD reactions are carried out through irradiation of the UV laser light.
- **During thermal CVD**, heating lamps or other heating methods are used to supply rapid heating to the substrate. Heating the only substrate (rather gas or chamber wall) helps to reduce the un-necessary gas-phase reactions that can lead to particles formation.
- **Chemical solvent deposition (CSD)** or chemical bath deposition (CBD). This technique is also known as sol-gel method because of solution gradually evolves towards the formation of a gel-like diphasic system. This is an inexpensive and simple technique to grow thin films.

3.1.1.1. Physical processes

In physical deposition techniques, the thin films can be produced by using mechanical, electromechanical or thermodynamic means. Commercial physical deposition systems tend to require a low-pressure vapor environment to function properly; most can be classified as physical vapor deposition (PVD). During these techniques, the material to be deposited (target) is placed in an energetic, entropic environment, so that particles of material escape its surface. The evaporated material travels towards the host materials (substrate) held at low temperature which draws energy from these particles as they arrive, allowing them to form a solid layer. The whole procedure takes place in a vacuum chamber known as deposition

chamber. Since ejected particles tend to follow a straight path, films deposited by physical means are commonly directional, rather than conformal. These can be classified into following categories:

- In **thermal evaporation process**, evaporating source material in a vacuum chamber condensates on the substrates. Conventionally thermal evaporation processes are also called vacuum deposition. Resistive heating is most commonly used method for fabrication of thin films where source (target) material is evaporated by resistively heated filament or boat (usually made of W, Mo, and Ta, and crucibles of quartz, graphite, alumina etc..).
- **Pulse laser deposition (PLD)**: This technique works on ablation process where pulses of focused laser light vaporizes the surface of the target material and convert into plasma which reverts to gas before reaching to the surface of the substrate. Usually, a substrate is placed at a target-to-substrate distance of 2–10 cm [Nis15]. A basic PLD chamber works under high vacuum between 10^{-6} and 10^{-11} Torr, while substrate heater, target manipulator, and gas inlet are introduced to facilitate quality deposition.
- **Molecular beam epitaxy (MBE)** is an elegant material growth technique known familiar for its very refined form of vacuum evaporation or physical vapor deposition, with exquisite control over material purity, interface formation, alloy compositions, and doping concentrations. Non-interacting molecular beams of source materials are evaporated or sublimed and allowed to chemically interact on a substrate which is at elevated temperature. MBE can produce extremely good very sharp interfaces. The effusion cells that produce the molecular beams of source (target) materials are typically synchronized with a mechanical shutter that can quickly start or stop the beams which help to control the rate of deposition. Better control over the temperature of the source, makes MBE very reliable to reproducible accurate alloy compositions and doping concentrations. The UHV environment also lends itself to the incorporation of various in situ monitoring techniques that can be used during growth, including reflection high-energy electron diffraction (RHEED), low-energy electron diffraction (LEED), and mass spectrometry. Combining specific techniques like spectral ellipsometry, laser reflectance,

pyrometry, and band edge thermometry, MBE becomes a very powerful tool for the study of basic science and the production of very high-quality materials and devices.

- **Sputtering:** During the bombardment of the energetic ions on the target materials, the atoms of the surface are scattered backward due to the collisions between the surface atoms and the energetic particles. This phenomenon is known as back-sputter or simply “sputtering”. Types of sputtering deposition

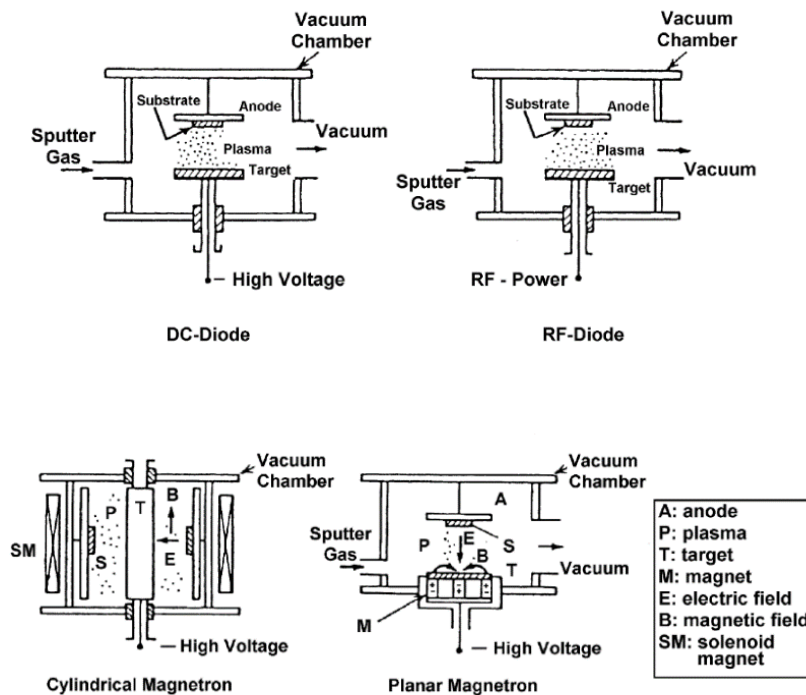


Figure 3.2: Sputtering deposition systems. Fig. is adopted from Ref. [Was12].

systems are shown in Fig. 3.2. The deposition rates in sputtering systems are lower than those of vacuum deposition. In order to enhance the deposition rate (lowering of sputtering pressure), magnetron-type discharge is introduced (see Fig. 3.2). In the magnetron sputtering system, a magnetic field parallel to the cathode surface is superposed. The electrons in the glow discharge shows cycloid motion and the center of the orbit drifts in a direction of $\mathbf{E} \times \mathbf{B}$ with drift velocity of \mathbf{E}/\mathbf{B} , where \mathbf{E} and \mathbf{B} represent electric and magnetic field respectively. Proper orientation of applied magnetic field keeps the drift path for electron to form a closed loop. Trapping effect of these electrons enhances

the collisions rate between the electron and sputtering gas. In the magnetron sputtering deposition system, the magnetic field increases the plasma density, which leads to increases of the current density at the cathode target, effectively increasing the sputtering rate at the target. Being the low working gas pressure, the sputtered particles traverse the discharge space without collisions, which results in high deposition rate.

- During **ion plating**, the coating flux is usually provided through thermal evaporation. The evaporated atoms are further ionized at the plasma region and accelerated by application of electric field before final deposition.
- **Activated reactive evaporation (ARE)** is commonly used for the deposition of metal oxides, carbides and nitrides [Was12]. In this deposition system, the reactive gas serves as plasma source.
- **Ionized cluster beam deposition (ICBD)** is modified form of ion plating. Atoms are evaporated from a closed source through a nozzle. Expansion through the nozzle, atoms becomes cooler and leads to the formation of clusters. These clusters are further ionized through the plasma region and finally accelerated before the deposition.

3.1.2. Tuning magnetic properties through ion irradiations

In the recent decade, the ions have shown tremendous way of tuning magnetic properties of the materials. Since after the pioneer work of Chapper, et.al [Cha98], where planner patterned magnetic media was achieved through ion irradiation, the ions have largely used to modify different magnetic parameters of thin films and multilayer [Fas04, Fas08]. A large variety of magnetic properties are based on the precise atomic arrangement either in a multicomponent system or across an interface in a multilayer system. In the first case short range order effects in amorphous alloys or chemically ordered crystallographic structures play an important role because of the quantum mechanical overlap of the wave functions of the ferromagnetic constituents govern the overall magnetic behavior. Example of such case study is FeAl alloy which is only ferromagnetic in its bcc-structure (disordered A2-phase) whereas the chemical ordered B2-phase exhibits paramagnetic properties [Bal14, Men09, Fas08a, Sor06]. In the second case, FePt alloy which possess a large magnetic anisotropy only if the chemically ordered L1₀-phase is established [Fas04].

3.1.2.1. Establishing ferromagnetism through disorder

As it has been described earlier that ferromagnetism in certain alloys can also be established through creating disorder in their chemical ordered structures. In the present dissertation one part of my study is related with the study of statics and dynamics of magnetization of one of such materials. $\text{Fe}_{60}\text{Al}_{40}$ alloy material is paramagnetic before the ion irradiation treatment. The crystallographic structure is the chemically ordered B2 -phase.

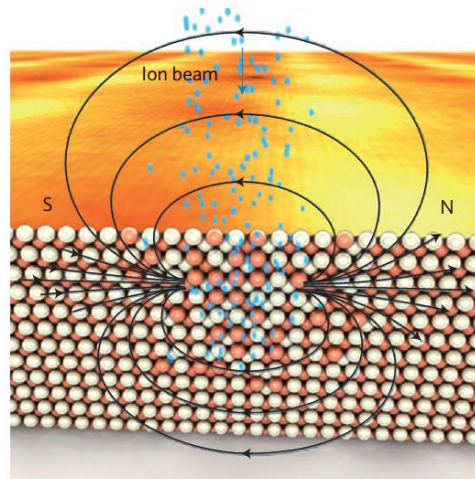


Figure 3.3: The white (Al) and red (Fe) balls indicate the different atomic species in the FeAl alloy. Owing to ion irradiation (blue), a transformation to the chemically disordered A1-phase is achieved, where each lattice site is occupied randomly by either Fe or Al (center of image). The change in chemical ordering is accompanied by a transition from paramagnetic (chemically ordered) to ferromagnetic (chemically disordered). Image courtesy of HZDR/Sander Muenster.

After ion irradiation the phase is transformed to the chemically disordered bcc-phase, which is ferromagnetic. Due to the local irradiation ferromagnetic nanostructures can easily be created in a paramagnetic environment [Bal14, Men09, Fas08a, Sor06].

3.1.2.2. Tailoring the magnetic anisotropy

The motivation behind the change of magnetic anisotropy through ions, comes from its potential use in future applications for ultra-high density magnetic recording as this ion-irradiation provides the ability to produce magnetic nanostructures without affecting surface topography. Magnetic anisotropy is directly related to the asymmetry of the atomic environment. The source of this asymmetry could be due to magneto-crystalline (lattice space group), magneto-elastic (uniaxial strain), or interfacial (symmetry breaking at interface) origin. Co–Pt systems with large perpendicular magnetic anisotropy (PMA) and high coercivity have attracted considerable interest as future magnetic media reaching a density of 1Terabit in⁻² [Woo00]. All recent experiments on uniformly irradiated Pt–Co systems [Cha98,

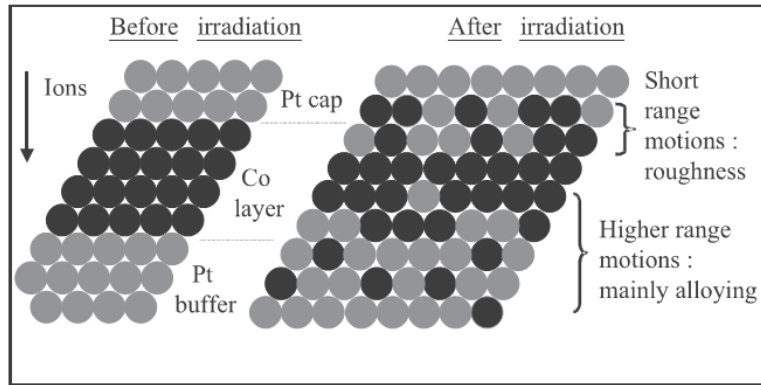


Figure 3.4: Qualitative scheme of a Pt/Co/Pt sandwich structure before and after irradiation. Co (Pt) atoms are shown in black (grey). Ions move towards the bottom of the figure. Displaced Co atoms moving in the ion direction travel more than one inter-atomic distance and become isolated (Co–Pt alloying), whereas Co atoms moving in the opposite direction travel typically only one inter-atomic distance and contribute to roughness (local thickness fluctuations). Fig is adopted from Ref. [Fas04].

Fer99, Cha01, Hyn01,] have shown that irradiation at room temperature induces intermixing at the interfaces whatever the ions and energy used. In these ultrathin (nanometer-range) films, irradiation may affect the upper and lower interface differently [Dev00]. The upper Co interface undergoes short range mixing which results in roughness (the local Co thickness fluctuation), whereas the lower Co interface is mostly modified by higher range mixing, leading to formation of CoPt alloy (See Fig. 3.4). A very recently Maziewski, et.al [Maz12] have shown that by an appropriate selection of ion-irradiation conditions, one can enhance the perpendicular magnetic anisotropy in Pt/Co/Pt ultra-thin having in-plane magnetization state. Two out-of-plane branches of magnetic anisotropy could be related with intermixing at Co/Pt interfaces and formation of ordered $\text{Co}_{1-x}\text{Pt}_x$ alloys exhibiting out-of-plane magnetic anisotropy.

3.1.3. Patterning of nanostructures

Nanomagnets are getting lots of scientific interest both from a fundamental viewpoint and also due to their potential use in wide range of emerging applications such as logic devices, electro-mechanical systems (M/NEMS), memory devices, and countless others as well. Due to their extremely smaller in size, they possess both statics and dynamics properties which are quantitatively and qualitatively different from the parent bulk materials. Nanofabrication can be classified into two categories depending on their growing routes. Top-down process refers to approaching to nanoscale from the top (larger dimensions), through lithography, nanoimprinting, scanning probe, E-beam, Ion irradiation, Focus ion beam (FIB) etc,.. In the bottom-up fabrication technique, the nanotechnology process builds nanoscale artifacts from the molecular level up, through single molecules or collections of molecules that agglomerate

or self-assemble. The key issues in the development of the nanofabrication techniques are: critical dimension control, resolution, shape homogeneity, patterned area and alignment accuracy. Various nanofabrication techniques for fabricating nanomagnets have been developed which have advantages and disadvantages with respect to each other.

3.1.3.1. Magnetic Patterning through ion irradiation

First pure magnetic patterning by means of ion irradiation which relies on a local modification of the magnetic anisotropy of a magnetic multilayer structure was demonstrated by Chappert et. al [Cha98]. Magnetic patterning through ions can be divided in two parts: for large length scale patterning (through uniformly irradiation) and smaller length scale (focus ion beam (FIB), and ion projection lithography). Focus ion beam (FIB) is a technique which is used for patterning and deposition of different materials with nano-scale resolution. During FIB (generally Ga^+ ions accelerated at tens of keV, now Ne^+ -ions based FIB is available at Rossendorf (Germany)). By selecting appropriate FIB fluence, effect of possible change in topography could be avoided. Through FIB irradiation the change in magnetic anisotropy can be achieved in a similar fashion as early described in section 3.1.2.2 (tailoring the magnetic anisotropy) at much smaller length scale ($\sim \text{nm}$).

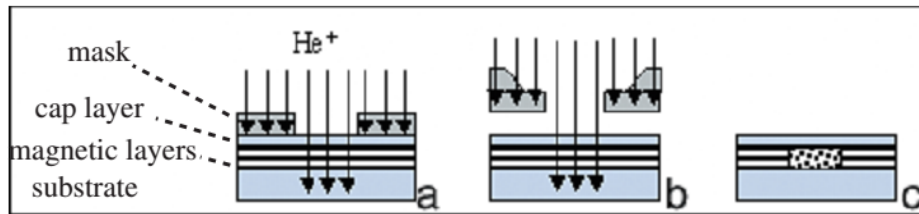


Figure 3.5: Ion induced magnetic patterning through masking. (a) Through a mask deposited directly on the sample surface. (b) Through a suspended non-contact stencil mask. (c) After the removal of the mask, the sample is magnetically patterned (in dotted area) while having planar surface. The image is adopted from Ref. [Fas04].

Usually large scale magnetic patterning is carried out with the support of mask having enough thickness to completely stop the energetic ions. In such a way, the protected area (covered by mask) keeps its original properties. As it can be seen from Fig. (3.5), the irradiation can be performed through masks either by direct deposition onto the surface of the sample by lithography (contact mask) or by employing membrane with drilled holes suspended above the surface of the sample (non-contact stencil mask) [Fas04]. During ion interaction with the surface, many effects such as radiation damage, elastic reflected ions,

implantation, and ion etching (milling) can take place. All these effects depend on the kinds, energy and fluence of the ions (He^+ , Ne^+ , Ar^+ , Ga^+ , N^+ etc).

3.1.3.2. Magnetic patterning through photolithography

Nanofabrication through lithography is a collective term for several closely related processes, including resist coating, exposure, and development. Hence lithography is usually categorized by the radiation source as, optical, electron-beam (e-beam), ion beam, and X-ray lithography. Based on the employed lithography technique, the transfer is performed in different way, which defines the resolution that can be attained. In the case of electron beam lithography (EBL), is a high resolution method for fabricating magnetic nanostructures. The principle of the EBL is the direct writing of the required nano structures on a thin resist layer with focused beam of electron. The writing process in EBL is a serial process which is very slow and thus hinders for the fabrication of large area nanopatterns. Interference lithography (IL) is another technique which has been employed for the fabrication of nanostructures at large scale. In this technique, the resist layer is exposed by interference patterns generated by two obliquely incident laser beams without use of a mask. The intensity of the interference

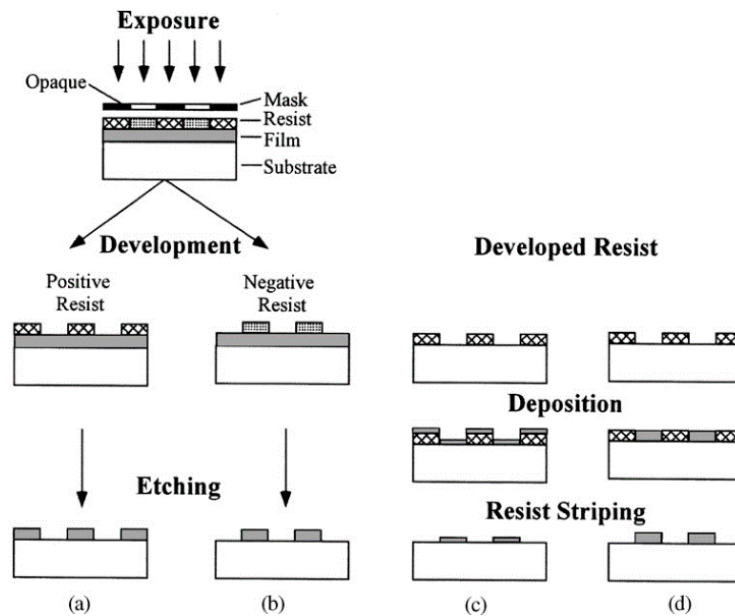


Figure 3.6: Schematics of lithography processes for (a) positive and (b) negative resist in conjunction with (a), (b) etching, (c) lift-off, and (d) electrodeposition. This image is adopted from Ref. [Mar03]

pattern is defined by the $p = \lambda_{\text{laser}} \sin \theta$, λ_{laser} is the wavelength of the laser, and θ is half of the angle between the two beams [Lod04]. In order to fabricate arrays of dots, a second exposure after rotating the substrate by 90° is needed. The patterned area is estimated by the diameter of the two laser beams. This technique can be easily and cheaply employed where alignment is not required. Nanoimprint lithography (NIL) has also emerged as promising technique for

fabrication of magnetic nanostructures over a large scale area. In NIL, the resist is patterned by physical deformation with a mould assisted by either thermal effect or UV radiation. Magnetic nanostructures can be then fabricated by employing the resist as a deposition template or as an etch mask.

A standard photolithography system consist of four fundamental elements: (i) illumination system (ii) mask containing the patterns corresponding to desired structures, (iii) exposure system to generate an aerial image of the mask pattern, and (iv) a medium known as photoresist or a resist for recording the image generated by the exposure system.

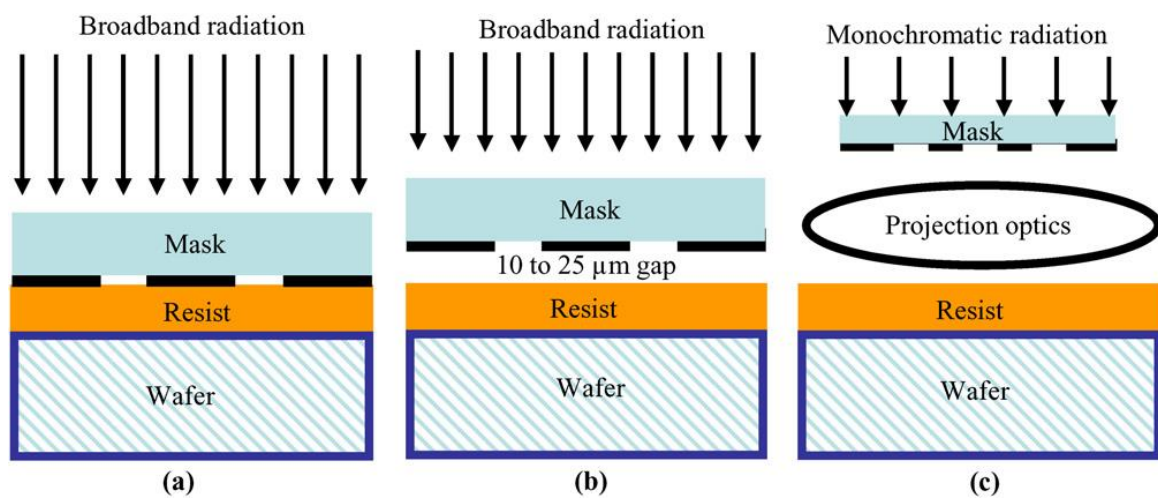


Figure 3.7: Schematic diagram, of the exposure systems (a) contact, (b) proximity, and (c) projection. This image is adopted from Ref. [Ade04].

The substrate (un-patterned) is first spin-coated with a uniform layer of resist (a polymeric photosensitive material) dissolved in certain organic liquid solvent. The thickness of the resist typically varies from a few thousand angstroms to a micron, depending on the spinning speed and the resist viscosity. The adhesion is promoted through the soft-baking ($\sim 110^{\circ}\text{C}$ for few seconds) which also serve to remove the resist. Desired areas of the resist are then exposed to a radiation source (1st element), usually through a mask (2nd element (mask) is a glass blank containing the layout information of the structures to be patterned on the substrate in the form of physical or optical coding. Conventional mask also known as a binary intensity mask (BIM) or chrome on glass (COG) mask while beside the conventional masks, optical lithography also uses phase shift masks (PSMs) for resolution enhancement). Early optical lithography tools used radiation from mercury lamp (broadband (300-450 nm), g-line (436nm), i-line (365 nm)) as the source of energy. Today deep ultra violet (DUV) excimer lasers

(krypton fluoride (248 nm KrF) and argon fluoride (193 nm ArF) are being used [Bru97]. The patterning can be realized through Fig. (3.6). The exposure system (3rd element) generates the optical image of the mask patterns on the substrate. In contact exposure systems, developed in the early 1960s, the mask is in hard contact with the substrates see Fig. 3.7(a). The desired patterns on the mask are being transferred to the substrate through single exposure using broadband light with a spectrum from 300 to 450nm. The contact lithography offers high resolution, but suffers from mask damage due to hard contact between the mask and the resist substrate which causes the generation of defects on the substrate, and consequently constrained this process in manufacturing. Through proximity lithography one can reduce the mask damage by keeping the mask a few (10–25) micrometers away from the substrate as shown in Fig. 3.7(b). Due to the diffraction effects from the gap between the mask and substrate, the resolution is poorer. The most commonly used exposure system is the projection lithography system. It uses the concept of projecting the reticle image through a lens system (projection optics) see Fig. 3.7 (c). Although not shown, the projection optics consists of complex optical elements with more than 40 lenses [Ulr00]. After sufficient exposure (4th element), the polymer chains in the resist are either dissolve (positive resist) or become cross-linked (negative resist, poorer resolving power). The homogeneity is often enhanced through the post-baking before the development of positive or negative image of the mask. By proper selection of developer, temperature, and development time, one can obtain straight, round-off or undercut depth profiles in the resist. For etching process, the developed resist is usually hardened by a hard-bake while for the case of wet etching chemical or electrochemical processes are involved to dissolve the materials. Thickness of the film (to be patterned) limits the resolution of the patterning as it is intrinsically isotropic and causes sloped pattern edges. In case of dry etching, physical processes such as ion milling and sputter etching use ion bombardment to remove the unwanted materials. Through dry etching, straight and sharp pattern edges are produced thus better resolution for a given thickness can be achieved [Vos78]: Alternatively, nanopatterns can also be fabricated by post-lithography deposition. Lift-off process helps to adjust the height of a developed resist by breaking apart a subsequent deposited, much thinner, layer of material Fig. (3.6). The film deposited on top of the resist is lifted off during resist stripping while leaving behind only the portions directly deposited onto the substrate. In order to have better edges of the patterns, directional deposition technique is preferred.

3.2. Statics measurements

3.2.1. Magneto-optical Kerr effect (MOKE)

When linearly polarized light is reflected from a magnetic film, its polarization becomes elliptic and the principal axis is rotated. This effect is known as the magneto-optical Kerr effect (MOKE). Accordingly, the rotation angle and ellipticity are referred to as Kerr angle θ and Kerr ellipticity ε . In general, these two quantities can be expressed in terms of complex amplitudes of the electric field vector. The quantities θ and ε are proportional to the magnetization of the film. Which component of the magnetization is probed in the experiment depends on the measurement geometry. The amount of rotation is small, generally much less than one degree, and depends the material and on the direction and magnitude of the magnetization relative to the plane of incidence of the light beam. Specifically, the degree of rotation depends on the component of magnetization parallel to the direction of propagation of the light beam. There are three types of Kerr effect, which are differentiated according to the orientation of the magnetization with respect to the direction of the wave propagation and with respect to the normal to the surface.

Figure 3.8 illustrates three different Kerr effects, which are the (a) polar, (b) longitudinal and (c) transverse MOKE. When the magnetization vector is perpendicular to the

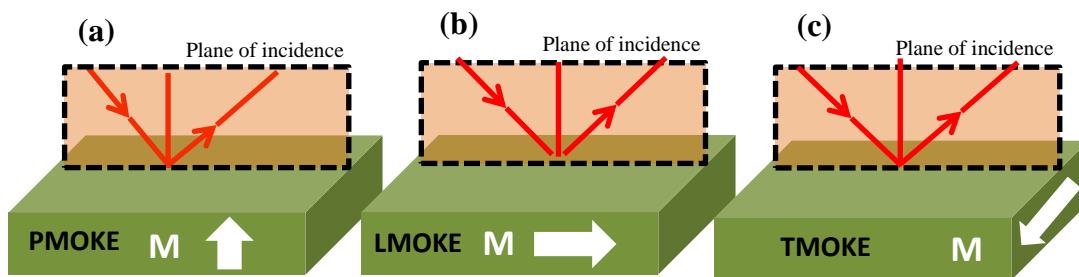


Figure 3.8: Illustration of various configurations for the magneto-optical Kerr effect: a) PMOKE, b) LMOKE, and c) TMOKE

reflection surface and parallel to the plane of incidence, the effect is called the polar Kerr effect. To simplify the analysis, near normal incidence is usually employed when doing experiments in the polar geometry (Fig. 3.8a). While in the case of longitudinal Kerr effect, the rotation of the plane of polarization occurs and an ellipticity appears when linearly polarized light reflects from the sample surface, provided the magnetization vector is parallel to both the reflection surface and the plane of incidence (see Fig. 3.8b). The effect can be used to observe the domain structure of the material whose magnetization lies in the sample plane.

Like above mentioned effects (Polar and longitudinal Kerr effect), transverse Kerr effect is linear in magnetization. The transverse Kerr effect can be observed only for absorbing materials. It is manifested as intensity variations and phase shift of linearly polarized light reflected from a magnetized material, if the magnetization lies in the sample plane but is perpendicular to the plane of incidence of the light (see Fig. 3.8c).

The fact, that particular types of MOKE are sensitive to a certain orientation of the magnetization, means that each of them probes one component of the magnetization. For any general direction of the applied magnetic field or the magnetization, the respective effects can occur together, however in certain conditions it is possible to separate them. In terms of dielectric permittivity tensor, each component of the magnetization is represented by a proper off-diagonal tensor element. Additionally, for the case of cubic symmetry of the media, the tensor can be simplified, as then the diagonal elements are identical and equal to a square of the refractive index of the material:

$$\boldsymbol{\varepsilon} = \varepsilon \begin{bmatrix} 1 & -iQ_V m_3 & iQ_V m_2 \\ iQ_V m_3 & 1 & -iQ_V m_1 \\ -iQ_V m_2 & iQ_V m_1 & 1 \end{bmatrix} + \begin{bmatrix} B_1 m_1^2 & B_2 m_1 m_2 & B_2 m_1 m_3 \\ B_2 m_1 m_2 & B_1 m_2^2 & B_2 m_2 m_3 \\ B_2 m_1 m_3 & B_2 m_2 m_3 & B_1 m_3^2 \end{bmatrix} \quad (3.1)$$

where Q_V is the (Voigt) material constant describing the magneto-optical rotation of the plane of the polarization of the light-Faraday effect in transmission and Kerr effect in reflection. The effect is also called circular magnetic birefringence, a birefringence for circularly polarized light. With this term alone the dielectric law may also be written in the form:

$$D = \varepsilon(E + iQ_V m \times E) \quad (3.2)$$

The constants B_1 and B_2 describe the Voigt effect. In isotropic or amorphous media the two constants B_1 and B_2 are equal, but in cubic crystals they are in general different. The m_i are the components of the unit vector of magnetization along the cubic axes. All constants are frequency dependent and complex in general, but the real parts of the constants Q_V , B_1 and B_2 are usually predominant.

MOKE gives access to precise information about the actual magnetization state of a medium. The important property and the big advantage of the magneto-optical effect in practical use is that they happen exactly during the time when the light passes through the

sample which makes MOKE an extremely useful technique, widely used in studies of magnetism, from quasi-statics to ultrafast magnetization dynamics.

3.2.2. Magneto-optical milimagnetometer

The magneto-optical milimagnetometer setup (Fig. 3.9) mainly consists of a diode laser light source (640-nm wavelength) emitting a beam of about 300 μm in diameter, photoelastic modulator (PEM), optics, magnets, and photodiode as a detection element. The PEM is an optical device that is used to enhance signal to noise ratio by modulating the polarization of the light source.

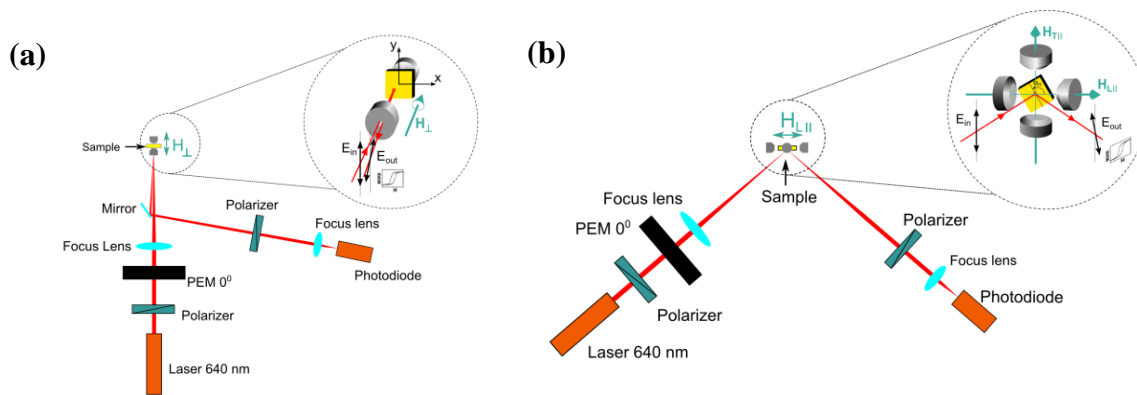


Figure 3.9: Schematic of the magneto-optical setup: a) PMOKE configuration, b) LMOKE and TMOKE configuration. Image courtesy of Ref. [Maz13]

The laser light is focused (focusing lens with $f = 50$ cm) on the sample before that it passes through the polarizer (set at 45° in relation to the path of the incidence light), and PEM (modulation frequency of about 50 kHz). The lens with large focusing length helps to prevent the influence of magnetic field. Depending on the configuration the reflected light follows the different paths, see Fig. 3.9(a) and Fig. 3.9(b) for PMOKE and LMOKE/TMOKE respectively.

In PMOKE configuration Fig. 3.9(a) laser light goes and comes back after reflection from sample practically on the same path. Reflected light is directed towards the photodiode by employing mirror in its path of reflection. After reflected by mirror the light further passes through polarizer and finally focused to photodiode by focusing lens. In this configuration magnetic field is applied perpendicular to the sample surface which allows to probe the only out-of-plane component of magnetization (maximal amplitude of the applied magnetic field up to 12 kOe). With the help of computer controlled X-Y motors it is possible to scan the whole sample.

Figure 3.9(b) shows the LMOKE/TMOKE configurations where the incidence and reflected laser light was about 50° from the sample normal. In this studies magnetic field was applied form the special construction of the electromagnet with orthogonal to each other generated magnetic field (maximal amplitude of the applied magnetic field up to 1.5 kOe). In this configuration sample was mounted on special holder which allows to move (X-Y) and rotates the sample in the sample plane. Magnetic field was generated using Kepco amplifiers. All studies processes were controlled by special program written in LabView software.

3.2.3. Kerr Microscopy

The most common Kerr microscopes are sketched see Fig. (3.10). The first setup is recommended for low resolution applications in the longitudinal or transverse effects to obtain an overview of the domain pattern of larger samples. The advantage of this setup is that no optical elements other than the sample exist between polarizer and analyzer, so that

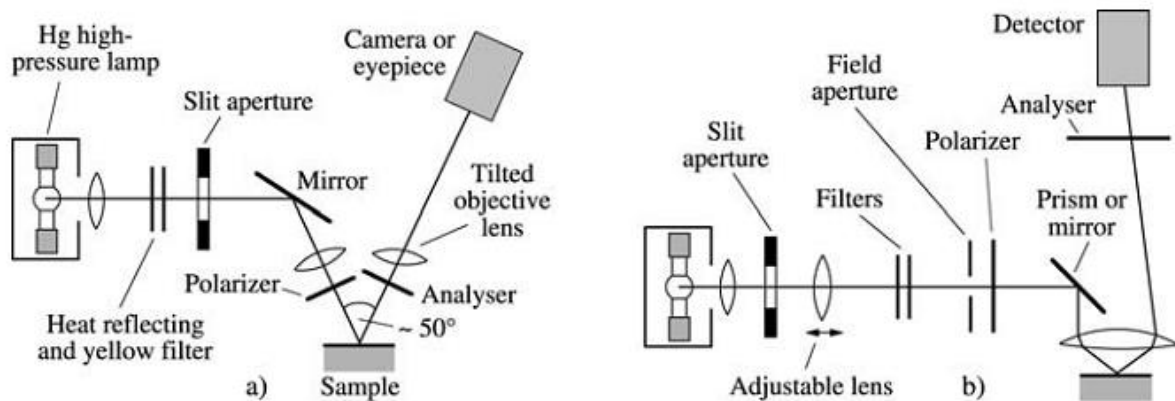


Figure 3.10. Two Kerr microscopes. (a) A low resolution and high sensitivity version. In this case a wide angle objective lens, which can be tilted to reduce distortion, works best. (b) A high resolution, distortion-free Kerr microscope. To avoid depolarization, the objective lens and the mirror element must be strain-free. Image is adopted from Ref [Hub09].

contrast conditions are optimal. The objective lens is tilted to increase the range of focus and to reduce the image distortion [Fel67]. Resolution in this arrangement is practically limited by the achievable numerical aperture and by aberrations in the tilted objective to about $2\mu\text{m}$. Microscopes of this type have to be custom-made. Observations at high resolution up to the limit of optical microscopy are possible with the second setup [Gre62] which is usually based on a conventional polarizing microscope. Using oil immersion for a high numerical aperture and blue light for a short wavelength, a resolution of $0.3\mu\text{m}$ could be achieved for the polar effect, thus observing domains as narrow as $0.15\mu\text{m}$ [Hub67, Sch86]. Contrast is reduced to some extent since the beam passes through the mirror element and twice through the objective

between polarizer and analyzer. Strain-free, polarization-quality optics are mandatory. A high pressure mercury lamp with suitable spectral filters to select the green and yellow mercury lines is recommended as the best light source in most cases. It offers sufficient brightness and a suitable color spectrum, which can be used not only in the yellow-green but also in the blue range. The disadvantage of arc lamps is their insufficient stability and lifetime. A more stable alternative can be laser illumination. Solid state green or blue lasers will be interesting when they become available and sufficiently reliable. The advantages of laser illumination are (i) virtually unlimited intensity, (ii) the possibility to stabilize the output power of the laser, which is impossible for arc sources, and (iii) the use of short laser pulses for high-speed and stroboscopic microscopy.

3.2.3.1. The illumination Path

The illuminating aperture in a Kerr microscope should be neither too small nor too large. Too small an aperture (parallel light) leads to disturbing diffraction fringes especially around sharp effects on the sample surface. A large aperture reduces the contrast by generating a background intensity because of depolarization effects. The reason for this is sketched in Fig.3.11a.

Consider all light beams hitting one point of the sample. We call the plane defined by the central beam of the illuminating bundle and the surface normal the central plane of

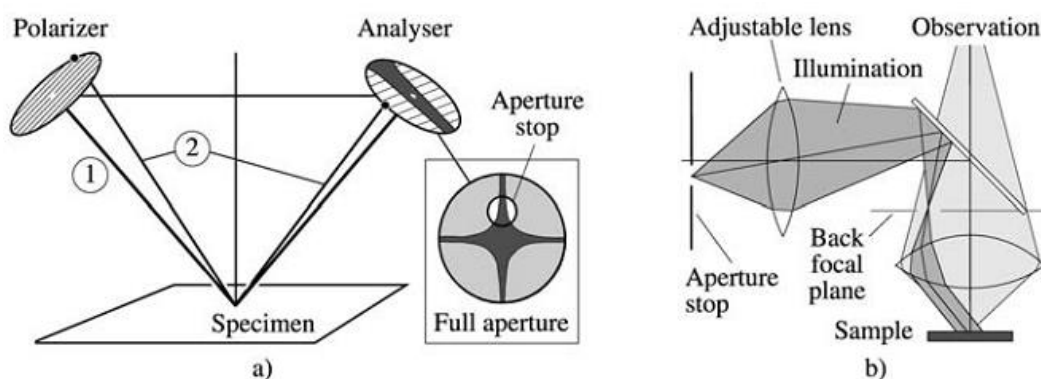


Figure 3.11: Schematics of the illuminating aperture, polarizer and analyzer (a). If the polarizer is set parallel to the central plane of incidence, the central beam (1) is reflected without a phase shift from any metallic surface.

This is not true for an off-centre beam (2) with its different plane of incidence. This beam is reflected in an elliptical and rotated polarization state in general, and is thus not fully extinguished by an analyzer oriented perpendicular to the central plane of incidence. The zone of extinction in the full aperture, observable in the back focal plane of a microscope (b), is indicated in the inset (a) for this case. An effective aperture stop is chosen to select an illumination with a good extinction ratio. Image is adopted from Ref [Hub09].

incidence. The positions of polarizer and analyzer are defined with respect to this central plane. For all beams not lying in this plane the effective polarizer angles are different. If the

polarizer settings were optimized for the central illumination plane, they are no more optimized for other beams. This can be demonstrated by adjusting polarizer and analyzer for maximum extinction and looking at the diffraction plane (the so-called conoscopical image) of the microscope (by using a built-in Bertrand lens, or an auxiliary telescope replacing the eyepiece, or, less satisfactory, by simply looking into the tube after removing the eyepiece). The zone of maximum extinction is in general cross shaped in the full aperture (Fig.3.10a, inset). Polarization-dependent reflection and transmission effects on curved lens surfaces and other optical elements within the microscope add to the depolarization by the sample. This is particularly true for the strong objective lenses used at high magnification. All these depolarization effects could in principle be reduced by suitably tailored anti-reflection coatings on lenses and sample. No practical solution in this sense is available, however.

To obtain best contrast conditions, the illumination should be restricted to the extinction zone in the conoscopical image. For the polar effect, a central circular diaphragm is placed in the illuminating beam. For the longitudinal effect, a displaced slit aperture oriented parallel to the plane of incidence is preferable [Tre61], while, for the transverse effect, a displaced slit oriented perpendicular to the plane of incidence would be the best solution. The diaphragm should be effective uniformly for the whole observation field by placing its optical (not the actual) position into the back focal plane of the objective (Fig.3.11b). This is achieved by adjusting the lens indicated in this Fig and in Fig. 3.10(b) according to the properties of the respective objective. If a sheet reflector is used instead of a prism, the plane of incidence can be chosen freely by moving the image of the aperture diaphragm in the back focal plane of the objective. In this case the true transverse Kerr effect can be replaced by the longitudinal Kerr effect with a transverse plane of incidence.

In conclusion the standard Kerr technique of domain observation provide unique tool to study the magnetization state and analysis of the magnetic domains of the studied samples through non-contact (not destroy or damaged) during observation regardless of the shape and size of the sample. The process of observation does not influence the magnetization (if the heating effect of the illumination is suppressed; as another exception, there are certain photo-induced magnetic anisotropy changes in magnetic oxides). Dynamic processes can be observed at high speed by using high speed camera. The samples may be manipulated easily during observation. High or low temperature, mechanical stress or, most importantly, arbitrary magnetic fields may be applied. The same effects that are used for imaging may also

be used for the magnetic characterization of the material, measuring local hysteresis properties. These possibilities are naturally available in the scanning variant of Kerr microscopes. They can also be added to conventional Kerr microscopes by replacing the camera with a photoelectric detector or adding a micro-magnetometer to the microscope [MaC95].

Beside advantages there are few drawbacks of magneto-optical methods such as samples have to be prepared so that they are reasonably flat and smooth on a scale exceeding the chosen resolution. Some equipment is necessary, especially if low contrast conditions call for electronic enhancement. The resolution is limited to magnetic domains larger than about $0.15\mu\text{m}$, corresponding to an optical resolution of about $0.3\mu\text{m}$.

3.2.3.2 Domain observation

Figure 3.12(a) shows the general principle of the domain observation. Light from a source passed through a polarizer which transmits only plane polarized light, or naturally polarized light from a laser, is incident on the specimen. For simplicity the specimen is assumed to contain only two domains, magnetized antiparallel to each other as indicated by the arrows. During reflection the plane of polarization of beam 1 is rotated one way and that of beam 2 the other way, because they have encountered oppositely magnetized domains. The

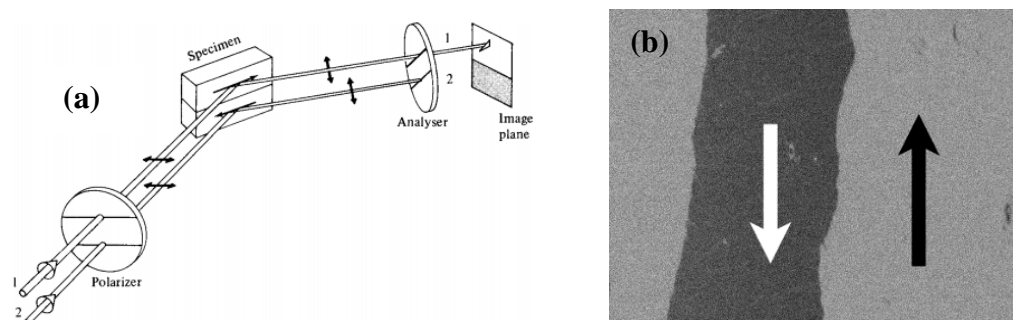


Figure 2.12: (a) Principle of domain observation by the Kerr effect, (b) Domains in 40nm $\text{Fe}_{60}\text{Al}_{40}$ thin films irradiated with Ne^+ ion energy of 30keV observed using Kerr effect.

light then passes through an analyzer and into a low-power microscope. The analyzer is now rotated until it is “crossed” with respect to reflected beam 2; this beam is therefore extinguished and the lower domain appears dark. However, the analyzer in this position is not crossed with respect to beam 1, because the plane of polarization of beam 1 has been rotated with respect to that of beam 2. Therefore beam 1 is not extinguished, and the upper domain appears light. Fig 3.12(b) shows domains in a thin film of 40nm of $\text{Fe}_{60}\text{Al}_{40}$ irradiated with

Ne⁺ ions with energy of 30keV revealed in this way; the light and dark bands are domains magnetized in opposite directions.

Because of the small angle of rotation of the plane of polarization, the contrast between adjoining domains tends to be low, so all the optical elements must be of high quality and well adjusted. However, the Kerr method is ideal for observation of domain walls in motion and has supplanted the Bitter method for such studies. It has no limitations with respect to specimen temperature beyond the usual ones of thermal insulation and protection against oxidation. It can be applied both to bulk specimens and thin films. However, a component of the magnetization vector must be parallel to the direction of propagation of the light, which means for most materials the light beam strikes the sample surface at a fairly small angle. This limits the area that can be observed, especially at high magnification. Note that the term “Kerr effect” is also applied to an *electro-optic* effect. If certain organic liquids are placed in a transparent container, called a Kerr cell, and subjected to an electric field, plane polarized light passing through the cell will be rotated by an amount depending on the applied voltage.

3.2.4. Study of magnetization reversal processes

Magnetic switching in thin film has obtained great technological importance because of numerous devices rely on the fact that magnetic system can be bistable. Switching from one state to other is achieved by a magnetic field. As soon as the field is applied, one state becomes metastable, and the system proceeds through large number of metastable states of decreasing energy until the ground state is reached. Temperature and applied field determine the probability to overcome the barriers separating metastable states, and thus system evolves with time even though field and temperature are kept constant. This relaxation phenomenon is called an after-effect or creep. The long term stability of the magnetic storage media is largely determined by this effect [Mos99]. Magnetization relaxation study was carried out for Fe₆₀Al₄₀ thin films. The ferromagnetism in the present case is related to the disorder (A2-phase) which is directly related to the collisions between the energetic ions and host atoms, thus creating inhomogeneous distribution of ferromagnetic (FM) regions in thin Fe₆₀Al₄₀ films. From a technological point of view such systems are promising candidates for their use in high density data storage applications. An understanding of the magnetization reversal process is necessary for exploring the potential of materials possessing disorder induced ferromagnetism for applications in data storage media. Magnetization reversal (MR) was

studied by imaging the change of the magnetic domain patterns in an applied reversal magnetic field (H_R), as a function of time (t). The scheme of the experimental procedure is shown in Fig. (3.13). Initially, the samples were magnetized by an applied magnetic field $-H_M$ parallel to the sample plane with field amplitude larger than its coercivity value. In the next step, at time $t = 0$ the reversal magnetic field H_R with opposite direction to $-H_M$ with $H_R < +H_c$ was applied inducing the magnetization reversal process. The values of the normalized magnetization (m) were calculated from the magnetic domain images for $t > 0$.

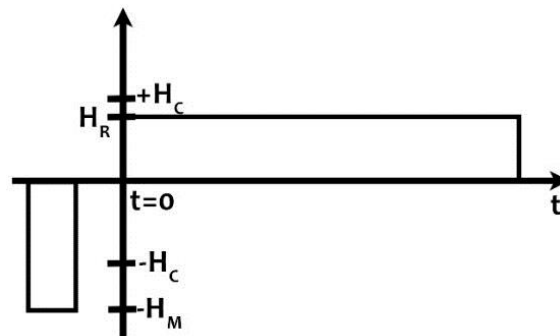


Figure 3.13: Schematic of in-plane applied magnetic field changes for magnetization reversal studies.

3.3. Dynamics measurements

3.3.1. Ferromagnetic Resonance (FMR)

The local environment of a magnetic moment is determined by the crystal fields, but spin-orbit couplings and hyperfine interactions with the nuclei also play an important role in controlling the electronic structure. These effects can be studied by using a variety of experimental techniques which involve magnetic resonance. The resonance arises when the energy levels of a quantized system of electronic or nuclear moments are Zeeman split by a uniform magnetic field and the system absorbs energy from an oscillating magnetic field at sharply defined frequencies corresponding to the transitions between the levels. In 1946, Griffiths observed that microwaves are strongly absorbed by ferromagnetic films at a frequency different from the Larmor frequency of the electron spin [Gri46] and later, [Kit47] theoretically explained this phenomenon as the ferromagnetic resonance in a magnetic material. Ferromagnetic resonance (FMR) technique was initially applied to ferromagnetic materials, all magnetic materials and unpaired electron systems. Basically, it is analogous to

the electron paramagnetic resonance (EPR). The EPR technique gives better results at unpaired electron systems. The FMR technique depends on the geometry of the sample at hand. The demagnetization field is observed where the sample geometry is active. The resonance area of the sample depends on the properties of material. The FMR technique is advantageous because it does not cause damage to materials. Also, it allows a three dimensional analysis of samples. The FMR occurs at high field values while EPR occurs at low magnetic field values.

The sample geometry, relative orientation of the equilibrium magnetization M , the applied dc magnetic field H and experimental coordinate systems are shown in Fig. 3.14.

The magnetization dynamics of a uniform precession motion is described by the Landau-Lifshitz-Gilbert equation. The magnetic moments are assumed to precess coherently with the same frequency and phase. The frequency of a uniform precession mode is known as ferromagnetic resonance (FMR) frequency ω_{FMR} . The FMR mode describes the spin waves with infinite wavelength, i.e., their wave-vector $|k_{SW}| = 0$. Therefore, all magnetic moment are parallel to each other and precess in phase hence exchange energy to the total SW system equals to zero. The FMR frequency is

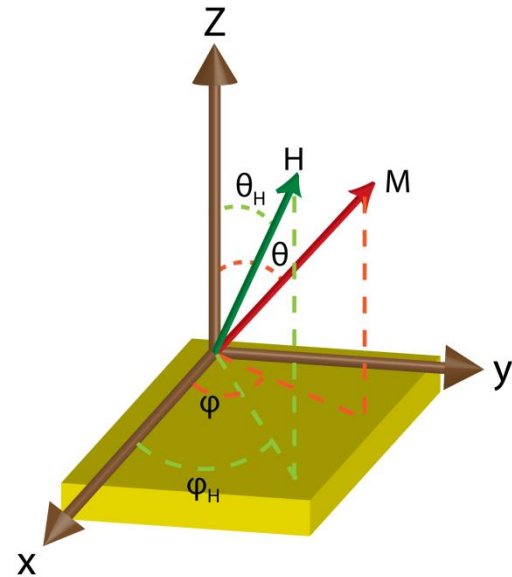


Figure 3.14: Sample geometries and relative orientations of equilibrium magnetization M and the dc component of external magnetic field, H for thin films.

calculated through the Landau Lifshitz equation (2.41) is solved for small dynamic magnetic fields. In this approach, the magnetization is assumed to have a static as well as a dynamic component written as $M(t) = M_o + m(t)$. The Dynamic magnetization m is assumed to have a harmonic time dependence as $m = m \exp(i\omega t)$. The dynamic magnetization is considered to be a response of the effective magnetic field using Eqs. (2.22), (2.42), given as:

$$B(t) = B_o - \mu_o \tilde{N} m(t). \quad (3.3)$$

By assuming the dynamic magnetization to be very small in comparison with the static magnetization ($m(t) \ll M_o$), the LLG equation (2.43) can be linearized. For an ellipsoidal with demagnetizing tensor N , the ferromagnetic resonance frequency [Kit48] is express as:

$$\omega_{FMR} = \gamma \sqrt{[B_{eff} + \mu_o M_S(N_{yy} - N_{zz})][B_{eff} + \mu_o M_S(N_{xx} - N_{zz})]}, \quad (3.4)$$

and known the *Kittle* equation or formula. The effective magnetic field $B_{eff} = \mu_o(H_{ext} + H_{ani})$, and external magnetic field $B_{ext} = \mu_o H_{ext}$ act along z -axis. For an infinitely long thin film, magnetized in the xy -plane ($N_{xx} = 1, N_{yy} = N_{zz} = 0$), the Kittle formula simplifies to:

$$\omega_{FMR} = \gamma \sqrt{B_{eff}(B_{eff} + \mu_o M_S)} \quad (3.5)$$

3.3.1.1. Experimental arrangement of FMR

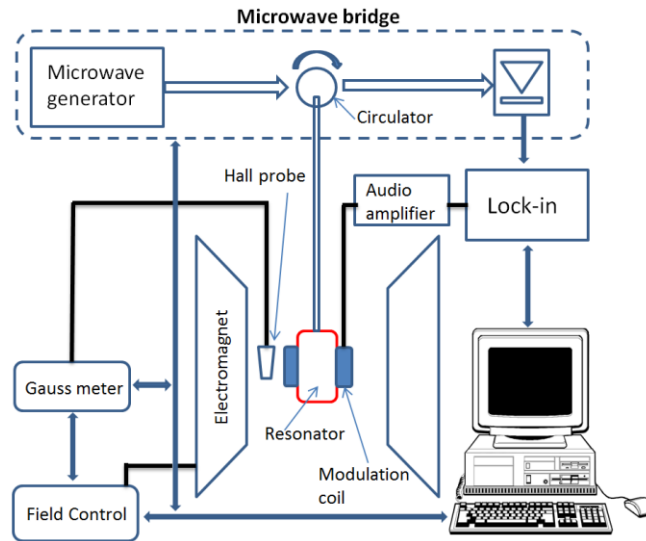


Figure 3.15: Basic configuration of FMR spectrometer. The microwave bridge mainly consists of microwave generator, circulator, and detector. The image is adopted from Ref. [Lo13].

When a ferromagnetic material is placed in electromagnetic field (DC or Quasi DC) whose frequency equals the precessional frequency of the ferromagnetic system, resonant absorption occurs. This phenomenon is called ferromagnetic resonance. Generally speaking the FMR spectrometer should consist of at least an electromagnetic (EM) wave excitation source, detector, and transmission line which bridges sample and EM source. The precession frequency lies at microwave range from 0.1 to about 100 GHz (L-Band (1-2GHz), S-Band (2-4GHz), C-Band (4-8GHz), X-Band (8-12GHz), Ku-Band (12-18GHz), K-Band (18-27 GHz), Ka-Band (27-40), V-Band (40-75 GHz), W-band (75-110 GHz)). A schematic of the standard

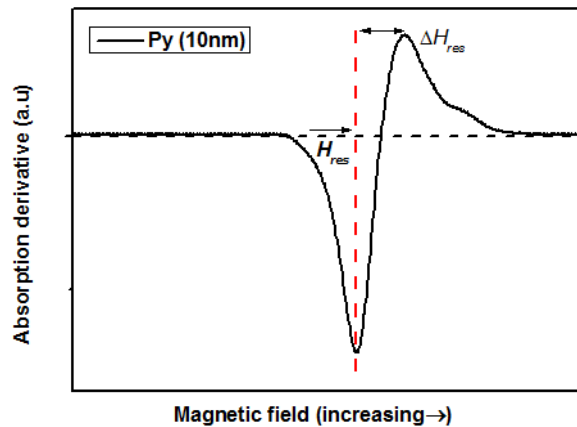


Figure 3.16: Exemplary FMR spectrum from uniform Py thinfilm with thickness of 10nm. The resonance field and FMR linewidth are also shown.

FMR experimental setup is shown in Fig. (3.15). FMR spectrometer contains a resonator and an electromagnet which produces magnetic field to vary the sample's magnetization during the measurement. Sample is mounted inside the cavity which absorbs energy from the microwave source. During sweeping of magnetic field, the change in reflectance or transmittance of the microwave is being monitored through detector. Usually FMR spectrometer works at standard frequency (in our case it is X-Band (9.4 GHz)). The microwave is generated through Klystron, which goes to a metallic cavity via waveguide. Signal reflected towards the detector from the cavity follows the same waveguide where circulator is employed to guide microwave to-wards the detector and not return back to the generator. After the FMR condition is satisfied through tuning of the applied magnetic field, the ferromagnetic-resonance absorption in the spin system changes the dielectric function and the permeability in the cavity and thus the resonance characteristics, and will be “resonantly” enhanced. Figure 3.16 illustrates a standard FMR signal in the form of the derivative of the absorption. The most important parameter from FMR measurement is the resonance field (H_{res}). Magnetic anisotropy is investigated by measuring how the resonance field values changes with the change in direction of the applied magnetic field. The FMR linewidth ΔH_{res} also contains useful information as it provides a measure of magnetic homogeneity of the studied system [Far98].

3.3.2. Brillouin Light scattering (BLS) spectroscopy

In FMR experiment one has to restricted to the spin excitations with zero wave-vector which are uniform across the sample and do not exhibits dipolar coupling in layered structures. In addition, in a FMR experiment one measures the average magnetic properties of a millimetric-sized sample and is generally limited to a single frequency. These limitations has been overcome by employing Brillouin light scattering (BLS) technique which relies upon the inelastic scattering of photons. BLS is an optical spectroscopic method for the investigation of excitations in magnetic structures, such as thin films [Tac14, Yos04, and Coc91], multilayers [Kra91 and Hil93] and magnetic nanoelements [Car00, Car14], and single crystals [Zuk92] with frequencies in the GHz regime. BLS has number of advantages over microwave spectroscopy. These are: (i) the potential to investigate spin waves with different absolute

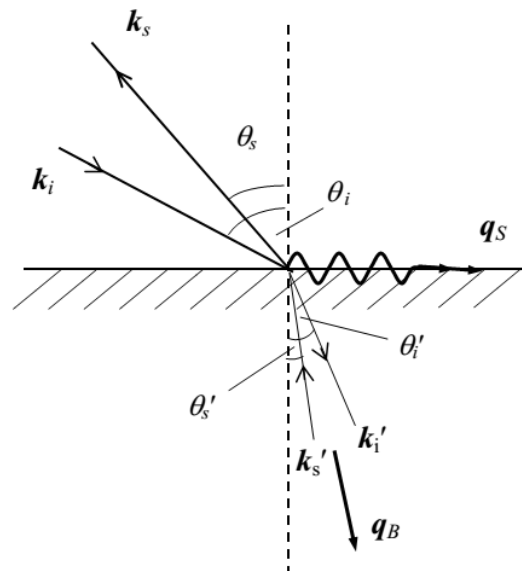


Figure 3.17: Schematic of scattering geometry: the incident and scattered light wave-vectors k_i and k_s ; the surface and bulk magnon (phonon) wave-vectors q_s and q_B . θ_i and θ_s are the angles between the out-going surface normal and the respective incident and scattered light. (The plane which contains the wave-vector of the scattered light and the surface normal of the sample is defined as the scattering plane.) Figure is adopted from Ref. [Hai06].

values and orientations of their wave-vectors; (ii) a wide dynamic range. i.e the possibility to detect both low amplitude thermal spin waves and high amplitude spin waves, excited by an external microwave source.; (iii) high spatial resolution defined by the size of the laser beam focus, which is 30-50 μm in diameter (a non-destructive and non-contact technique) [Car99]., i.e BLS provides an unique opportunity to investigate two-dimensional confinement effects [Dem01]. In BLS measurements, a beam of highly monochromatic light is focused on the

sample surface under investigation. The scattered light within a solid angle is frequency analyzed using a multi-pass Fabry-Perot (FP) interferometer. From BLS measurements of the spin wave frequency as a function of the direction and magnitude of the external magnetic field, magnetic properties such as anisotropy constant, exchange constant, gyromagnetic ratio and saturation magnetization, can be obtained.

During BLS experiment, a laser beam of fixed angular frequency and wave-vector is incident on the surface of a sample. Fig (3.17) shows the scattering geometry with an incident angle of θ_i to the surface normal. Most of the light is specularly reflected or absorbed. However, as a result of thermal excitation (magnon or phonon), a small fraction of the light is

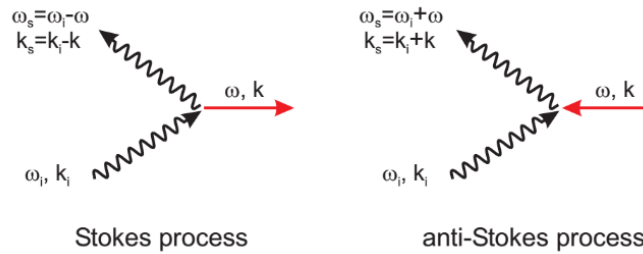


Figure 3.18: Schematic showing of photon-magnon scattering processes. A magnon can be created (Stokes process) or annihilated (anti-Stokes process) resulting in a gain or loss in energy and momentum of the scattered photon respectively. ω_i and k_i denote frequency and wave vector of the incoming photon, ω_s and k_s describe the scattered photon and ω and k are assigned to the magnon.

inelastically scattered with a frequency shift depending on the nature of the scattering process see (Fig. 3.18). The spectrum of the light inelastically scattered at an angle θ_s contains information about surface or bulk (or both) magnons (or phonons). In the usual implementation of BLS, the scattered light is collected in the direction 180° from the incident light and thus is $\theta_i = \theta_s$, an arrangement known as the 180° -backscattering geometry which is the mainly used in the present study, a schematic for the experimental setup is shown in Fig. 3.20.

From the quantum mechanics point of view, such an inelastic scattering can be described as: Photons can interact with magnons, i.e. the elementary quanta of spin waves, via inelastic photon scattering which is known under the name of Brillouin light scattering. Generally, two different scattering processes are distinguished, in which a magnon is created (Stokes process) or annihilated (anti-Stokes process), resulting in an energy shift of the

scattered photon, Fig. (3.15). Both photon-magnon scattering processes satisfy the laws of energy and momentum conservation:

$$\hbar\omega_i = \hbar\omega_s \pm \hbar\omega \quad (3.6)$$

$$\hbar k_i = \hbar k_s \pm \hbar k \quad (3.7)$$

In these expressions, $\omega_{i,s}$ and $k_{i,s}$ denote the frequency and wave vector of the incoming and scattered photon, respectively. The parameters describing the magnon are without any index. For light scattering from thin films the perpendicular component of the wave is not conserved anymore due to the break of translational symmetry. In this case, Eq. (3.7) is only valid for K_{\parallel} which is the wave vector component parallel to the film plane.

The presence of SW modulates the interaction between photons and the medium as a result the frequency of the reflected light from the medium gets shifted by the frequency of SW, given by the Doppler shift [Dem01, Gio01]:

$$\omega_s = \omega_i \pm K \cdot v_{sw} \quad (3.8)$$

where v indicates the phase velocity of the SW in the medium. The mathematical signs depends on the direction of the propagating Bragg grating with respect to the wave-vector of the incident light. Considering the Bragg condition $K = K_i - K_s$, the energy and momentum conservation conditions in Eq. (3.6) and Eq. (3.7) can be obtained. In order to determine the wave-vector of SWs, it is crucial to notice that the translation invariance is broken along the normal of thin films, so the conservation of linear momentum is not valid along the film normal. Only the in-plane components of wave vectors are conserved. Therefore, the wave vectors of light should be replaced by their projection along the film plane such that

$$K_s^{\parallel} = K_i^{\parallel} \pm K \quad (3.9)$$

So by changing the projection of the light, i.e the angle of incidence angle θ of light with respect to the film plane (Fig. 3.19), wave-vector resolved measurements can be performed which was the case in the present study.

$$K_{\parallel} = \left(4\pi/\lambda_{\text{laser}}\right) \sin\theta. \quad (3.10)$$

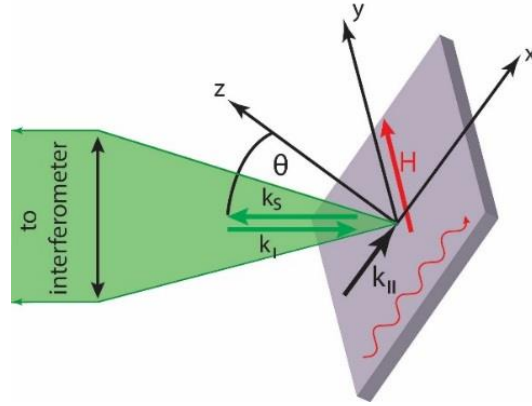


Figure 3.19: Scattering geometry of the laser from the sample surface in BLS setup.

3.3.2.1. Experimental arrangement

The BLS apparatus is employed to study the small shift in frequency lying in the gigahertz regime. The apparatus consists of many optical components including a solid state laser with a wavelength (λ_{laser}) of 532 nm and a tandem Fabry-Perot interferometer. The schematic of the experimental setup for BLS is shown in Fig. (3.20). Inelastically scattered light is sent through a crossed analyzer in order to suppress surface phonons signal. A static magnetic field is applied in the film-plane perpendicular to the transferred wave vector scattering plane, i.e. in the Damon-Eshbach (DE) geometry. The measurements are performed for various magnetic field values and at different angles of incidence of the probing light beam, *i.e.* the angle between the direction of the incident laser beam and the film normal θ , as shown in Fig. 3.19. The amplitude of the spin-wave transferred in-plane wave vector is related to the angle of incidence θ by the relation $q_{\parallel} = (4\pi/\lambda_{\text{laser}})\sin\theta$. By changing θ in the range of 10-80 degrees it is possible to change of q_{\parallel} from the range of $(0.81-1.8) \times 10^5 \text{ cm}^{-1}$.

One can see the path of the light coming out from the laser and finally going to the tandem Fabry-Perot (TFP) interferometer which is used to measure the shift in the frequency (spin wave frequencies). The TFP will be described in the following subsection.

The laser with power 200 mW is used to thermally excite spin waves in the present study. The laser is single mode and is linearly polarized perpendicular to the plane of the optical table. The light is targeted to the sample which is lying between the electromagnets. The scattered light is collected and directed towards the TFP. In order to study the spin waves, a crossed polarizer is inserted in the path of the scattered light, set such that it passes light perpendicular

to the incident laser polarization to suppress the signal from the phonons. Since the scattered light from a BLS measurement contains mostly elastically scattered light and light of the same polarization as the laser, the polarizer blocks out light of unaffected polarization. Photons that have scattered from magnons have a component normal to the original polarization that is transmitted through the polarizer.

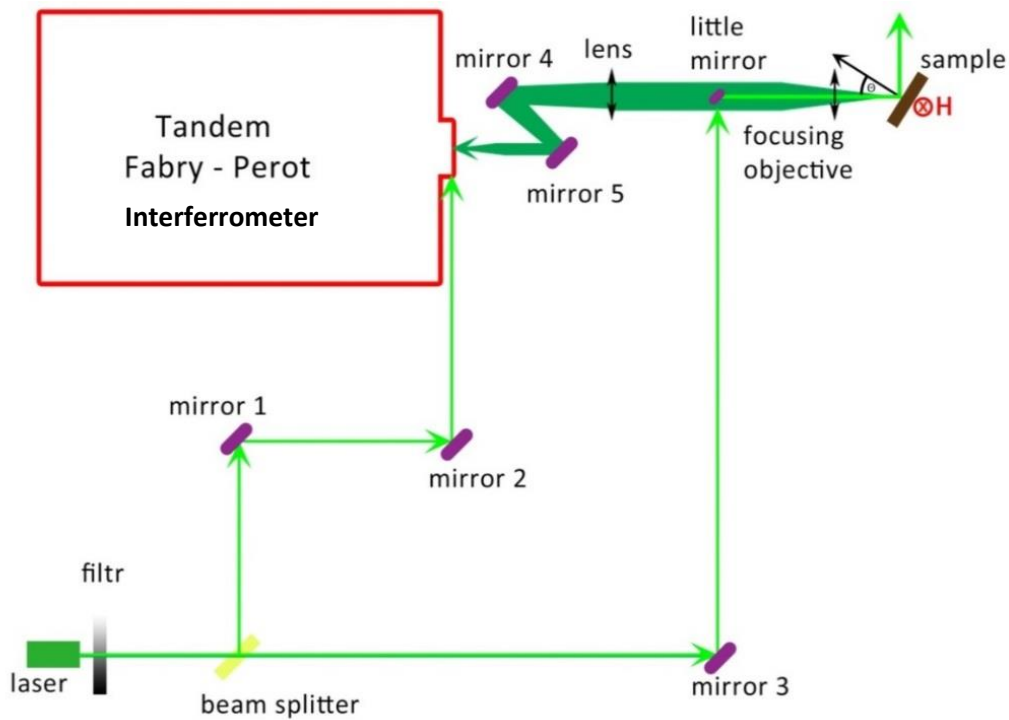


Figure 3.20: Experimental setup for BLS in backscattering geometry.

3.3.2.2. Tandem Fabry-Pérot (TFP) interferometer

Tandem Fabry-Perot interferometer (TFP) is employed where high resolution

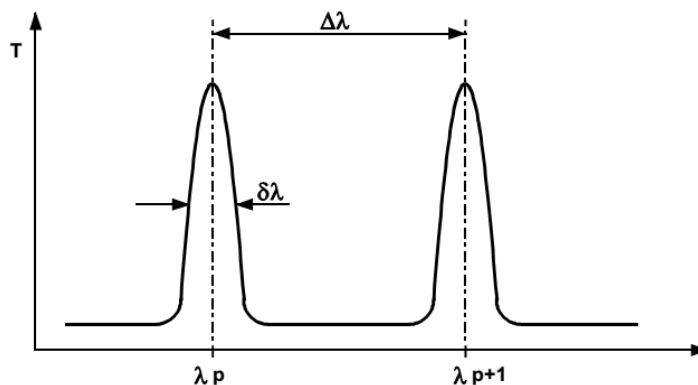


Figure 3.21: Illustration of the transmission versus wavelength of FP interferometer. Figure is adopted from Ref. [San10].

spectroscopy resolution of MHz to GHz is required. In TFP interferometer [San, J. R. Sandercock, Tandem Fabry-Perot Interferometer TFP-1, Operator Manual. JRS Scientific Instruments] two partially reflecting plane mirrors (the surfaces of the mirrors facing each other are coated with silver and typically have around a 95 percent reflectivity) are mounted accurately parallel to one another, with an optical spacing L_{mir} between them. The interferometer has the ability to scan through different frequencies because the spacing between the mirrors can be adjusted.

The light after entering into the interferometer goes through multiple reflections and will interfere constructively or destructively depending on the phase difference between the incident light and the reflected light. The phase difference is described as [Hec02]:

$$\delta = \left(\frac{2\pi}{\lambda_{laser}} \right) 2L_{mir}, \quad (3.11)$$

where λ_{laser} is the wavelength of the incident light, which remains constant for the reflected light. For constructive interference, the incident light the reflected light will be in phase ($\delta = 2\pi n$). This corresponds to mirror spacing of $L_{mir} = n\lambda_{laser}/2$. Here $n = 0, 1, 2, 3, \dots$

Through scanning the distance, light of a particular frequency will constructively interfere and be transmitted. The BLS will observe shift in frequencies caused by spin waves.

The operational principle of the TFP is described in Fig. 3.22. The first interferometer FP1 is set to lie in the direction of the translation stage movement. One mirror sits on the translation

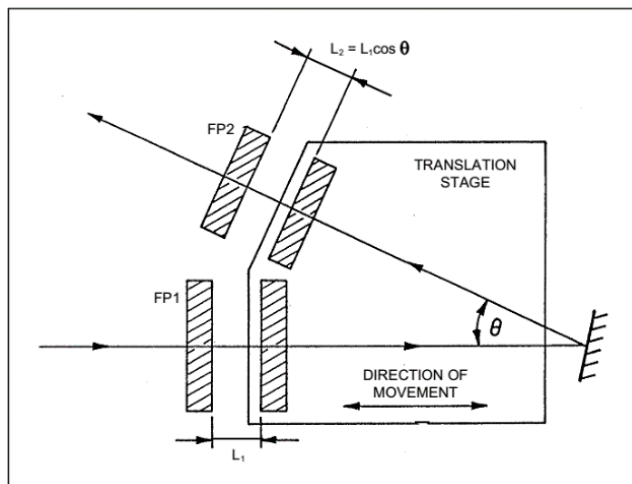


Figure 3.22: Transmission spectra for tandem Fabry-Perot interferometer. Figure is adopted from Ref. [San10].

stage, the other on a separate angular orientation device. The second interferometer FP2 lies with its axis at an angle θ to the scan direction. One mirror is mounted on the translation stage in close proximity to the mirror of FP1, the second mirror on an angular orientation device. A synchronization condition:

$$\delta L_1 / \delta L_2 = L_1 / L_2 \quad (3.12)$$

is satisfied when a movement of FP1 towards right side sets the spacing to L_1 (scan of δL_1 of the translation stage) produces a change of spacing δL_1 in FP1 and $\delta L_1 \cos \theta$ in FP2.

The length of the scan is limited by the shear displacement of the mirrors of FP2 for which scan more than $D/\sin \theta$ (mirror diameter D) would no longer overlap. A scan of several cms is easily possible for normal mirror diameters (3-5 cms). Figure 3.23 shows the optical setup for the (3+3)-pass TFP interferometer. The scattered light enters the system through the adjustable pinhole P1.

The aperture A1 defines the cone of the light which is accepted. Mirror M1 reflects the light towards the lens L1 where it is collimated and directed via mirror M2 to FP1. After passing through aperture 1 of the mask A2 and is directed via mirror M3 to FP2.

After transmission through FP2 the light strikes the 90° prism PR1 where it is reflected

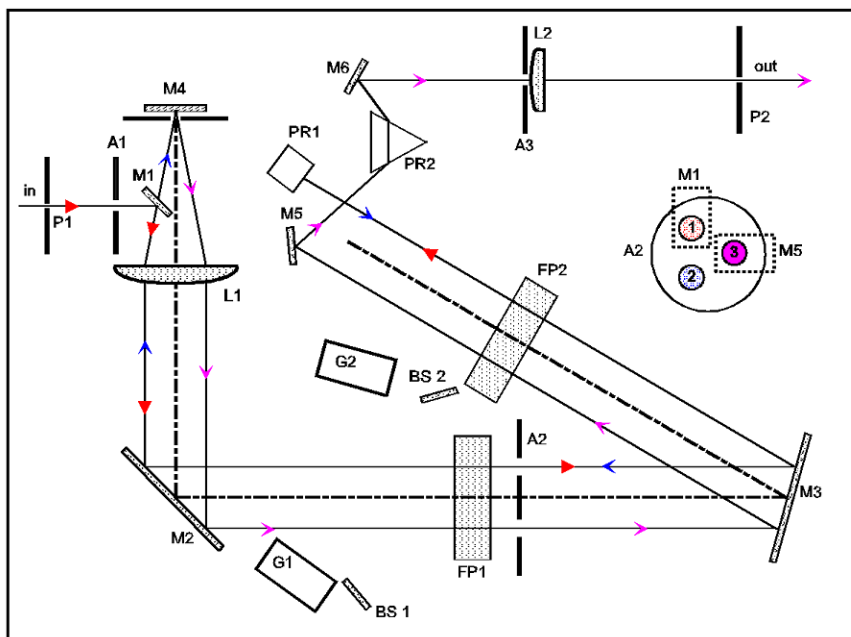


Figure 3.23: Optical layout for (3+3)-pass tandem operation. Figure is adopted from Ref. [San10].

downwards and returned parallel to itself towards FP2. It continues through the aperture 2 of A2 to FP1. After transmission through FP1 it passes through lens L1, underneath mirror M1, and is focused onto mirror M4. This mirror returns the light through lens L1 where it is again collimated and directed through FP1.

The combination of lens L1 and mirror M4 lying at its focus is known as a cats-eye, and is optically equivalent to a corner-cube but has the advantage that it also acts as a spatial filter which filters out unwanted beams such as the beams reflected from the rear surfaces of the interferometer mirrors. After the final pass through the interferometers, through the aperture 3 of A2, the light strikes the mirror M5 where it is directed to the prism PR2. This prism, in combination with the lens L2 and the output pinhole P2, forms a band-pass filter with a width determined by the size of the pinhole. The mirror M6 sends the light to the output pinhole and will have to be adjusted whenever the laser wavelength is changed. The glass block G1 shifts the light sideways so that it strikes FP1 in the center. The light reflected from FP1 and FP2 is shifted via the glass block G2 into the output path so that it passes through the output pinhole and on to the photomultiplier.

4. Results and Discussions

4.1. Fe₆₀Al₄₀

4.1. Fe₆₀Al₄₀

It is known that ferromagnetism in Fe₆₀Al₄₀ alloys by means of ion irradiation has depth distribution which requires an understanding of the statics and dynamics of magnetization for exploring the magnetization reversal mechanisms and spin wave excitations as this material can be potential candidate for fabrication of MCs and data storage media. Disorder is directly related to the collisions between the energetic ions and host atoms, thus creating inhomogeneous distribution of ferromagnetic (FM) regions in thin Fe₆₀Al₄₀ films. Source of depth varying magnetization in Fe₆₀Al₄₀ 40 nm thin films sets the plate form for studying dynamics of magnetization which has been systematically studied by vector network analyzer ferromagnetic resonance (VNA-FMR) and Brillouin light scattering (BLS) spectroscopy along with analytical calculations. Depth of disorder produced in the films is directly related to the ion energy so that the effective thickness of the ferromagnetic phase too. In general, the A2/B2 phase boundary is gradually pushed deeper into the film with increase in ion energy and finally expelled when the film is fully penetrated by the ions. The ability to adjust the position of the A2/B2 phase boundary helps to investigate the possible pinning effects at this interface. Pinning of spin-wave modes was considered in the analytical calculations to interpret the experimental results.

4.1.1. Sample fabrication

4.1.1.1. Uniformly irradiated thin films

Oxidized Si(100) substrate (150nm) was used as buffer layer. Substrates were oxidized in tube furnace for 136 minutes at 1323 K while the flow of oxygen was kept constant at 3L/min. Polycrystalline films of the desired composition (Fe₆₀Al₄₀) and thickness of 40nm were deposited by magnetron sputtering from an Fe-Al target (Chempur) of nearly same composition. Ar-based sputtering was carried out at room temperature with base pressure of 1.8×10^{-3} mbar. The films were further annealed at 773K for 60 minutes, under pressure of 1×10^{-5} mbar in a vacuum annealing furnace (Xerion). The buffer layer was necessary to protect the film from silicide formation during annealing process. In order to achieve disorder in thin films, they were irradiated with Ne⁺-ions (to avoid chemical reaction with the host atoms, and sufficient mass to produce dense collision cascade) at various energies between 2-30 keV with a fixed fluence of 6×10^{14} ions cm⁻². The schematic of the sample fabrication processes are shown in Fig. 4.1.

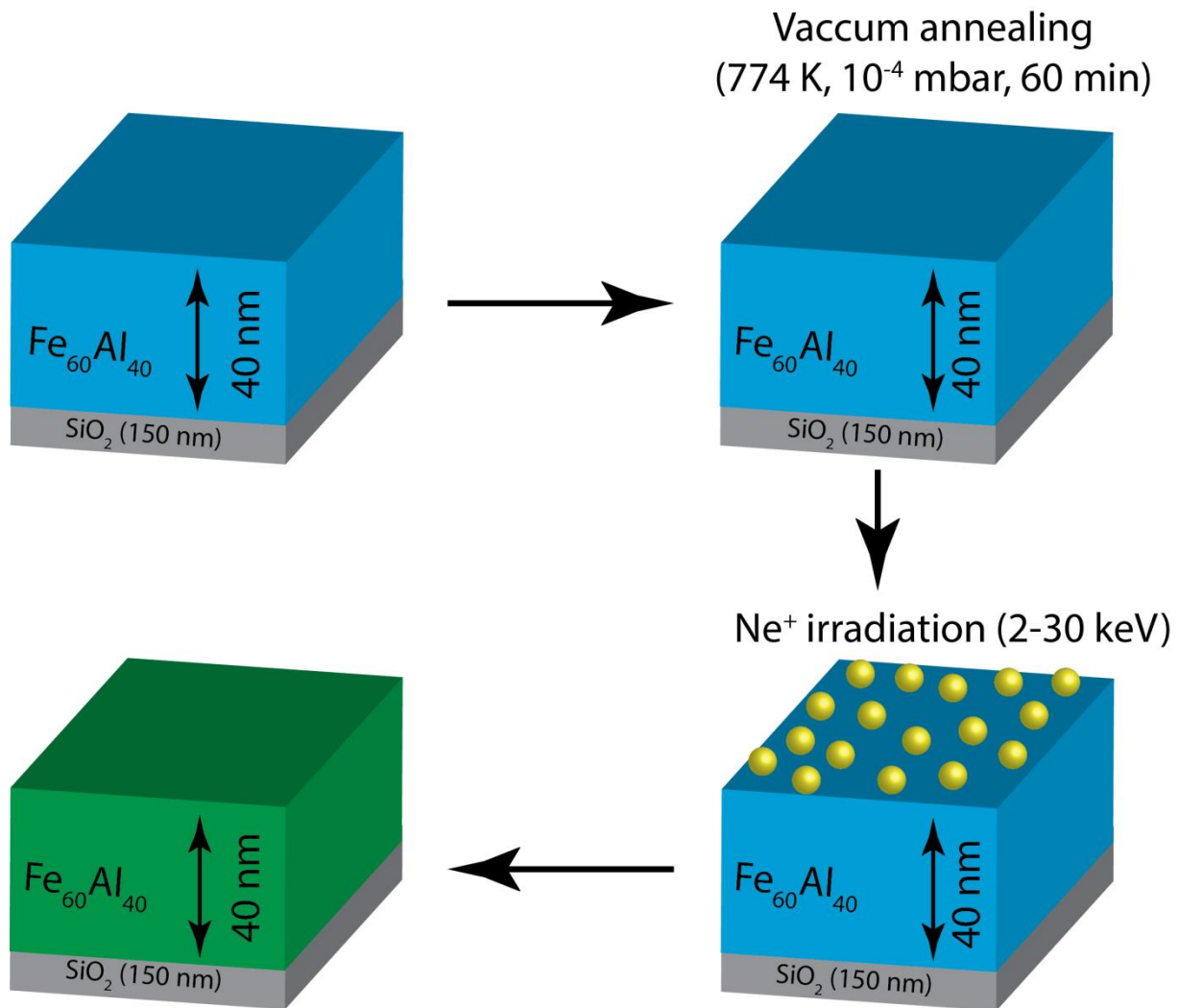


Figure 4.1: Sample preparation scheme.

Ions irradiation was carried out at Rossendorf (Germany). A 50 kV low energy ion-implanter 1050 (Danfysik A/S, Tastrup, Denmark) was used to bombard the Ne^+ -ions onto the $\text{Fe}_{60}\text{Al}_{40}$ thin films at base pressure of 5×10^6 mbar. The beam spot was approximately 1.5 cm in diameter and rastered over the sample with rate of 1 kHz. Fluence of 6×10^{14} ions cm^{-2} was deposited in 3 minutes by using a current of $0.65 \mu\text{A cm}^{-2}$. The disorder gradient was controlled by introducing shutter *in-situ* and moving it over the sample at $100 \mu\text{m}$ per step. At each step fluence of 1×10^{13} ions cm^{-2} was irradiated in 30 sec at $0.2 \mu\text{A cm}^{-2}$. Through this procedure the fluence was gradually varied from 0 to 6×10^{14} ions cm^{-2} , i.e over a range of 6 mm (size of the sample).

The structure of the samples was characterized by employing Empyrean (Panalytical) X-ray diffractometer (XRD). The scans were measured for a 2θ range of 20 - 120° . The presence of

Fe-rich phases that may contribute to the magnetic signal was not detected within the detection limit of the instrument, however a peak at 41.4° can be seen which does not corresponds to either A2 or B2 phase of $\text{Fe}_{60}\text{Al}_{40}$ phase [Bal14].

Detailed local analysis of the microstructure was carried out through transmission electron microscopy (TEM). TEM cross-sectional analysis of the samples suggests that actual thickness of the samples are around 40nm covered with a 4nm thick continuous oxide layer. Possible intermixing with the SiO_2 buffer layer due to annealing and irradiation is negligible confirmed by the well-defined substrate-film interface region. Moreover, the films surface was found to be smooth, pointing to negligible sputtering by the Ne^+ -ions. More details about the sample characterization can be found in Ref. [Bal14].

The B2 phase possesses a low saturation magnetization (M_s) of $\sim 20 \text{ kA m}^{-1}$. After irradiation the change in saturation magnetization, 480 and 780 kA m^{-1} for 10 and 30keV respectively was observed [Bal14]. The estimation of the depth profile is shown in Fig. 4.2(a) .

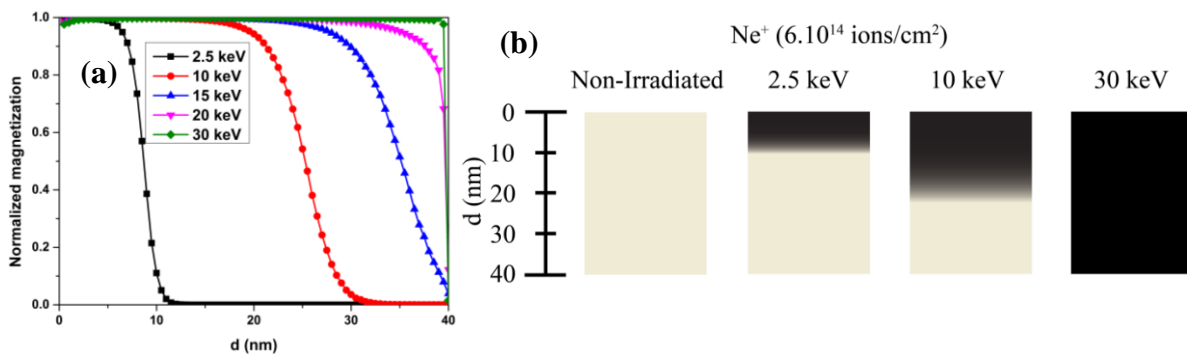


Figure 4.2: (a) Depth profile of the normalized magnetization for irradiation of the $\text{Fe}_{60}\text{Al}_{40}$ sample by Ne^+ ion having energies, 2.5 keV, 10 keV, 15 keV, 20keV and 30 keV, (b) Schematic shows creation of ferromagnetic layer with ion irradiation of different energies

4.1.1.2. Fabrication of 1D stripes

Magnetic patterning was performed on a $10 \mu\text{m}$ wide and $400 \mu\text{m}$ long wire of chemically ordered $\text{Fe}_{60}\text{Al}_{40}$ (Fig. 4.3). The wire was covered with a 150 nm thick resist layer and patterned using e-beam lithography. TRIM simulation showed that the 150 nm thick resist layer is sufficient to block impinging 10 keV Ne^+ -ions. Subsequent lithography was used to fabricate stripe like openings of 0.5 and $2 \mu\text{m}$ widths (Fig. 4.4). As shown in the Fig. 4.5 the stripe-openings were separated by $\sim 40 \text{ nm}$ wide (and 150 nm high) resist walls, thereby stopping the impinging Ne^+ ions reaching the areas directly underneath the resist.

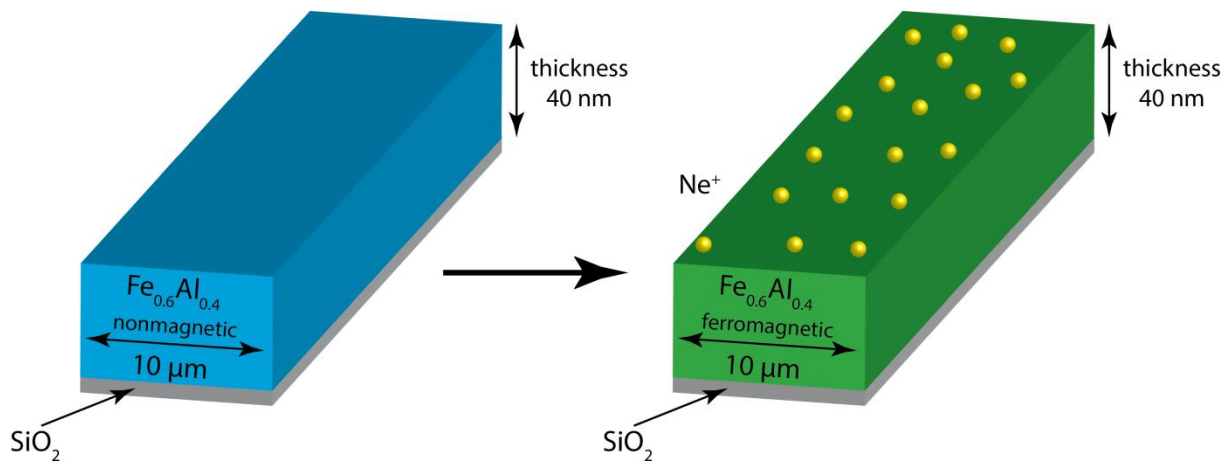


Figure 4.3: Fabrication scheme layout for the uniformly irradiated 1D stripe.

These areas can be expected to retain chemical order after exposure to Ne^+ , however, only if the lateral scattering of ions is restricted. The wire covered by the shadow-mask was exposed to 10 keV Ne^+ ions at a fluence of $6 \times 10^{14} \text{ ion cm}^{-2}$. Figure 4.6 shows the magnetic contrast image, obtained using Kerr microscopy on the sample prior to application of saturating magnetic fields. Striped regions are clearly observed possessing random magnetic orientations.

Patterning geometry: W_A ($2\mu\text{m}$)/ W (40nm spacer)/ W_B ($0.5\mu\text{m}$)/40 nm spacer (W)/.....

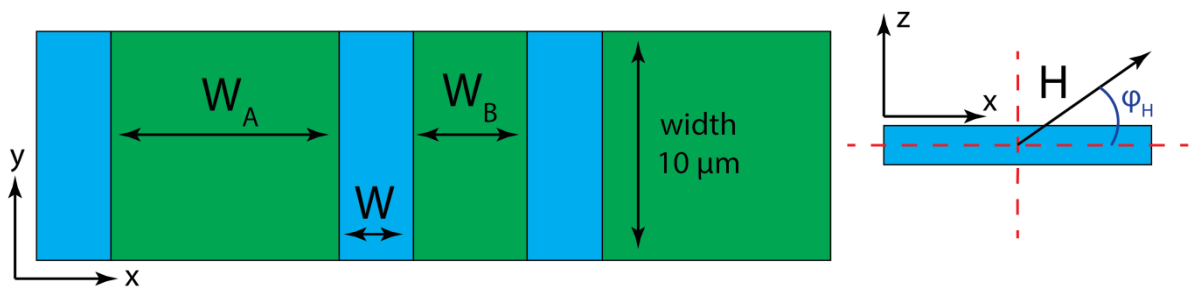


Figure 4.4: structural parameters for fabrication of reprogrammable 1D sample while the direction of the applied field is also shown on the right side.

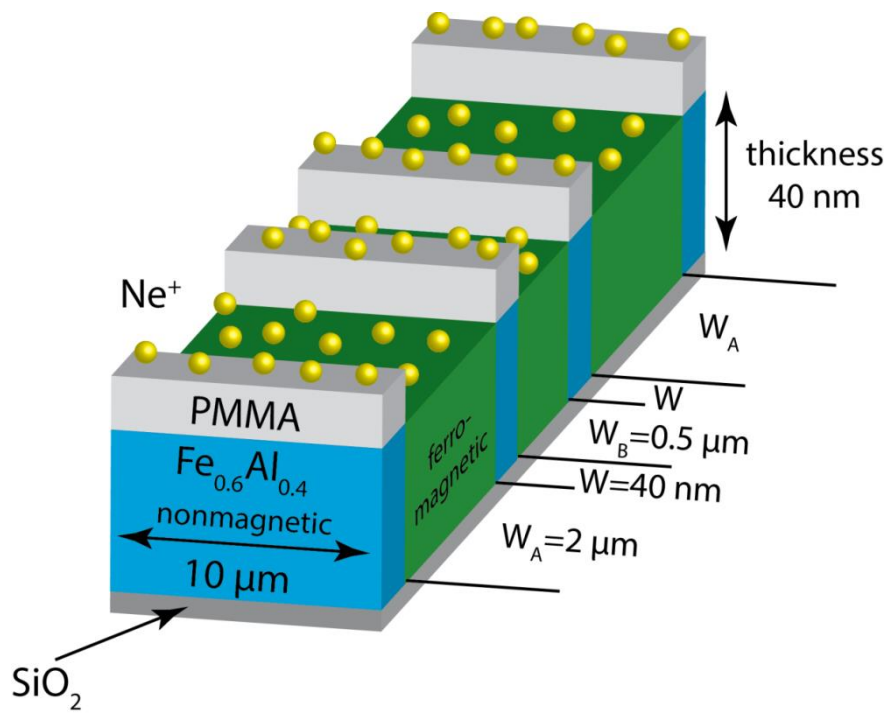


Figure 4.5: structural parameters for fabrication of reprogrammable 1D sample.

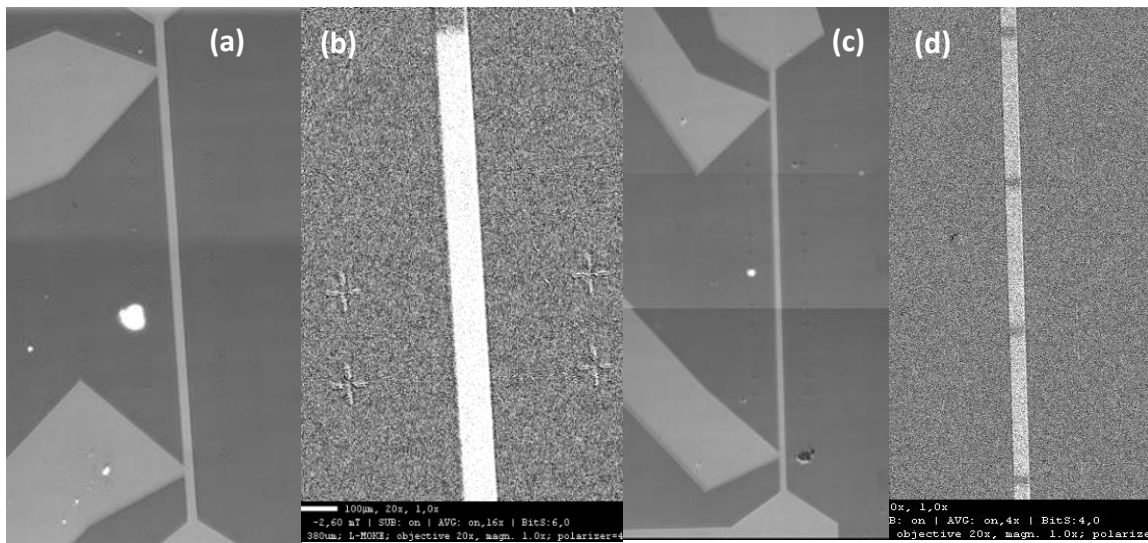


Figure 4.6: a) Optical image of uniformly irradiated 1D stripe. (b) Remanent image of uniformly irradiated 1D stripe. (c) Optical image of the reprogrammable 1D stripe. (d) remanent image of the reprogrammable 1D stripe. Different contrasts in the optical images (a and c) are due to the combination of different images to make one image.

4.1.2. Statics measurements

4.1.3. Uniform films

The magnetic properties of the samples are characterized by magneto-optical Kerr effect (MOKE) measurements in polar (PMOKE) and longitudinal (LMOKE) configuration at room temperature. The magnetic field perpendicular (H_{\perp}) to the sample plane or in-plane (H_{\parallel}) was applied in PMOKE and LMOKE configuration respectively. In the PMOKE setup the measurements were carried out using a diode laser light source (640-nm wavelength) emitting a beam of about 300 μ m in diameter. Magnetic domain images were observed as a function of time using LMOKE with a specially modified wide-field optical polarization microscope equipped with a CCD camera. The normalized magnetization m (defined as $(S_w - S_b)/(S_w + S_b)$) (where S_w and S_b are white and black domain areas, respectively) was calculated from the magnetic domain images for quantitative determination of the magnetization state.

4.1.3.1. Magnetization state

Figure 4.7 shows the magnetization curves measured for samples irradiated with 0, 2.5, 5, 10 and 30keV in PMOKE configuration. These curves show characteristics of hard axis with no hysteresis and can be characterized by parameter, saturation field (H_{sat}). The analysis of the magnetization curves from PMOKE (Fig. 4.7) and LMOKE (Fig. 4.9) clearly indicates an in-plane magnetization state (easy plane magnetic anisotropy). For applied field H_{\perp} , the magnetization rotates towards the normal of the sample plane. This perpendicular state is

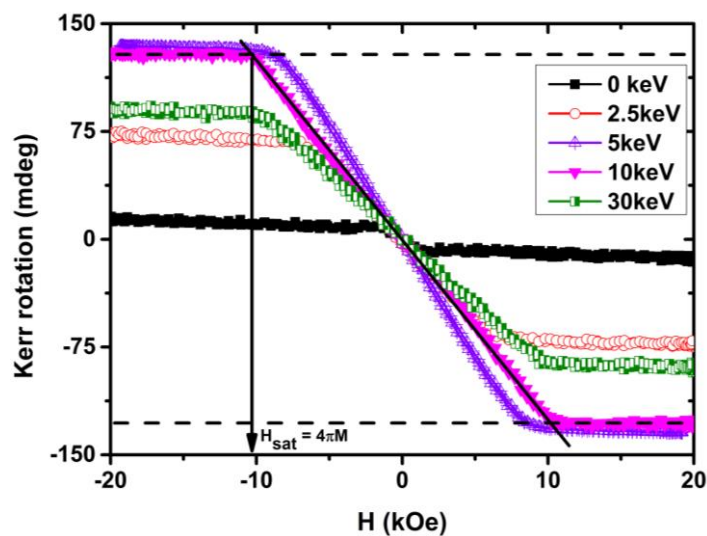


Figure 4.7: Magnetic hysteresis (PMOKE) of samples irradiated with ion energy of 0, 2.5, 5, 10 and 30keV.

achieved at the applied field of H_{sat} which corresponds to the effective magnetization $4\pi M_{\text{eff}}$. From the analysis of the PMOKE magnetization curves we can plot the effective magnetization Fig. 4.8 (a) as a function of ion energy. The effective magnetization ($4\pi M_{\text{eff}}$) increases with the increasing ion energies and saturates for the energies larger than 5keV. The saturation around 5keV energy can be also related to with the penetration depth of the laser light as the thickness larger than the light penetration depth ($\sim 20\text{nm}$ in the case of Fe) can be treated as bulk. This observation is also consistent with the VSM results where increase in the saturation magnetization upto 5keV is related to the increase in the disorder in the thin films [Bal14]. Fig. 4.8 (b) shows the dependence of estimated values of uniaxial anisotropy (K_u), and effective thickness (d_{eff}) on ion energy. The change in anisotropy could be related with the creation of the phase boundary (A2/B2).

At low energy the effective thickness is smaller which added additional anisotropy around the boundary between A2 and B2. The maximum anisotropy can be found around with effective thickness $\sim 21\text{nm}$ (10keV) which is almost half the film thickness.

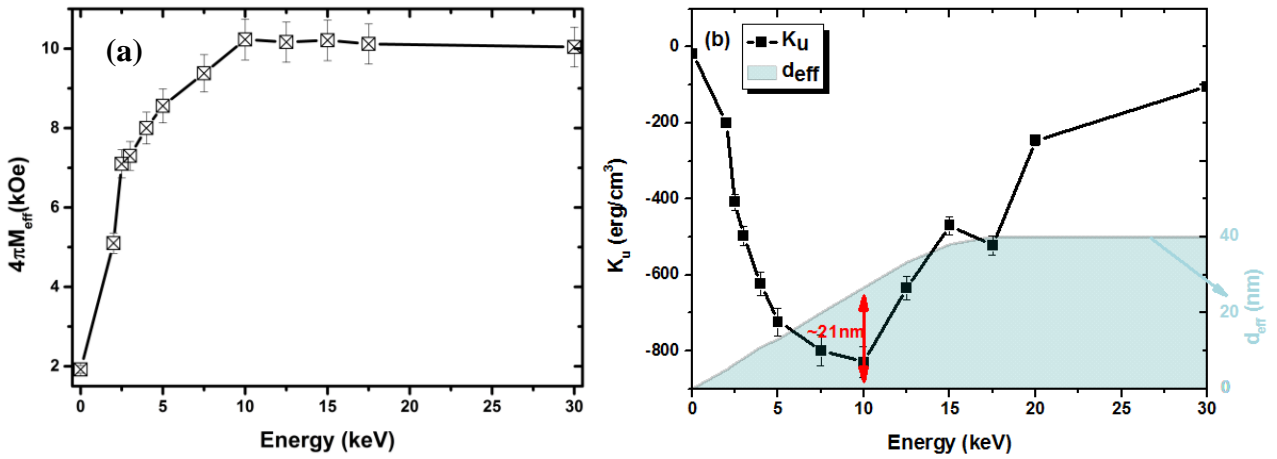


Figure 4.8: Magnetic parameters as a function of energy calculated from PMOKE hysteresis. (a) effective magnetization, and (b) effective uniaxial anisotropy.

LMOKE hysteresis loops for samples irradiated with energies of 2.5, 5, 7.5 and 30keV are shown in Fig. 4.9 (a). Hysteresis loops measured at various in-plane azimuthal angles did not show significant differences in H_c and remanance, suggesting that the samples are isotropic within the film plane (shown in the appendix). Fig. 4.9 (b) shows the dependence of the coercivity (H_c) and the effective magnetic thickness on the energy of irradiated ions. The

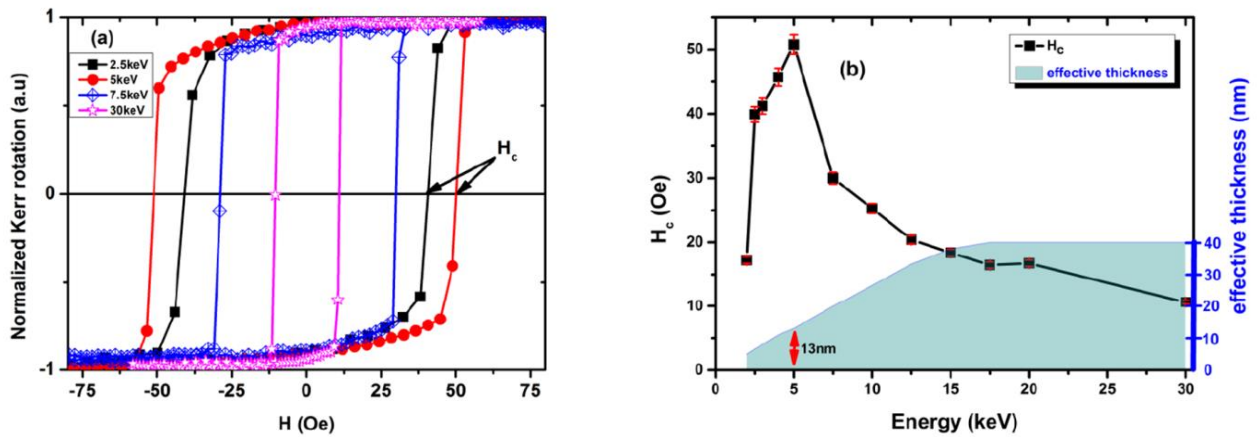


Figure 4.9: (a) LMOKE hysteresis for samples with irradiation energies of 2.5, 5, 10 and 30keV respectively. (b) Dependence of coercivity and effective thickness on the irradiation energy

effective magnetic thickness is expected to increase with increasing ion-energy, until the whole film has been penetrated beyond which the effective thickness remains 40 nm. A rapid increase in H_c is observed, until a maximum is reached for 5 keV ions corresponding to an effective magnetic thickness of 13 nm. As the ion energy is further increased, the H_c gradually decreases. For $E > 5\text{keV}$, H_c decreases from 51 Oe (ion energy of 5k eV) to 11 Oe (ion energy of 30keV) by a factor of ~ 4.7 . The sharp increase in H_c for $E < 5\text{keV}$ can be connected with increase in magnetic interaction between individual island. Similar dependence of H_c on film thickness was also observed in ultrathin Co [Kis03, Cam00]. The decrease in coercivity for $E > 5\text{keV}$ can be related to the increase in thickness where magnetization changes by domain wall motion (consistent with the experimental results of magnetization reversal explained later in discussion) [Sel02, Cul09].

4.1.3.2. Magnetization reversal study

Magnetization reversal (MR) was studied by imaging the change of the magnetic domain patterns in an applied reversal magnetic field (H_R), as a function of time (t). The scheme of the experimental procedure is shown in experimental section (Fig. 3.13). Initially the samples were magnetized by an applied magnetic field $-H_M$ parallel to the sample plane with field amplitude larger than its coercivity value. In the next step, at time $t = 0$ the reversal magnetic field H_R with opposite direction to $-H_M$ with $H_R < +H_c$ was applied inducing the magnetization reversal process. The values of the normalized magnetization (m) were calculated from the magnetic domain images for $t > 0$. Examples of such magnetic domain

patterns for samples irradiated with ion energies of 2.5, 5, 7.5, and 30keV are presented in Fig. 4.10.

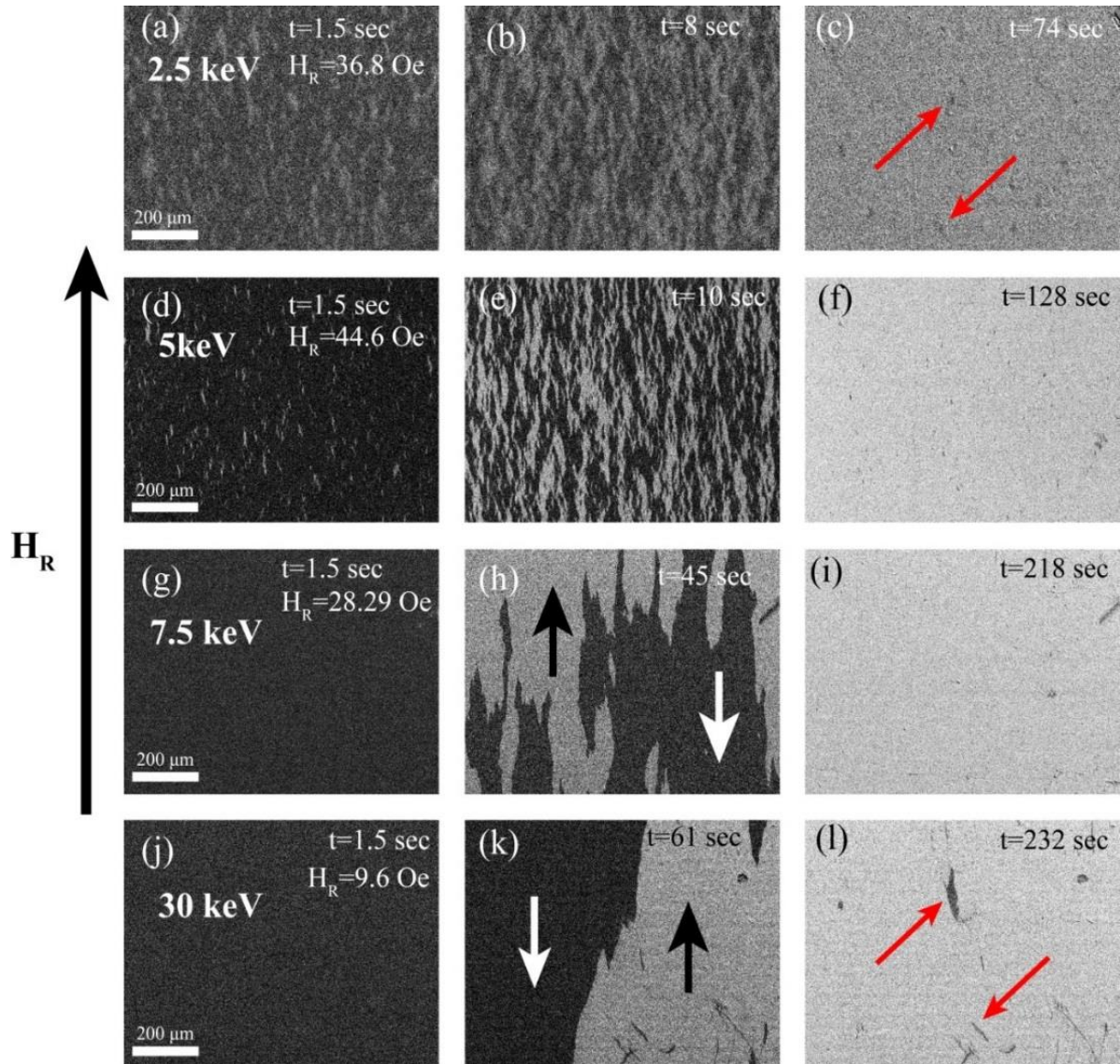


Figure 4.10: Magnetic field H_{II} driven evolution of magnetic domain structures with time registered for ion energy E : (i) 2.5keV (first row), $H_R = 36.8$ Oe. a) 1.5 sec, b) 8 sec, c) 74 sec; (ii) 5keV (second row), $H_R = 44.6$ Oe. d) 1.5 sec, e) 10 sec, f) 128sec; (iii) 7.5keV (third row), $H_R = 28.9$ Oe. g) 1.5 sec, h) 45 sec, i) 218 sec; (iv) 30keV (fourth row) $H_R = 9.6$ Oe, j) 1.5 sec, k) 61 sec, l) 232 sec). The black and white arrows show the direction of magnetization in domains.

In Figs. 4.10 the black areas correspond to the initially, un-switched domains, while white areas correspond to the switched domains with magnetization along the direction of the applied magnetic field H_R . Subsequent magnetization reversal cycles exhibit similar magnetic domain patterns although the location of black and white areas is statistical. The density of nucleation centers varies with ion energy. For samples irradiated with an ion energy of 2.5

keV, the evolution of magnetic domain patterns are shown in Figs. 4.10 (a-c) for H_R (26.8 Oe).

The magnetization reversal proceeds via nucleation of white domains, Fig. 4.10 (a). For the completion of the magnetization process the white domains coalesce (Fig. 4.10 (b)) approaching finally an almost saturated state. The small black non-reversed regions (magnetically harder) are still visible (Fig. 4.10 (c) shown by red arrows). The magnetization reversal processes for samples irradiated with ion energies $E \geq 7.5\text{keV}$ are different. Magnetic domain patterns for samples irradiated with E of 7.5keV and 30keV are shown in Figs. 4.10 (g-i) and Figs. 4.10 (j-l), respectively. For samples irradiated with $E \geq 7.5\text{keV}$, the magnetization reversal proceeds via a much smaller number of nucleation centers within the observation area (see Fig. 4.10 (g)). H_R driven white domains nucleate: (i) in both, inside selected places of the

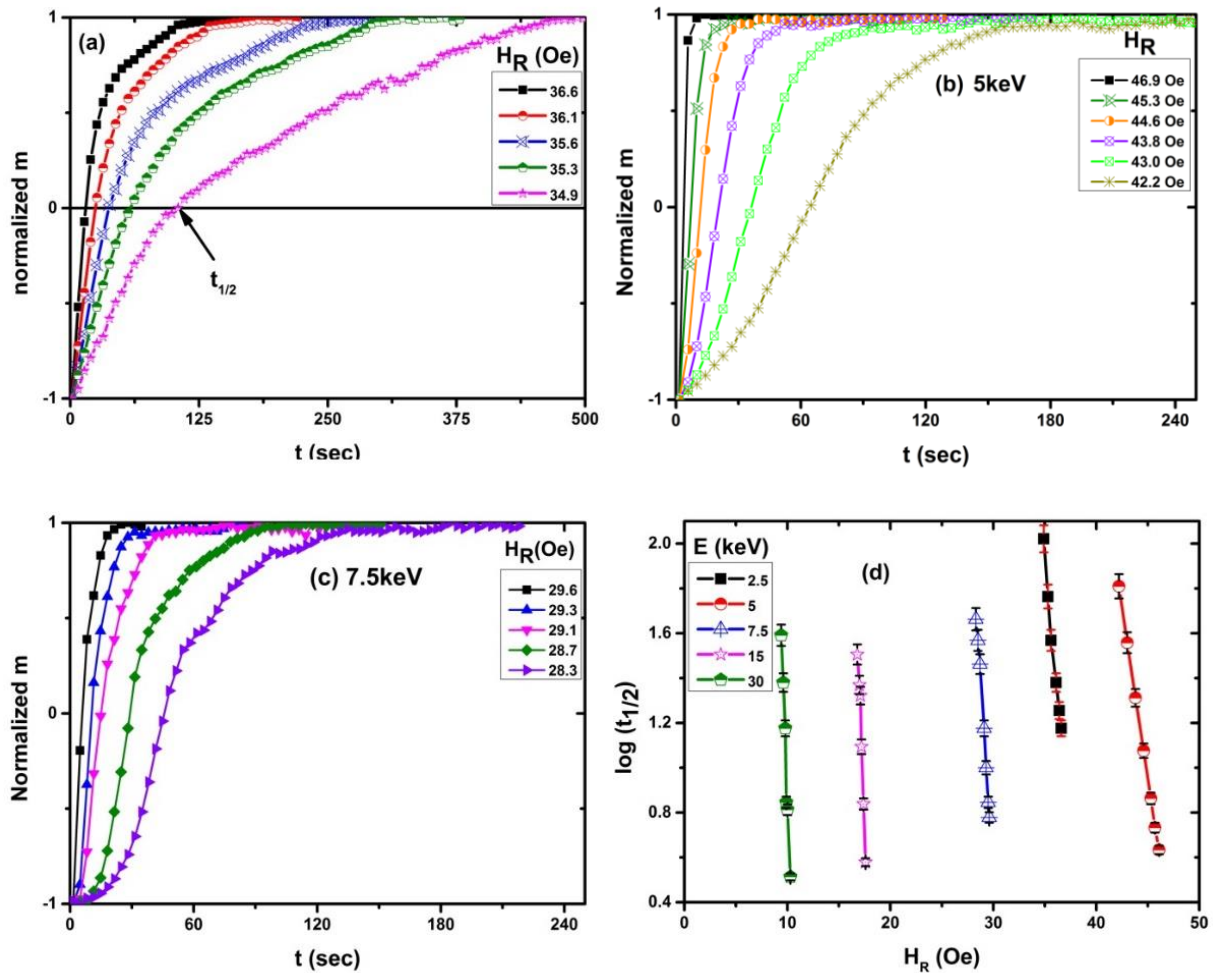


Figure 4.11: Time dependence of magnetization reversal for samples irradiated with different energy E . (a) 2.5keV, (b) 5keV, (c) 7.5keV, and (d) dependence of $\log t_{1/2}$ on H_R for samples irradiated with energies of 2.5, 5, 7.5, 15 and 30keV.

observation region as well as outside this region; (ii) outside the observation region (no nucleation in observation region, Fig. 4.10 (j)). The white domains grow in size through propagating with the preference of the applied field direction (Fig. 4.10 (h) and 4.10 (k)). Non-reversed black regions (hard centers) are still visible in Fig. 4.10 (l).

The Figs. 4.11 (a-c) show the time dependent normalized magnetization $m(t)$ reversal for samples irradiated with ion energy of 2.5, 5, and 7.5keV, respectively. By increasing the reversal field amplitude H_R the magnetization reversal proceeds faster as compared to the lower values of H_R . The reversal speed is characterized by the time $t_{1/2}$ needed to reverse half of the magnetization within the probed area. The Fig. 4.12 shows two MR curves constructed after considering only domain nucleation or only domain propagation mechanism basing on Fatuzzo-Labrune model [Fat62, Lab89]. By comparing the experimental relaxation curves, Figs. 4.11 (a-c) with Fig. 4.12, one can see (around $E = 5\text{keV}$) the crossover of magnetization reversal dominated by domain nucleation mechanism (almost exponential type) and dominated by domain wall propagation mechanism (S-shaped like). For $E > 5\text{keV}$, the shapes of the magnetization reversal curves suggest that MR is proceeded through domain wall propagation. This can also be confirmed with the help of the magnetic domain images, where one can see larger magnetic domains,

Figs. 4.10 (g, j). Intermediate shape of MR curve can be found for sample with $E = 5\text{keV}$ (Fig. 4.11) despite of large number of nucleation centers observed see Fig. 4.10(e). Fig. 4.11 (d) shows the logarithmic plots of the relaxation time ($t_{1/2}$) for samples irradiated with ion energies of 2.5, 5, 7.5, 15 and 30keV versus reversal field (H_R) where strong dependence of $t_{1/2}$ on H_R is visible. The dependence of $t_{1/2}$ on normalized H_R

is observed to be linear suggesting that magnetic aftereffect is due to thermal activation of magnetization reversal. The magnetization reversal analysis enables to estimate the Barkhausen volume to be in the range of $5 \times 10^{-24} \text{m}^3$.

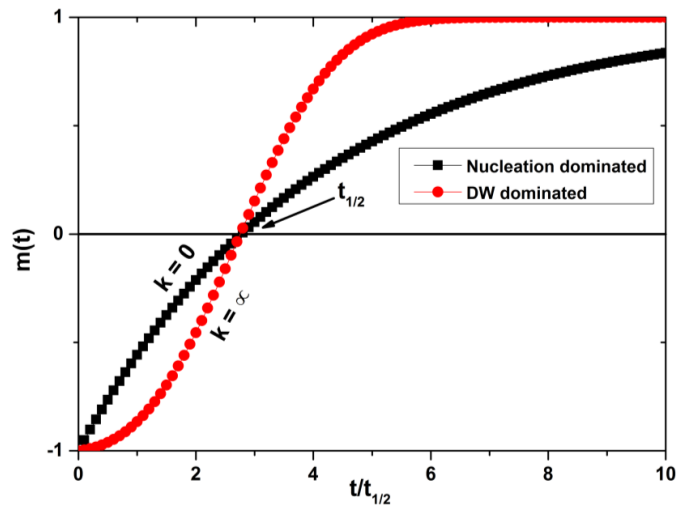


Figure 4.12: Time dependence magnetization relaxation curves: nucleation dominated (Black), and domain wall propagation (Red) based on Fauzzo and Lubrune model [Fat62, Lab89].

4.1.3.2. Magnetization reversal in reprogrammable 1D stripe

In this section the study of the dynamics of the magnetization reversal is carried out in 1D stripe. The details of the samples layout is described already in sample fabrication section 4.1.1.2. The samples with: (a) uniformly irradiated wire 10 μm wide and 400 μm long, was irradiated with 20 keV Ne⁺ ions at the fluence (6×10^{14} ions/cm²); and (b) 10 μm wide wire patterned by stripes with alternating 2 and 0.5 μm widths respectively separated by $\sim 40\text{nm}$ wide weakly magnetic spacers (see Fig 4.3, Fig. 4.4). The magnetic stripe pattern was generated by keeping the same irradiation conditions as for (a), however, performing the irradiation through a lithographed resist.

4.1.3.2.1. Magnetization reversal for uniformly irradiated stripe

Magnetization reversal process in uniformly irradiated 10 μm wide wire strongly depends on orientation of applied field (defined by ϕ_H angle measured from the wire axis), see inset of Fig. 4.13.

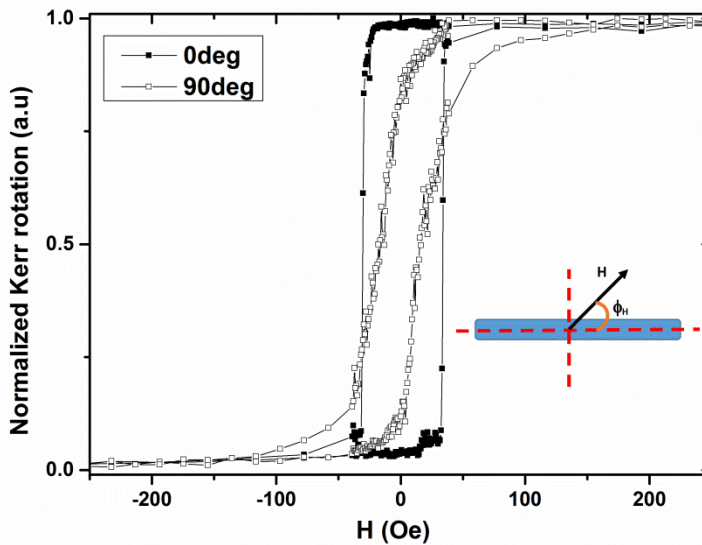


Figure 4.13: Comparison of hysteresis loops for different orientation of in-plane applied magnetic field. Inset shows the schematic of the applied field direction with respect to the wire major axes.

At $\phi_H = 90^\circ$, the wire takes higher applied field values for saturation and remanence value becomes smaller along with coercivity as compared to $\phi_H = 0^\circ$. This may be ascribed to the existence of magnetic shape anisotropy which creates an easy direction of magnetization along the wire axis, as expected from the high aspect ratio of the wire [Ebe97].



Figure 4.14: Evolution of magnetic domains for different field orientations. $\phi_H = 0$, a) appearance of large single domain, b) fully saturated wire. $\phi_H = 90^\circ$, c) appearance of multi-domain, d) fully saturated wire. The arrows show the direction of applied magnetic field.

The difference in magnetization reversal curves can be clarified by domain observations. For field applied along the wire axis, one can see domain propagation in the direction of applied field. For field applied at $\phi_H = 90^\circ$, magnetization reversal is carried out through multi-domain structures shown in Fig. 4.14(c). Stray fields generate the nucleation of many magnetization reversal (“white”) regions distributed quasi-periodically near the stripe edges.

4.1.3.2.2. Magnetization reversal study in 1D reprogrammable stripe

Magnetization reversal of wire patterned consisting of alternating 2 and 0.5 μm wide stripes respectively, undergoes a two staged reversal process [Bal14]. With sweeping magnetic field one obtain the following magnetic states evolution: (i) initial parallel state where (WA \uparrow /spacer/WB \uparrow); (ii) anti-parallel state (WB \uparrow /spacer/WA \downarrow); (iii) parallel state with reversed magnetizations (WB \downarrow /spacer/WA \uparrow); (iv) (WA \uparrow /spacer/WB \downarrow) state. Field driven domain state evolution is presented in Fig. 4.15 (b, c, d, and e). Switching between different magnetic states can be also deduced from magnetization hysteresis curve, see Fig. 4.15(f).

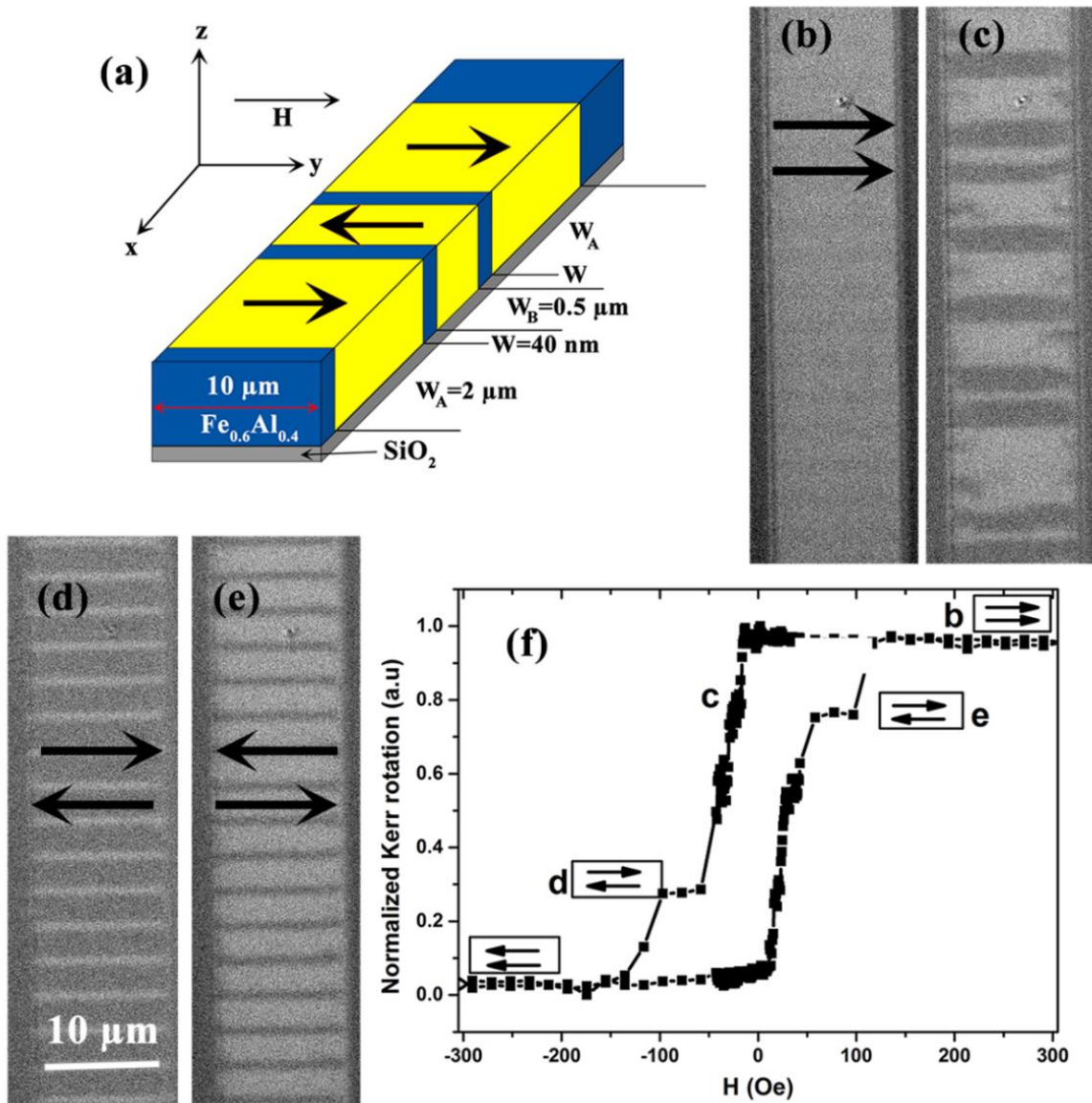


Figure 4.15: (a) Schematic of the magnetic nanopatterning, b) fully saturated magnetic state “ferromagnetically ordered stripes, c) Partially magnetically saturated W_A stripes, d) remnant image of stripes W_B by $H < 0$, e) Remnant image of fully saturated W_A for $H > 0$, f) Magnetic hysteresis loop showing two step reversal mechanism at which different stripes switches at different applied field giving rise to AFM configuration.

4.1.3. Study of magnetization dynamics

Materials exhibiting the above phenomena of disorder-induced ferromagnetism have yet to be investigated for their magnetization dynamics properties. Reliable estimates for technologically useful material parameter such as the exchange stiffness (A) is missing in the literature.

In the following part the study related to the dynamics of magnetization in $\text{Fe}_{60}\text{Al}_{40}$ 40 nm thin films is carried out wherein chemical disorder has been systematically induced using ions. As earlier shown in the statics measurements that the increase in the ion-energy leads to increase in their penetration depth, causing the formation of the A2 phase inside the deeper regions of the film. This implies that the effective thickness of the ferromagnetic phase increases with ion energy. Furthermore, the A2/B2 phase boundary is gradually pushed deeper into the film and finally expelled when the film is fully penetrated by the ions. The ability to adjust the depth-position of the A2/B2 phase boundary helps to investigate the possible pinning effects at this interface.

The dynamic response of the irradiated films by was studied by employing VNA-FMR which allows the variation of frequency and applied magnetic field [Bil07], and BLS spectroscopy along with analytical calculations.. Apart from the situations where nonzero wave vectors are introduced through finite geometry effects, (A2/B2 boundary in the present study) FMR is restricted to dipolar zero-wave-vector spin wave excitation (uniform mode). An example of nonzero wave vector situation is called standing spin waves (SSW) i.e., exchange-dominated modes with wave vector determined by the layer thickness. BLS spectroscopy with its sub-GHz resolution and high surface sensitivity (~ few nm) for metals is ideally suited for studying A2/B2 phase boundaries. All the measurements were carried out in backscattering geometry defined in experimental section 3.3.2.1 at room temperature.

Exemplary BLS spectra collected from samples irradiated with ion energies of 2.5 keV, 15 keV and 30 keV for various applied magnetic fields H and in-plane wave vectors q_{\parallel} are shown in Figs 4.16 (a, b), 4.16 (c, d) and 4.16 (e, f), respectively. The peaks position in both the Stokes (negative frequencies) and anti-Stokes (positive frequencies) part of the spectrum move towards higher frequencies upon increasing the external magnetic field , Figs. 4.16 (a, c and d), revealing their magnetic origin.

Furthermore it has also been observed that FWHM (Fig. 4.17) of DE mode decreases with increase in the irradiated energy. The decrease in FWHM could be related to the homogeneity of the ferromagnetic layer as similar thickness dependence of Py films have been found in the literature [Nib03]. The observed increase in the frequency of this particular mode with increasing ion-energy (Fig. 4.18) can be ascribed to the variation in saturation magnetization M_S with increase in ion energy observed up to ~ 5 keV, i.e., to the thickness of the transient region between A2 and B2 phases.

To better understand the origin of the observed modes, and their ion-energy-dependent occurrences, we performed measurements with VNA-FMR, to observe the dependence of the field position of the resonance peak on the excitation frequency (Fig. 4.19). As seen in Fig. 4.19 (a), a single spin wave frequency mode is observed for the 2.5 keV case, consistent with the BLS spectra of Fig. 4.16 (a-b). BLS measurements showed that this spin wave frequency mode has pronounced dispersion with the in-plane wave vector q_{\parallel} and it can be assumed as a magnetostatic surface wave, which propagates in the film plane (also known as the DE mode) see Figs. 4.16 (b, d and e).

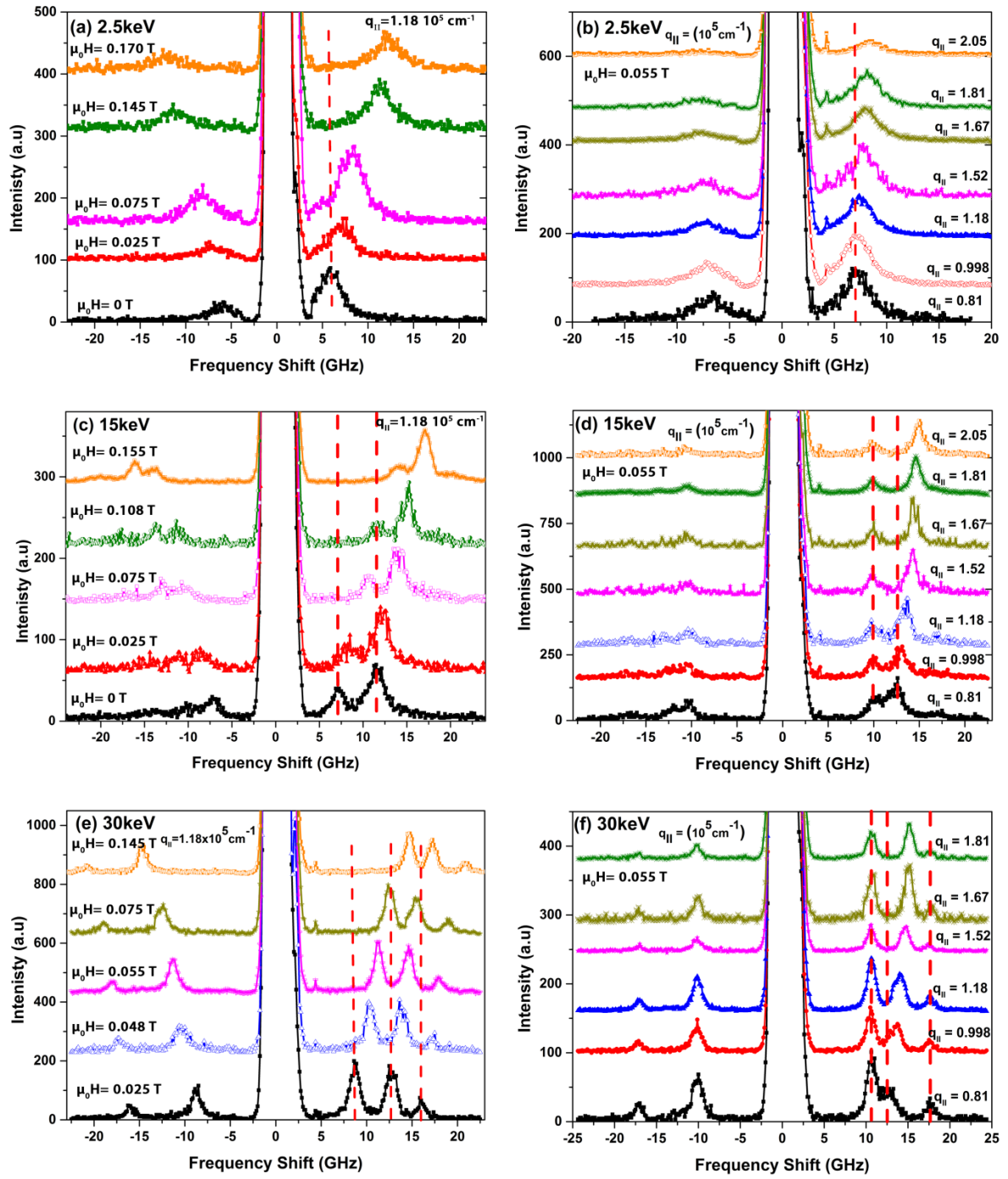


Figure 4.16: BLS spectra at different applied magnetic field values at a transferred wave vector of $1.18 \times 10^5 \text{ cm}^{-1}$ (a) 2.5 keV, (c) 15 keV, and (e) 30 keV. Dispersion characteristics at different angle of incidence θ , i.e different transferred wave vector $q_{||}$ at external magnetic field of 0.055 T (b) 2.5 keV, (d) 15 keV and (f) 30 keV.

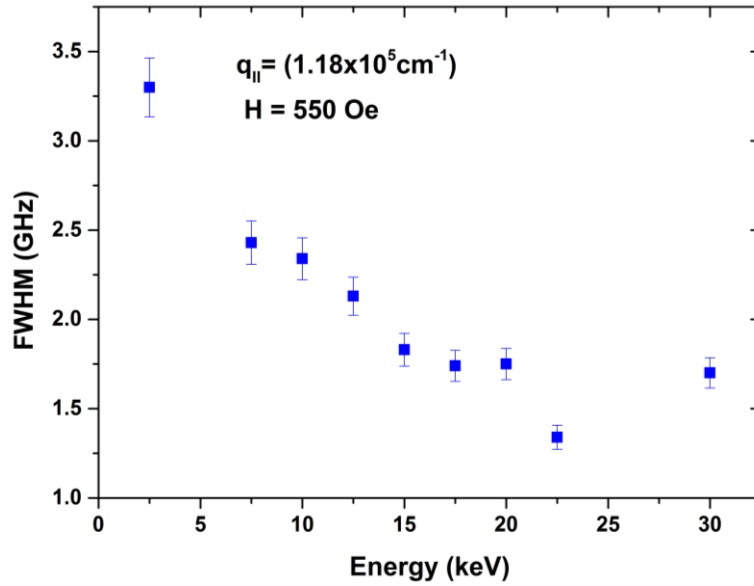


Fig. 4.17: Dependence of FWHM from DE mode (Description of applied field and q-vector are shown inset).

Depending on the ion irradiation energy (thickness of the modified layer) different modes observed by BLS spectra at external field of $\mu_0 H = 0.055$ T and $q_{||} = 0.81 \times 10^5 \text{ cm}^{-1}$ are summarized in Fig. 4.18.

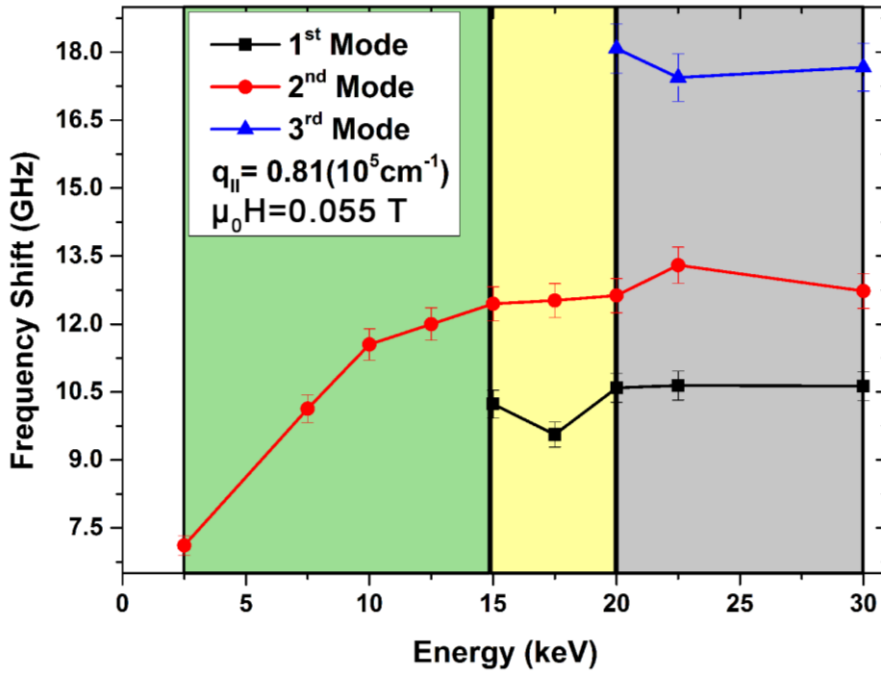


Fig. 4.18: Dependence of observed spin wave (SW) modes on energies of irradiated ions. The data are collected at $\mu_0 H = 0.0550$ T and $q_{||} = 0.81 \times 10^5 \text{ cm}^{-1}$.

In contrast to the case of 2.5 keV Ne^+ irradiation, the $\text{Fe}_{60}\text{Al}_{40}$ film irradiated with 15 keV Ne^+ showed two spin wave modes Fig. 4.16(c) (BLS) and Fig. 4.19(b) (VNA-FMR) with separation of ~ 3 GHz at $q_{\parallel} = 0$. Our theoretical analysis will show that in the 15 keV case, (Fig. 4.16(d)), the higher frequency mode showing a dispersion where dependence on q_{\parallel} can be ascribed to DE mode. The lower frequency mode showed negligible dispersion with q_{\parallel} and we can assume it to be an SSW mode. Furthermore, the sample irradiated with ion energy of 30 keV showed three spin wave frequencies modes in BLS (Fig. 4.16(e)) while single mode was observed in VNA-FMR, (see Fig. 4.19(c)). Here, the theoretical analysis will show that the low and high frequency modes are the SSW as they are dispersion-less while the middle spin wave frequency mode show strong dispersion characteristics on q_{\parallel} confirming it as DE mode.

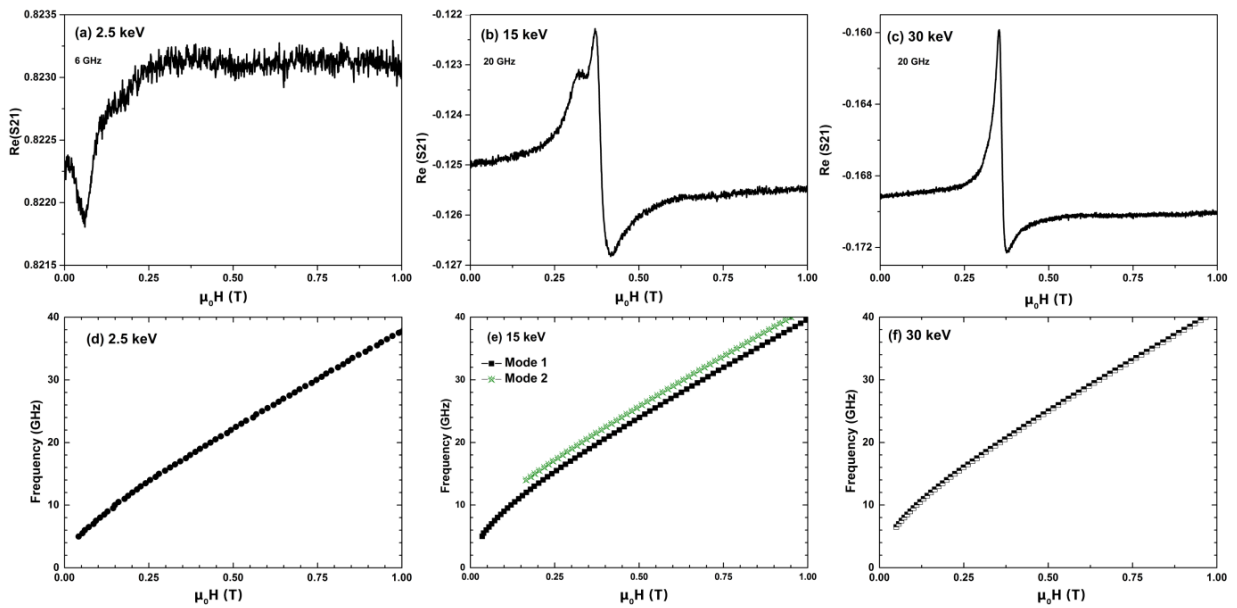


Fig. 4.19: The raw VNA-FMR spectra for sample irradiated with energies of 2.5, 15 and 30 keV in (a), (b) and (c), respectively. The measured frequency of spin-waves in dependence on the applied magnetic field for sample 2.5, 15 and 30 keV in (d), (e) and (f), respectively.

ANALYTICAL RESULTS

In order to understand the origin of experimentally observed spin wave modes, the experimental data have been fitted by employing two basic formulas: for the DE-modes (i.e., surface magnetostatic spin waves propagating perpendicularly to the external magnetic field) and for the exchange SSW-modes. Taking into account the influence of both dipolar and

exchange interactions DE-mode frequency in the system under consideration is given as [Sta09]:

$$f_{DE} = \frac{\gamma\mu_0}{2\pi} \sqrt{(H + \lambda q_{\parallel}^2)(H + \lambda q_{\parallel}^2 + M_s) + \frac{1}{4} M_s [1 - \exp(-2q_{\parallel}d)]} \quad (4.1)$$

Here μ_0 is magnetic permeability, γ – gyromagnetic ratio (we assume the value of 176.67 GHz/T), d – thickness of the ferromagnetic film, and $\lambda = 2A/\mu_0 M_s$, A being the exchange constant. For SSW we have used formula for the purely exchange spin waves [Sta09].

$$f_{SSW} = \frac{\gamma\mu_0}{2\pi} \sqrt{(H + \lambda(q_{\parallel}^2 + q_{\perp}^2))(H + \lambda(q_{\parallel}^2 + q_{\perp}^2) + M_s)} \quad (4.2)$$

where q_{\perp} is the wavenumber of the spin-wave across the film thickness. Other parameters are the same as for the DE-mode.

Wavenumber q_{\perp} describes allowed successive standing waves across the film thickness. Its value takes into account the thickness of the A2 phase and pinning of the magnetization dynamics on the film surfaces. The pinning of the spin wave dynamics at the surface of the ferromagnetic film can have different origin [Pus79, Hil87, Rap04, Bur11, Ped10, and Zho13]. Beside other sources, it can result also from variation of the magnetization or exchange interactions at the outermost area of the ferromagnetic film [Wig61, and Spa70]. A continuously vanishing magnetization at the border between phases A2 and B2 Fig. 4.2(a) is only a small part of the whole film. However, this (and probable associated change of the exchange constant) can influence spin wave spectra. Thus, it is reasonable that the border between magnetized and paramagnetic part of the Fe₆₀Al₄₀ film formed by ion irradiation effectively modifies boundary conditions of the SSW formation and allowed values of q_{\perp} . We will look for q_{\perp} in the form $q_{\perp} = (n - \eta)\pi/d$, where n is a mode number and η describes the change of the wavenumber due to pinning and takes values from 0 to 1. We use standard form of the boundary conditions for the dynamical components of the magnetization vector \mathbf{m} , to derive η :

$$\left[\frac{\partial \mathbf{m}}{\partial z} + p_{0(d)} \mathbf{m} \right]_{z=0(d)} = 0, \quad (4.3)$$

where p_0 and p_d are pinning parameters on two boundaries of the film, the free surface and at the border between A2 and B2 phases, respectively. The derivative is calculated along normal to the film plane (along z -axis).

The relationship between wavenumber q_{\perp} and pinning parameters for the SSW modes is obtained from solvability condition of Eqs. (4. 3) by assuming harmonic solutions for \mathbf{m} [Gur96, and Bur11]:

$$\tan[q_{\perp}d] = \frac{q_{\perp}(p_0 + p_d)}{2q_{\perp}^2 - p_0p_d} \quad (4.4)$$

Assuming natural pinning on the free surface ($p_0 = 0$) one can obtain following formula for the pinning parameter at the border between A2 and B2 phase in its dependence on η :

$$p_d = \frac{2\pi}{d}(n - \eta) \tan[\pi(n - \eta)] \quad (4.5)$$

We shall comment, that in the model considered here the thickness of the A2 phase d is an ambiguous value, and so the p_d value. Because, by inspection of the Fig. 4.2 (a) it is clear that, the d can be chosen arbitrary from the value where magnetization starts to decrease up to the value where it drops to 0. For further consideration we chose the value d where M_S takes a value equal to a half of the maximal magnetization saturation, according with Fig. 4.2 (a) these are 40, 35 and 8.5 nm for ion energies of 30 keV, 15 keV and 2.5 keV, respectively. However, the most important for interpretation is the sign of p_d which points at the pinning or un-pinning of the magnetization at the surfaces of the film. The estimation of η is free from this ambiguity.

To take into account magnetization pinning at the interface between A2 and B2 phase in Eq. (4. 1) we use approximate approach by introducing an effective magnetization instead of M_S [Nib03]:

$$M_S \rightarrow M_{S,\text{eff}} \equiv M_S - \frac{2(K_{S1} + K_{S2})}{\mu_0 M_S d}, \quad (4. 6)$$

where K_{S1} and K_{S2} are surface anisotropy constants at the free surface and the border between A2 and B2 phases, respectively. According with the discussion regarding SSW we also here assume $K_{S1} = 0$, then Eq. (4. 6) reads:

$$M_{S,\text{eff}} \equiv M_S - \frac{2K_{S2}}{\mu_0 M_S d}, \quad (4. 7)$$

where K_{S2} is proportional to the pinning parameter p_d : $K_{S2} = Ap_d$ [Gur96].

To estimate effect of the pinning we fit theoretical curves obtained from Eqs. (4. 1) and (4. 2) to the experimental data obtained from BLS and collected in Figs. 4.20. DE-mode is strongly dependent on M_S and only slightly on A , thus we estimated M_S from the fitting of the Eq. (4. 1) to the experimental data. The SSW modes are very sensitive to A and also to the pinning (q_\perp), thus Eq. (4. 2) is used to estimate exchange constant. We assume natural pinning on both surfaces ($\eta = 0$, $p_d = 0$ and $K_S = 0$) in the case of 30 keV, because the entire thickness of the layer ($d = 40$ nm) is ferromagnetic and mostly homogeneous, with both surfaces sharp. So, for this case we can find M_S from fitting of Eq. (4. 1) to the DE-mode and A from the fitting of Eq. (4. 2) to the two SSW modes found experimentally, Fig. 4.19 (e and f). The value of 0.880×10^6 A/m and 0.41×10^{-11} J/m is found for M_S and A , respectively, and used throughout the paper. Obtained values of M_S and A are collected also in Table 4.1. Then, we use these values of M_S and A to the sample irradiated with 15 keV. The fitting of Eq. (2) to the BLS results Figs. 4.20 (c and d) required $\eta = 0.3$. From Eq. (4. 4) we get $p_d \approx 0.17 \text{ nm}^{-1}$ which is comparable with values obtained for FePt thin films [Bur11]. The positive sign of η indicates for so called unpinning, which means the freedom of the spins at the A2/B2 phase boundary larger than natural [Pus79]. Similar results are presented in Ref. [Spa70], where unpinning were found to be result of decreasing magnetization, just like in our case. According to the theory of the surface spin wave [Pus79], the positive (according to the boundary condition Eq. (4. 3)) pinning parameter promotes the surface spin waves of the exchange origin (different from the DE mode). However, they can appear in the measured spectra, only when the magnetization saturation is out of plane or at angle smaller than some critical angle with respect to the normal [Ram76]. In the case of 15 keV irradiation, the effective magnetization of the sample as estimated from Eq. (4. 6) is only slightly lower, than M_S , i.e. $M_{\text{eff}} = 0.838 \times 10^6$ A/m. Thus, the influence of the pinning on DE-mode in this case is

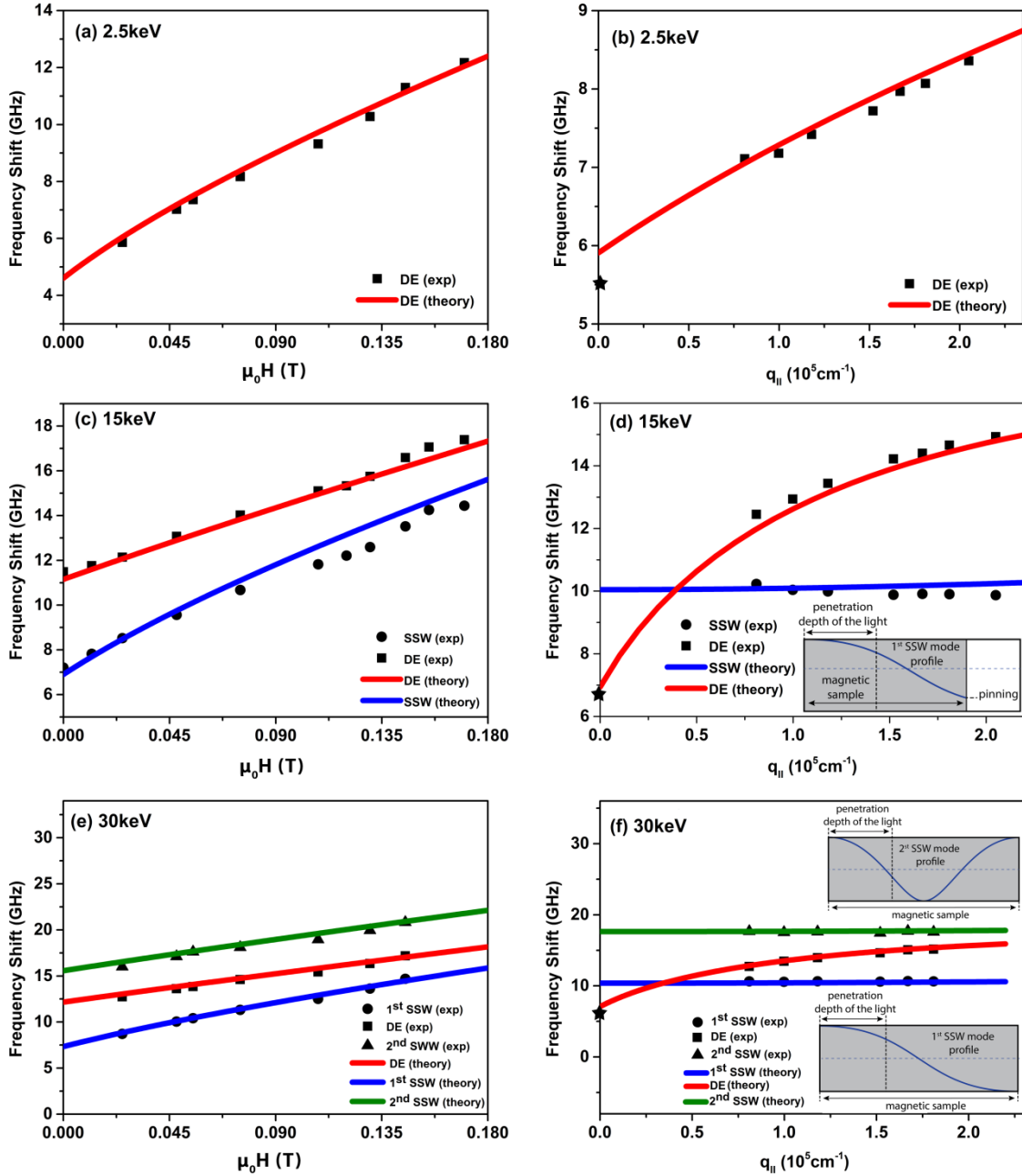


Fig. 4.20: Dependence of the spin wave frequency on the applied magnetic field at fixed $q_{||} = 0.81 \times 10^5 \text{ cm}^{-1}$ (a, c and e) and transferred wave vector $q_{||}$ at fixed external field $\mu_0 H = 0.055 \text{ T}$ (b, d and f) for samples irradiated with ion energies 2.5 keV (a, b), 15 keV (c, d) and 30 keV (e, f). Solid lines-show theory and solid points show experimental results from measurements by BLS (squares, circles and triangles) and VNA-FMR (stars). In the insets of (d) and (f) the sketches of the SSW profiles visible in BLS are shown with the dashed vertical line marked penetration depth of the light in BLS measurements.

insignificant. Also for this sample a good agreement with the experimental data is found for frequency of DE-mode in dependence on magnitude of the magnetic field as well as on wavevector, as shown in Fig. 4.20 (c) and (d), respectively.

For the sample irradiated with ion energy of 2.5 keV there is only DE-mode observed in BLS and FMR, thus we need only M_s to fit experimental data (the SSW are not considered, due to its high frequency exceeding considered range). In this case the saturation magnetization is expected to be reduced (see Ref. [Bal14]) as compared to its bulk value. According with this, the obtained value from fitting to Eq. (4. 1) is reduced as compared to the previous samples with taken into account the same pinning as in the previous sample ($p_d \approx 0.17 \text{ nm}^{-1}$ and $M_{\text{eff}} = 0.595 \times 10^6 \text{ A/m}$).

Table 4.1: Fitting parameters for BLS spectra: thickness of the A2 phase, magnetization saturation, exchange constant, and pinning at the A2/B2 interface.

Ion-energy (keV)	Magnetic film thickness (nm)	M_s (kA m^{-1})	A (10^{-11} J/m)	Pinning at the A2/B2 interface
2.5	8.5	705	0.41	Yes
15	35	880	0.41	Yes
30	40	880	0.41	No

The light has limiting depth of penetration into the metallic FeAl. If we assume that most of the signal is typically obtained from the top $\sim 10 \text{ nm}$ of the film then as shown in Fig 4.2(a), the signal in BLS spectrometer under normal incidence is collected from the 1/4 of thickness of the sample 30 keV. In 15 keV sample it is collected from the 1/3 of the ferromagnetic film thickness and for 2.5 keV from the whole sample. In FMR the dynamic magnetic radio-frequency field penetrate whole samples, thus the FMR intensity in the homogeneous thin film is proportional to the integral from SW amplitude across the total A2 phase thickness. Samples irradiated with ion energy of 2.5 keV showed in measurements only single spin wave mode Figs.4.16 (a, b). According to Eq. (4. 2) already the first SSW is out of the experimental range of frequencies, independent on the pinning. Thus we are not able to estimate the pinning parameter from SSW analysis (we assumed the same value of pinning as for 15 keV sample). This is consistent with FMR Fig. 4.19 (a) measurements, where the only single line is observed, which is the DE mode. In samples irradiated with ion energies of 15 keV, due to gradual decrease of the magnetization (probably associated with the decrease of

the exchange constant) at one surface of the ferromagnetic film we expect the change of the effective pinning of the magnetization dynamics at this border. For asymmetric boundary conditions the intensity from the SSW resonances is nonzero, especially for the 1st SSW Fig. 4.20 (d). The separation between DE mode and 1st SSW at $q_{\parallel} = 0$ is found to be 3.1 GHz in 0.055 T magnetic field which is close to the experimental value, see FMR results in Fig. 4.19 (b). At 30 keV, the irradiated ions have enough energy to penetrate the entire sample (i.e., entire thickness of the sample is ferromagnetic). Because of the limited penetration depth of the BLS two lowest SSW modes Figs. 4.20 (e, f) are observed while the 3rd one not, while in FMR measurements the magnetization dynamics is symmetric on both surfaces (the free magnetization) thus the FMR intensity from all SSW modes is 0 and the only observed mode is DE mode Fig. 4.19 (c).

Summary

Depending on an ion energy evolution of magnetic domain patterns and mechanisms in reversal processes were studied by employing LMOKE techniques. The maximum H_c was found around an ion energy of 5keV, corresponding to an effective magnetic film thickness of 13 nm which identifies the crossover from single domain to multi-domain behavior. This was further verified from the study of magnetic domain images and time dependence M_R curves, where for ($E \leq 5\text{keV}$), MR was dominated through nucleation centers (large numbers of nucleation centers) and for $E > 5\text{keV}$, MR was processed through domain wall propagation (a fewer nucleation centers). Our findings suggest that the effect of higher ion-energy (larger effective magnetic thickness) on the coercivity is similar as in conventional magnetic system such as Co where H_c , and magnetization reversal process depends on the thickness of the ferromagnetic layer. In 1D reprogrammable stripe patterned sample, the existence of binary re-programmable magnetization configurations, demonstrates the possibility to apply disorder induced ferromagnetic structures for future study of this system as Magnonic Crystals. Depending on energies of the irradiated ions, DE and SSW modes have been identified; for $E < 15\text{keV}$, only the DE mode is detected, for $15 \leq E < 20\text{keV}$, a lower frequency SSW is induced, and for $E \geq 20\text{keV}$, the DE mode is observed to lie in-between two SSW modes. The transient magnetization at the A2/B2 interface acts as asymmetric spin wave pinning site. Pinning of spin-wave modes was considered in the analytical calculations, and a good agreement with the experimental observations. Ion-irradiation of $\text{Fe}_{60}\text{Al}_{40}$ can therefore provide a way to tune magnetization dynamics, such as by inducing spin-wave pinning at

selected film depths. Materials where properties such as the saturation magnetization and spin wave pinning can be modulated are of huge relevance in the field of magnonics, which seeks to exploit spin-waves for device applications.

4.2. Patterned (antidot lattices) Py

4.2. Nanopatterns of Py

During last few years, there has been much interest in fabricating artificially engineered materials with modulating magnetic properties. The magnetic properties of thin films can be controlled through fabricating various micron and nano-patterns by different patterning techniques such as, deposition through a shadow mask, e-beam lithography, FIB, X-ray lithography, nanoimprint lithography, and interference lithography [Lod04]. Patterned magnetic nanostructures are researched and developed for fundamental studies and applications in areas such as nanomagnets, ultra high density storage, spinelectronic devices, memory cells (MRAM) magnetic logic devices [Fer98, Gom96, Kra97]. Alternatively, antidots structures (the reverse of isolated nanostructures) form another class of magnetic nanostructures in which arrays of holes are embedded into contiguous magnetic materials. Antidots are artificially engineered “defects” in an otherwise continuous film. The antidote lattice (ADL) has also been proposed as a competitor for high density storage media, with characteristics of high stability while avoiding the superparamagnetic limit [Cow97]. Due to the advances in the fabrication technology the proper arrangement of these antidots can lead to change in magnetic properties of the thin films in controllable manner [Ade08]. Such structures can be regarded as an example of two-dimensional (2D) artificial magnonic crystal (MC) where propagating spin waves are used to transmit and process information without the use of electric current [Khi08, Sch08]. Effect of antidot shape (square, circular, elliptical), size, interspacing distance, and arrangement (square lattice, honeycomb lattice, rhombic lattice) on statics (magnetization reversal), and dynamics of magnetization (spin waves) have been carried out by different techniques [Tri10, Tac10, Wan06]. There is still quest to know: how ADL tune the statics and dynamics of magnetization, triggers to study this subject as a part of current dissertation where effect of systematic addition of antidots on statics and dynamics of magnetization has been studied.

4.2.1. Sample fabrication

Large area ($4 \times 4 \text{ mm}^2$) $\text{Ni}_{80}\text{Fe}_{20}$ (Permalloy (Py)) antidot nanostructures were patterned on commercially available silicon (Si) substrates by employing DUV lithography at 248 nm exposing wavelength. In order to create patterns in the resist, the substrate was spin coated with 60 nm thick bottom anti-reflecting coating (BARC) followed by a 480 nm positive deep UV-photoresist which is four to five time thicker than those typically used for e-beam lithography. Thicker resist helps to achieve high aspect ratio and additionally makes the lift-off process easier. A Nikon lithographic scanner with KrF excimer laser radiation was used to

expose the resist. In order to transfer resist patterns into antidots, 10 nm thick Py was deposited at room temperature by e-beam evaporation technique at rate of 0.2 Å/s while the pressure in the chamber was maintained at 2×10^{-6} Torr [Sin04]. The schematic of the sample

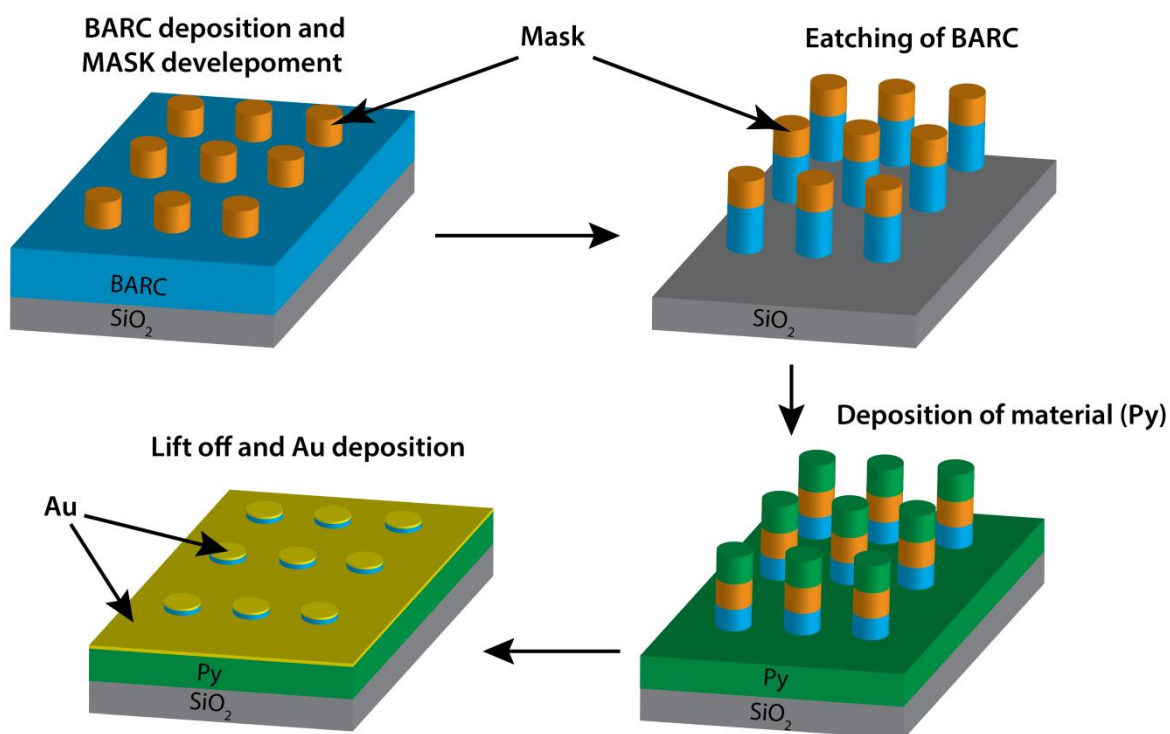


Figure 4.21. Schematic of the sample fabrication steps.

fabrication steps is shown in Fig. 4.21.

The samples with various geometries starting from basic (unit) structure “uniform antidots in square lattice”, to more complex system (wave-like pattern) by systematically inclusion of additional antidots (Bicomponent antidots with alternating diameters) were fabricated through the above discussed procedure. In order to keep the edges of the structures sharp, the last step the sample fabrication process (lift-off of BARC) was not carried out so BARC is present inside the antidots lattice which is confirmed from SEM and AFM analysis.

4.2.2. Structural analysis

Structural analysis was carried out through scanning electron microscope (SEM) and atomic force microscope (AFM).

4.2.2.1. SEM analysis

SEM analysis was carried out by employing ZEISS EVO HD15 microscope located at IFPAN, Warsaw.

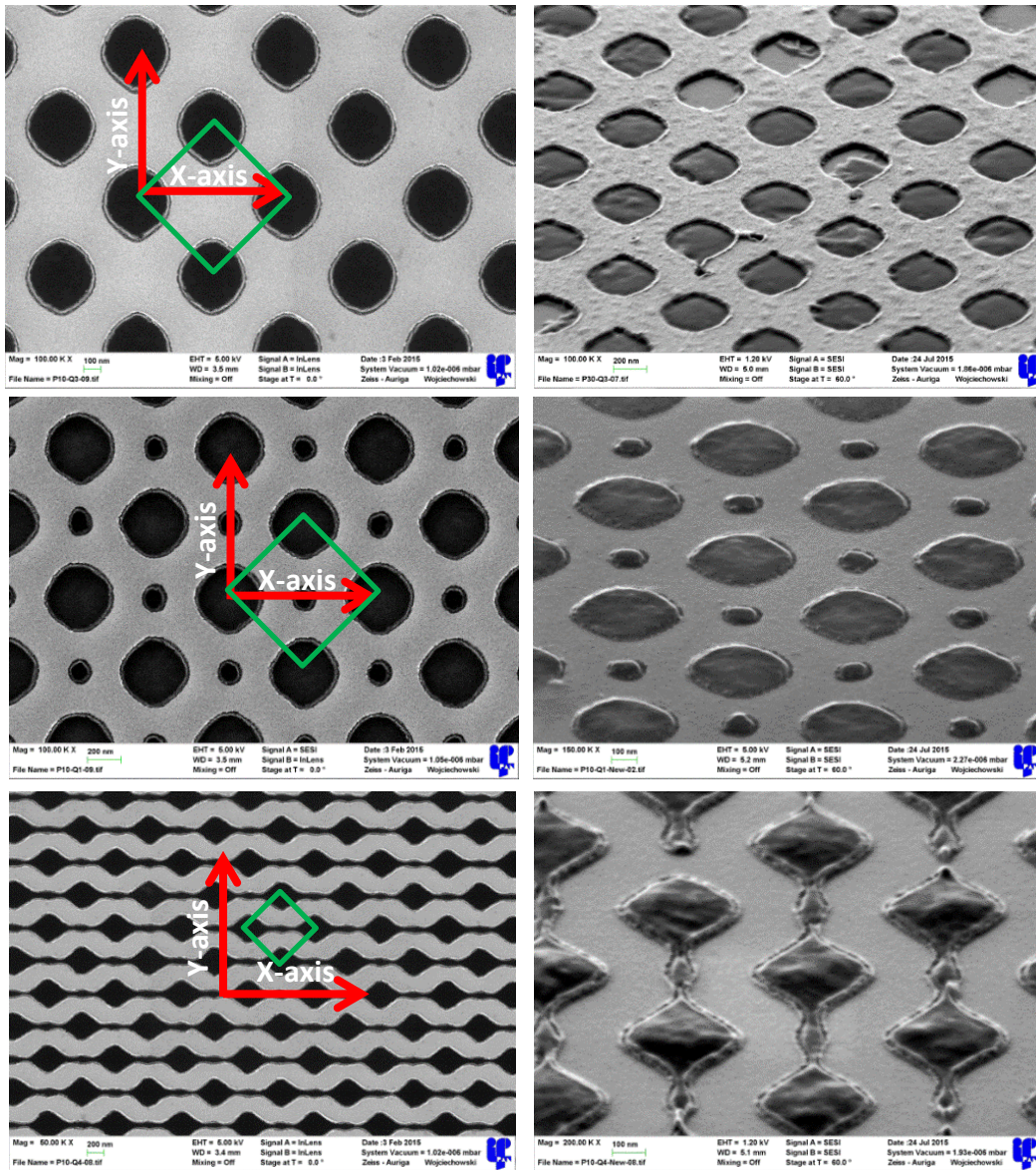


Figure 4.22. SEM micrograph (a-c) topographic, (d-f) tilted at 60° for square ADL, Square ADL with additional antidot inside the unit cel and wave-like patterns respectively One can clearly see that holes are filled with organic material (BARC).

As one can see from SEM micrograph, that holes are filled with BARC material which was left in order to keep the boundary of the holes sharp. The presence of BARC was further confirmed through energy dispersive X-ray analysis (EDX). The structural parameters

estimated from the SEM analysis are shown in the table 4.2. The nomenclature used for the samples are described as: reference sample (Ref_Py10), circular antidots (Theta_Py10_3), Bicomponent antidots lattice with alternative diameters (Theta_Py10_1), and wave-like patterns (Theta_Py10_4), where Py10 means thickness of the Py is 10 nm and these names will be used throughout the dissertation.

Table 4.2: Structural parameters of nanopatterns of Py extracted from SEM analysis.

Sr#	Names in Bialystok	Structures	Bigger size dia(nm)	Smaller size dia(nm)	Center to center distance (nm)	Thickness (nm)
1	Ref-Py10	Uniform film				10
2	Theta-Py10-3	Circular anti-dots (square antidot lattice (ADL))	405(along x-axis) and 450(Y-axis)	-	650	10
3	Theta-Py10-1	Square ADL with additional smaller antidot	410	140	650	10
4	Theta-Py10-4	Wave-like			580	10

4.2.2.2. AFM analysis

Atomic force microscope (AFM) provides better structural analysis because of high resolution of the order of few nm. Figure 4.23 shows the exemplary micrograph for theta_Py10_1, theta_Py10_3, and theta_Py10_4.

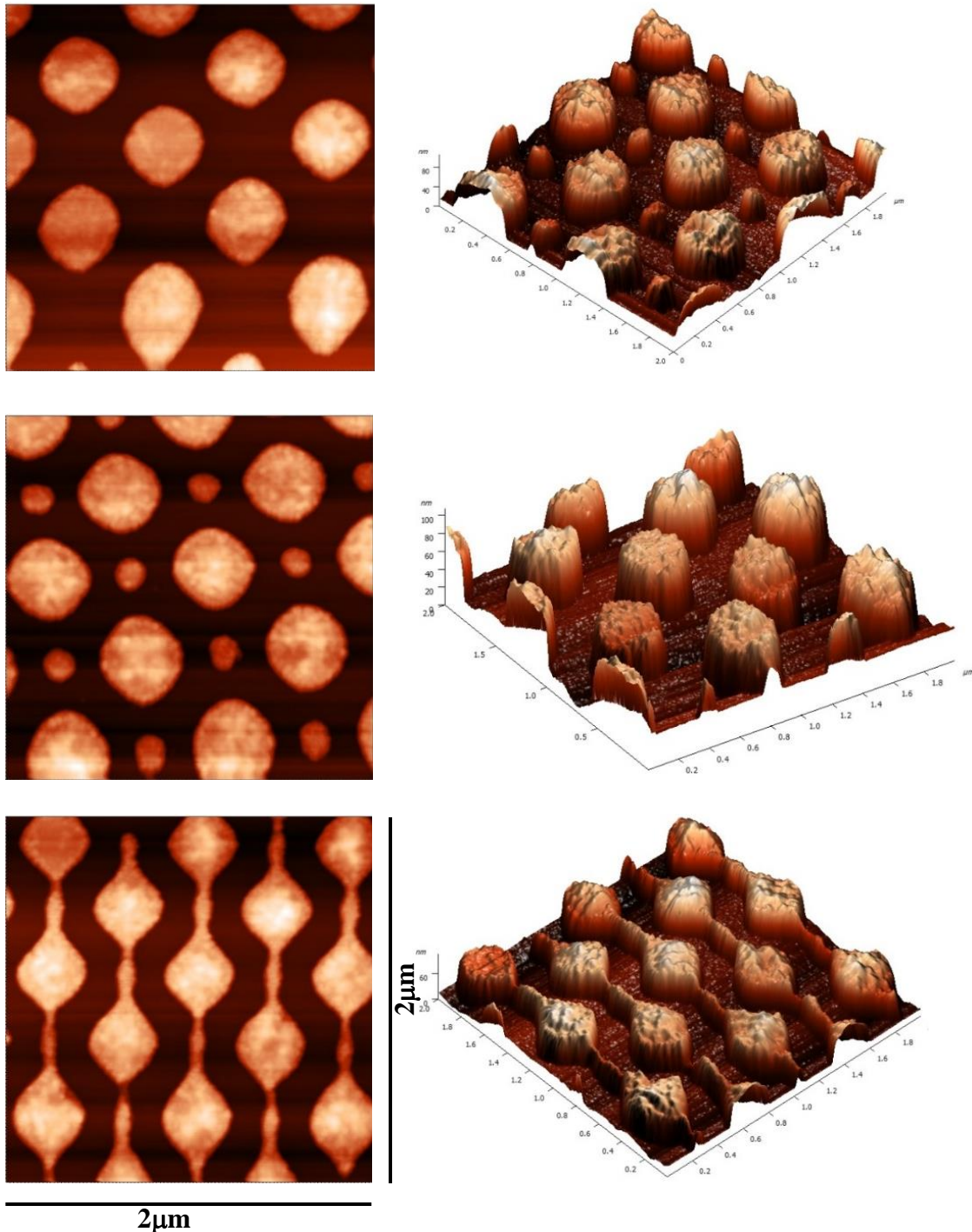


Figure 4.23. AMF images (a-c) topographic, (d-f) 3D for square ADL, square ADL with additional antidot, and wave-like ADL respectively. The light area corresponds to the BARC (confirms the height) while darker region is Py.

4.2.3. Statics measurements

It has been demonstrated that by fabricating symmetry order of the ADL, the local magnetic anisotropy distribution can be altered [Tri10, Cas04, Vav02, Ade08]. The statics measurements were carried out by employing LMOKE microscopy where magnetization

reversal has been carried out for in-plane angle to study the anisotropy related with the patterns. All the measurements were carried out room temperature.

Figure 4.24 shows the LMOKE hysteresis for Ref_Py10 for selected in-planes angles (0, 40, 90, and 180 degree).

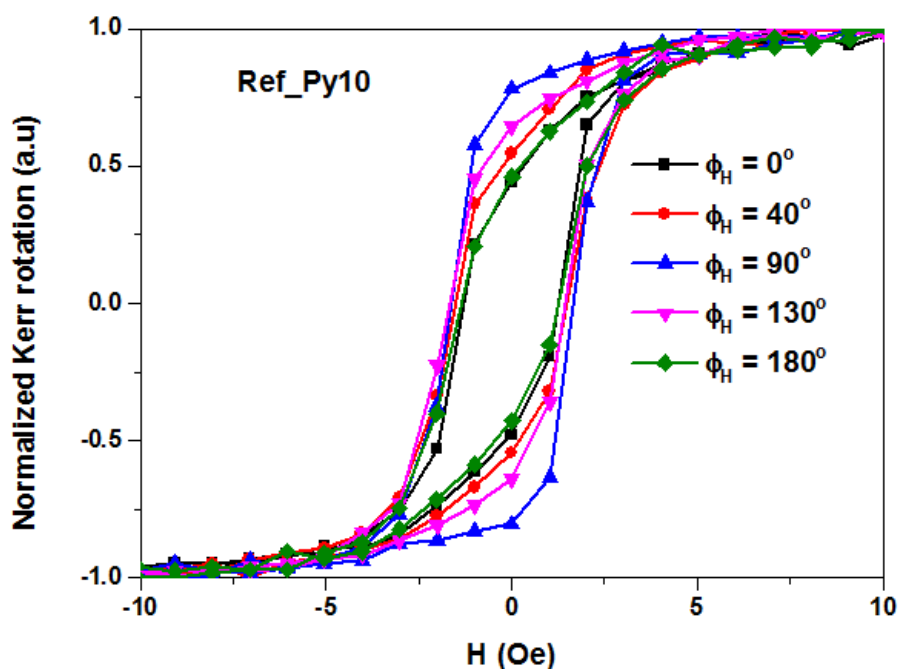


Figure 4.24. LMOKE hysteresis loops of reference sample (Ref_Py10) for different in-plane angles.

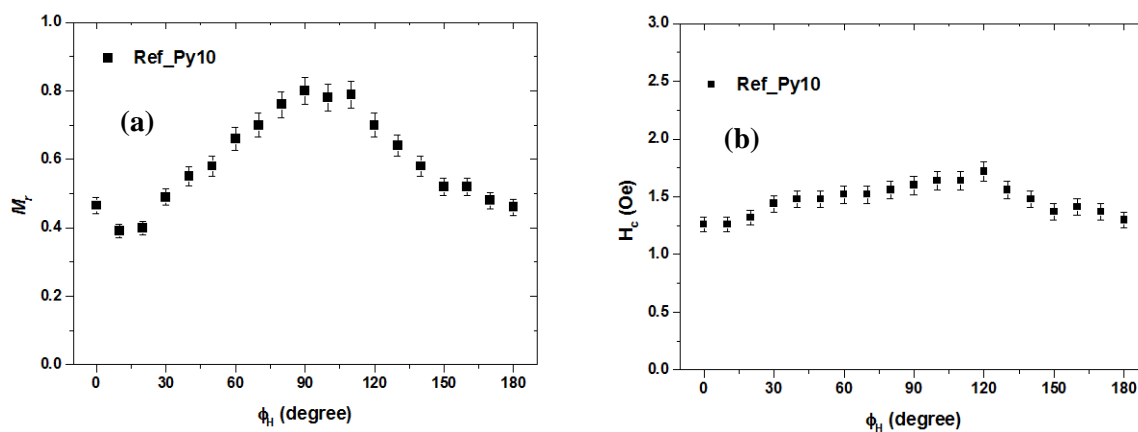


Figure 4.25. Angular dependence of (a) remanent magnetization (M_r) and (b) H_c for reference sample.

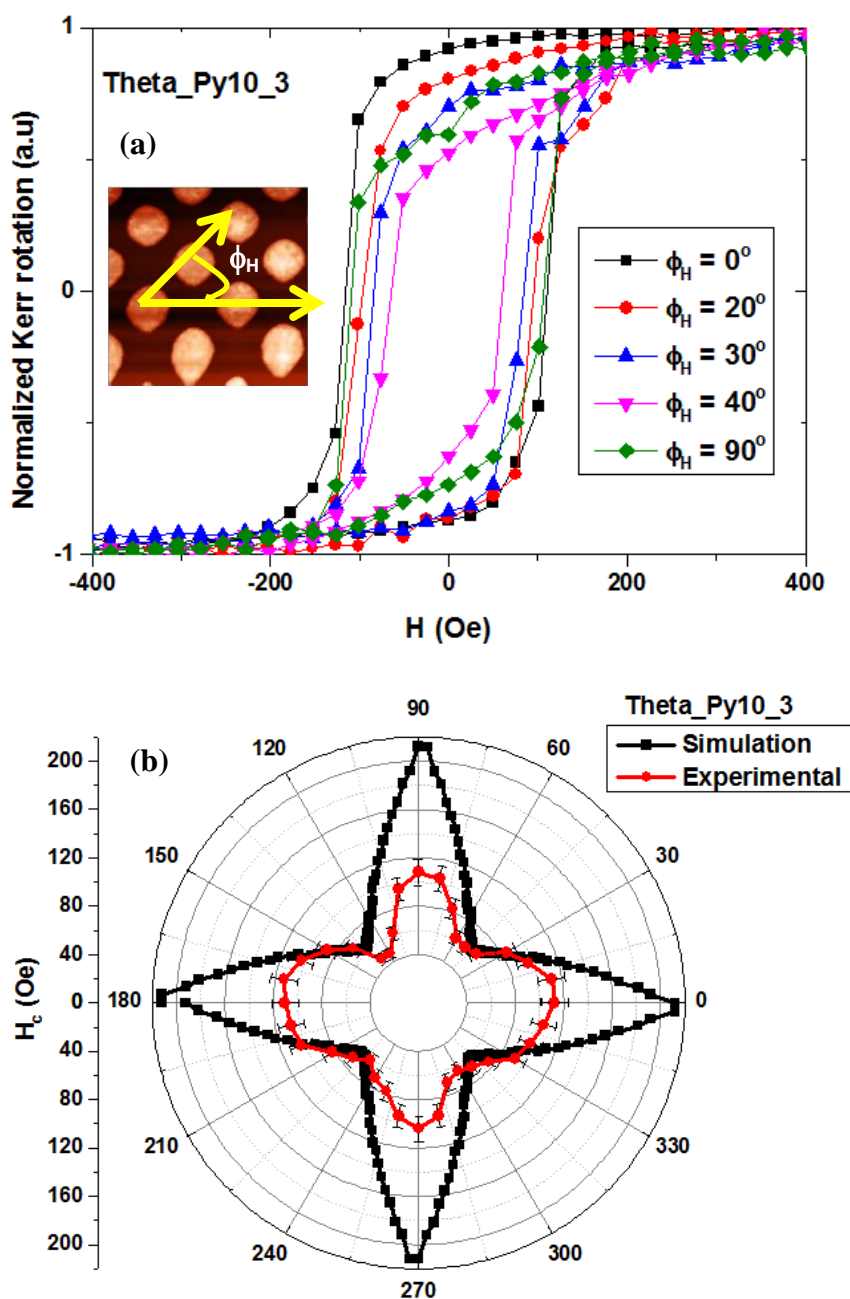


Figure 4.26. (a) LMOKE hysteresis for in-plane angles of 0, 20, 30, 40, and 90° . (b) Polar plot showing comparison of simulated and experimental H_c for Theta_Py10_3.

It has been observed that reference sample possesses a very small in-plane isotropy as it can be observed from the hysteresis loops, Fig. 4.24. The corresponding values of remanent magnetization and coercivity are shown in Fig 4.25 (a) and (b) respectively. It can be seen that the change in H_c is very small (<1 Oe) which states that continuous films (reference samples) have weak uniaxial anisotropy due to the polycrystalline nature of the film and absence of field induced anisotropy [Wan06, Ade08].

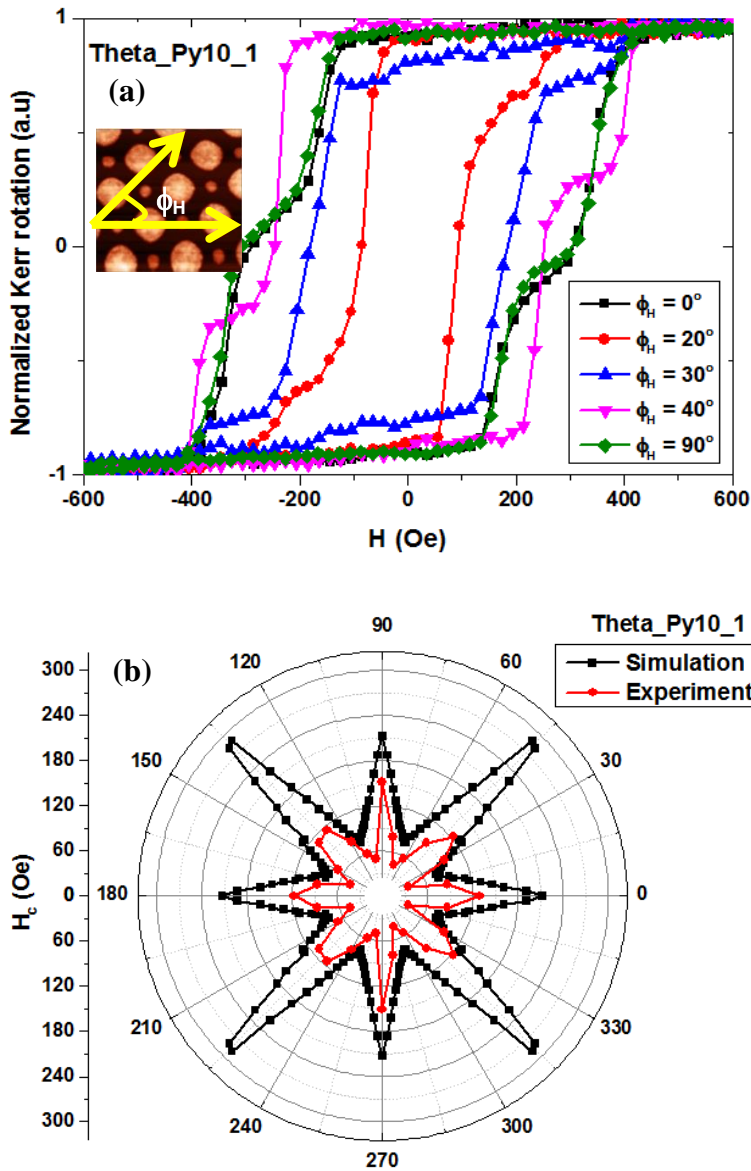


Figure 4.27. (a) LMOKE hysteresis for in-plane angles of 0, 20, 30, 40, and 90° . (b) Polar plot showing comparison of simulated and experimental H_c for Theta_Py10_1.

In square ADL (theta_Py10_3), Fig. 4.26 (a) shows a remarkable increase in H_c as compared to the reference sample. It has been seen that for $\phi_H = 0^\circ$ almost square-like hysteresis loop suggest easy axis while for $\phi_H = 30-40^\circ$ shape of hysteresis and decrease in the H_c suggests hard axis (Fig. 4.26 (a)). The arrangement for the measurements is shown in inset of Fig. 4.22 (a). From the LMOKE hysteresis one can see that remanent magnetization for in-plane angle 0° and 90° are larger as compared to 40° which is hard axis (being closest neighbors). Magnetization hysteresis loop for 40° suggests that magnetization reverses smoother along the hard axis. Clear in-plane four fold symmetry (biaxial anisotropy) with the

hard axes along the edges of the square ADL and easy axis along with diagonal direction can be seen from Fig. 4.26 (b) which is related to the ADL symmetry.

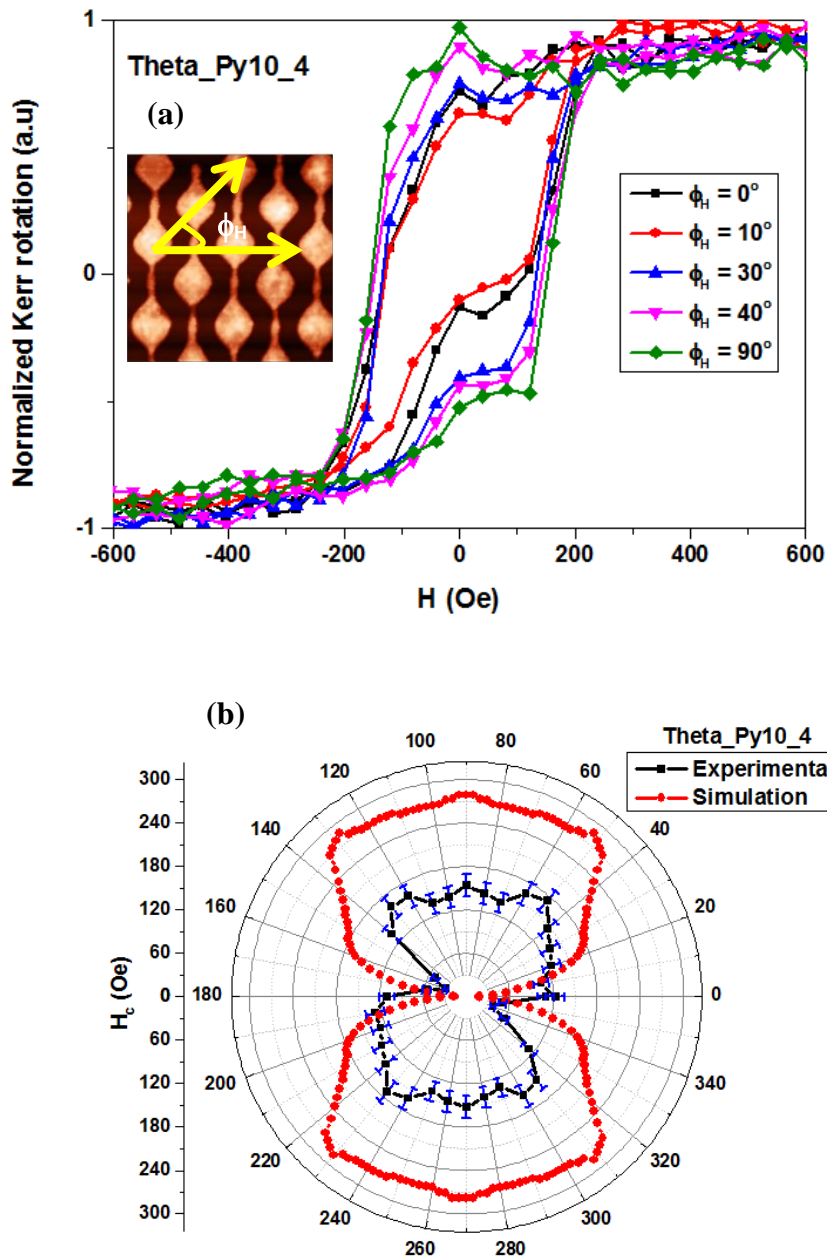


Figure 4.28. (a) LMOKE hysteresis for in-plane angles of 0, 10, 30, 40, and 90°. (b) Polar plot showing comparison of simulated and experimental H_c for Theta_Py10_4.

LMOKE results with additional antidots (in comparison to basic structure, Theta_Py10_1) inside the square ADL are summarized in Fig. 4.27. One can see that with

inclusion of additional antidot in the basic structure (square antidot lattice), the anisotropy from four fold symmetry to eight fold symmetry have been observed, Fig. 4.27(b). From the LMOKE hysteresis loops it is clear that magnetization reversal goes through via two steps reversal mechanisms. In the case of field applied X and Y-axis as defined in Fig. 4.22(c), the larger antidots are connected through smaller antidots while in the case of square lattice it was easy axis (larger distance between antidots). It has been observed that these axes remains still easy axes as large H_c can be seen in Fig. 4.27(b). During magnetization reversal, going from positive field to negative field direction, first the magnetic domains around larger antidots are unpinned and while reaching larger negative field the magnetic domains around smaller antidots are unpinned. More details analysis can be performed through simulation in the next coming paragraphs.

In the third case when larger and smaller antidots are connected which makes the wave-like shape (Fig. 4.22(e-f)), the results from LMOKE measurements are summarized in Fig. 4.28. The exemplary hysteresis loops for certain in-plane angles are shown in Fig. 4.28 (a). There is decrease in H_c and remanence values at in-plane angle of 10° and 170° being a symmetric structures. It has can be seen from LMOKE hysteresis and H_c dependence that easy/hard axis can be observed when the field is along/perpendicular to the direction of the wave-like patterns which is along X/Y-axis respectively in the Fig. 4.22(e). Clearly two-fold symmetry has been observed Fig. 4.28(b).

The increase in H_c after patterning could be related to the nanomagnetic vacancies, which hinder the domain wall movement [Vav02]. The observed increase in H_c after patterning is similar for all studied three geometries. From the in-plane dependence of H_c we can conclude that ADL induces an in-plane anisotropy. The induced easy and hard axes become the directions along which the antidots are furthest apart and closest to each other respectively. The origin of the patterning induced anisotropy can be understood from the following considerations: the surface “charges” that appear at the interface between magnetic material and the antidots, through demagnetizing field, to the formation of the magnetic domains as the external field is progressively lowered from the saturation state.

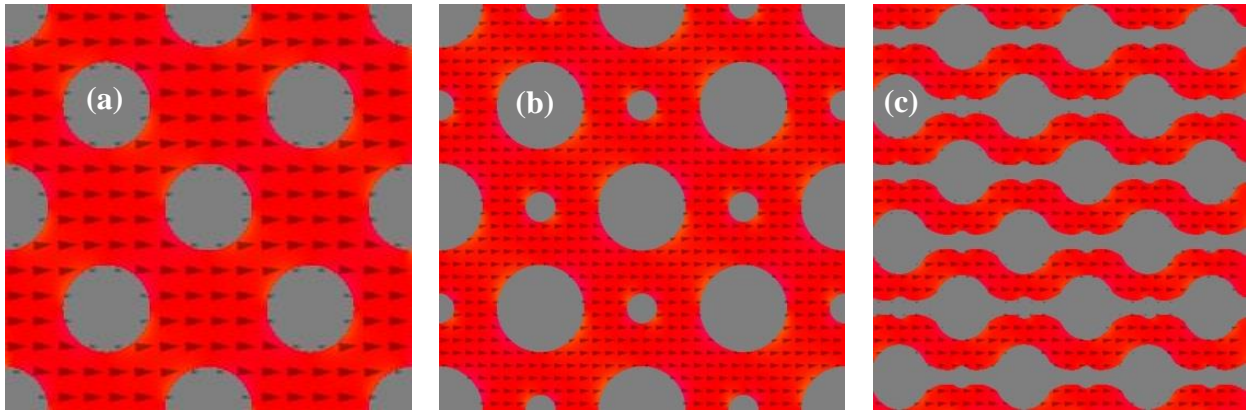


Figure 4.29. The simulation models for the three studied geometries (a) circular antidots, (b) Square antidot lattice with additional smaller antidot (c) wave-like patterns

In order to explain the magnetic anisotropy behavior in above shown results in Fig. 4.26(b), Fig. 4.27(b), and Fig. 4.28(b), an understanding of the distribution of the microscopic spin orientation in such structures is needed, since net effect of the magnetic moments along the applied magnetic field leads to the observed remanent magnetization. This was achieved through performing micromagnetic simulations for the remanent spin states using MuMax simulation [Van11]. The simulation models for three studied geometries are shown in Fig. 4.29. The magnetic parameters used for simulations are saturation magnetization (M_s) = 860 kAm⁻¹, exchange constant $A = 13 \times 10^{-12}$ Jm⁻¹, and anisotropy constant $K_u = 0$ [Wan06]. Numbers of cells are 256 and grid is about 2.5 nm. Periodic boundary conditions with 8 times repetitions and with built-in function edge smoothing to overcome staircase effects was employed. The external magnetic field in all measurements was kept same which is 0.2 T.

Figure 4.30 (a) and (b) shows the in-plane magnetization curve in the longitudinal configuration (field is applied along the side of the square ADL) at room temperature for sample thickness 10nm and magnetization distribution at different field values from the MuMax simulation respectively. At positive saturation field, all the spins in the ADL are aligned to the direction of the field. The corresponding remanent images are marked from 1 to 6 (Fig. 4.30 (b)). After reducing field progressively from saturation, the surface charges at the boundaries between antidots and magnetic layer lead to the formation of the domains through demagnetizing field, Fig. 4.30 (b). When the field is increased in the opposite direction, the increase or decrease of the individual domain areas continues until the critical field of about 0.0205T at which magnetization switching is activated. The results are in agreement with the literature [Yu00] with ADL where such domains are resulted due to the smooth decrease of

the component of magnetization parallel to the applied field. When the external field is applied along the direction where antidots are closest to each other in our case (45°), these domains may coalesce more easily (i.e. when the external field is not reversed yet) to form bands of 90° rotated spins connecting the holes along the field direction. With such configuration of spins system can reduce its magnetostatic energy by reducing the extension of domain wall creating larger domains with 90° rotated spins, which can expand easily when applied field is successively reversed. The loops measured along such direction will show hard-axis-like shape, Fig. 4.26(a).

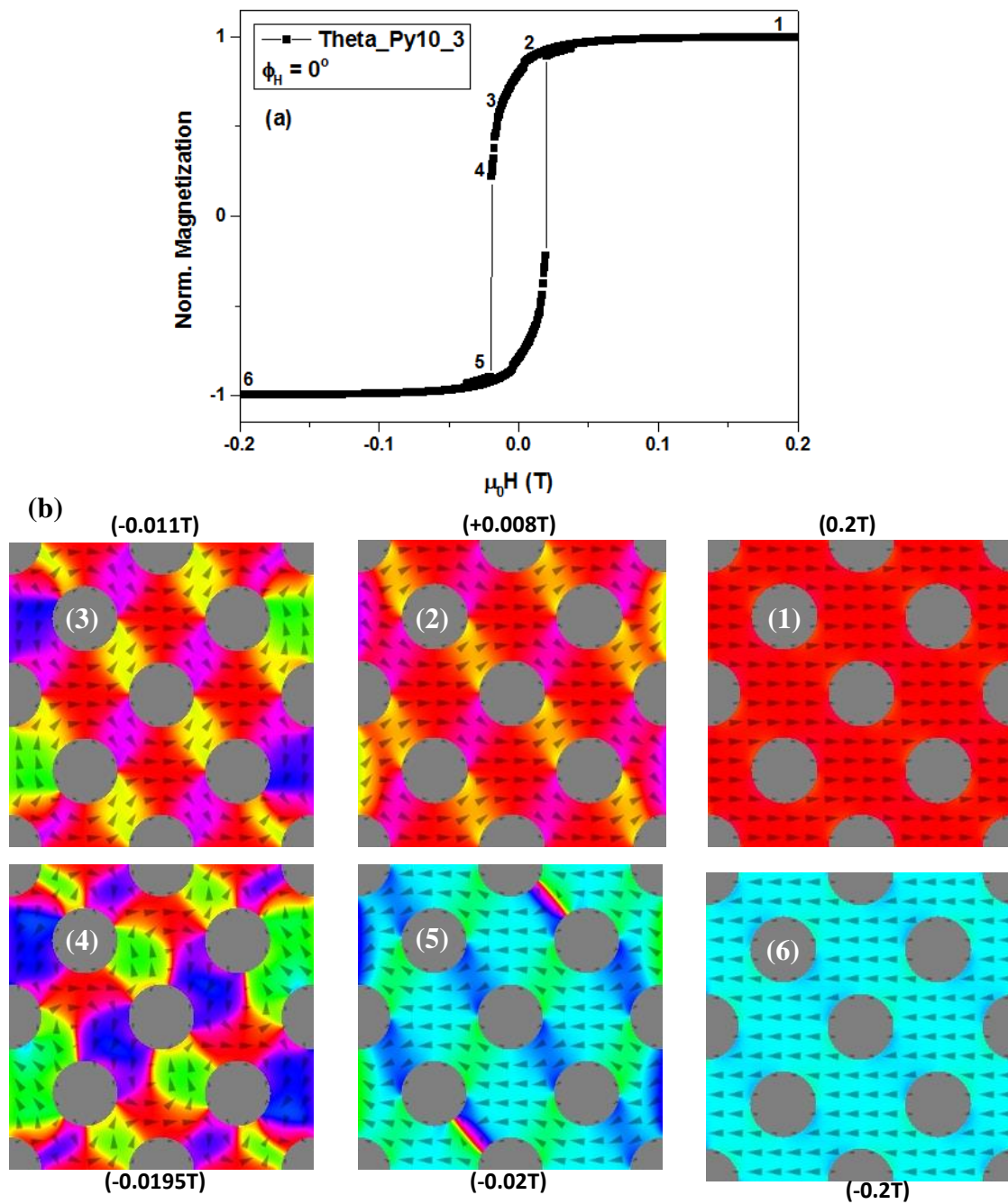


Figure 4.30: (a) Magnetic hysteresis while the sample is magnetized in-plane for $\phi_H = 0^\circ$. (b) Magnetization distribution obtained from MuMax simulation for different magnetization reversal values Theta_Py10_3 .

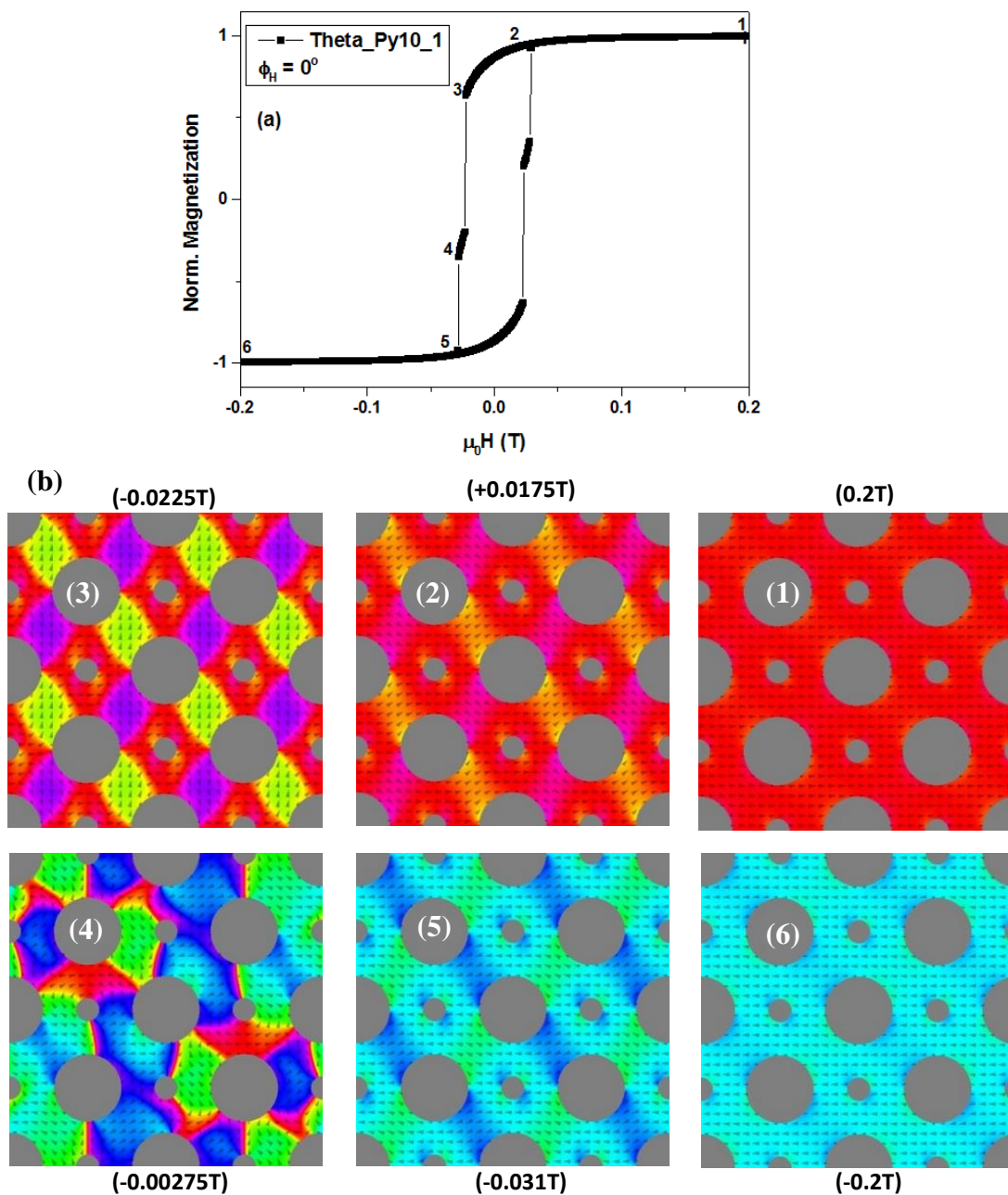


Figure 4.31. (a) Magnetic hysteresis while the sample is magnetized in-plane for $\phi_H = 0^\circ$. (b) Magnetization distribution obtained from MuMax simulation for different magnetization reversal values_Theta_Py10_1.

The magnetization reversal for the ADL with alternative diameters of antidots can be explained through Fig. 4.31. Experimental we have observed that when we compared to homogenous circular antidots with comparable dimensions and film composition, the magnetization reversal mechanism is markedly modified due to the alternating dimensions of adjacent antidots. The two step-hysteresis loop from LMOKE measurements (Fig. 4.28(a)), suggests reversal process through two different switching field. At positive saturation field all

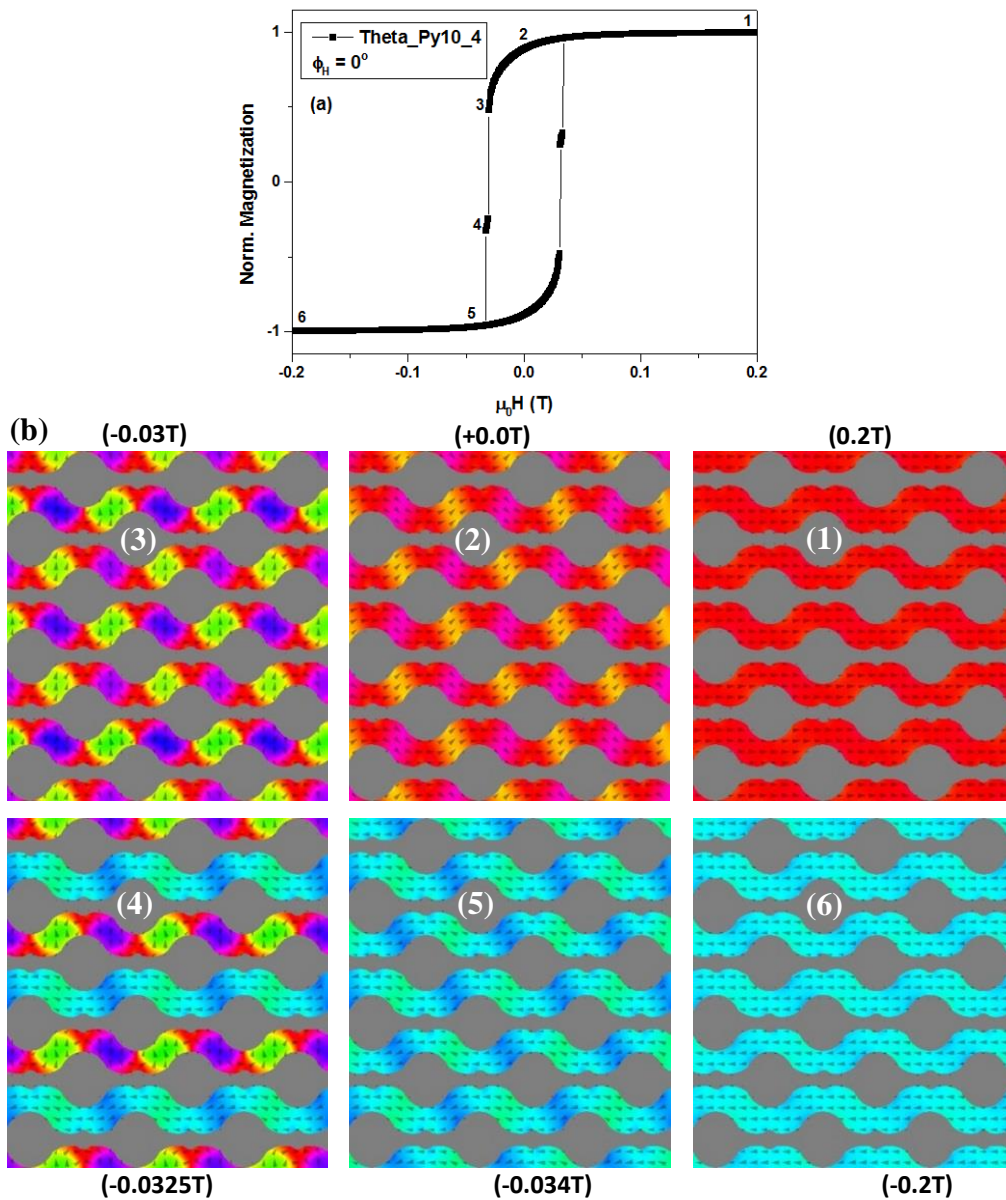


Figure 4.32. (a) Magnetic hysteresis while the sample is magnetized in-plane for $\phi_H = 0^\circ$. (b) Magnetization distribution obtained from MuMax simulation for different magnetization reversal values_Theta_Py10_4.

the spins in the ADL are aligned along the field direction. As in the case of square ADL, similarly domain formation because of surface charges have been observed due to the demagnetizing field around the boundary between antidots and magnetic film, Fig. 4.31(b). The results are comparable to the literature [Tri10]. As the field is increased in the reverse direction, the magnetization start decreasing due to the rotation of the magnetic domains until the critical switching field is reached. With further increased in reverse direction, magnetization decreases sharply till the ordered domain configuration, with both the wedge shaped domain between each large/small having undergone a 180° magnetization rotation. The magnetic domains are pinned around the smaller antidots and they require larger reversal

field to switch which is visible also in Fig. 4. 31(b.4). With the addition of hole/holes (antidot/antidots), the contribution of the surface energy becomes larger and blade-like magnetic domains appears as similar results have been observed in the literature [Vav98, Vav02, Fea02, and Tri10].

The simulated results for wave-like patterns are summarized in Fig. 4.32. The magnetization reversal mechanism follows the trend as it was observed for Theta_Py10_3, and Theta_Py10_3 except blade-like domain formation. One can see in the remanent image Fig. 4.32(b) mentioned by 2, during applying applied field in reverse direction, the domains at the edges of the wave-like patterns where larger holes are present try to align along the direction of the applied field. in 3rd remanent image one can see with further increase in reversal field, the area of the edge domains increases and domains are at 90° as compared to the domains between narrower regions of the wave-like patterns due to the larger demagnetizing field. As the applied field reached around 0.25T there is sudden jump in magnetization because of the switching of the domains around the narrower regions [Gue02, and Gue03]. In the final stage (6) after applying sufficient reversal field all the domains are aligned parallel to the applied field direction.

The experimental results agree qualitatively with the simulated results, filled black squares in Fig. 4.26(b), Fig. 4.27(b) and Fig. 4.28(b). The small discrepancy can be related to the small mismatch in the real shape of the antidots (Fig. 4.22).

4.2.4. Dynamics measurements

Dynamics properties of magnetic nanostructures are gaining attention due to their potential role for the development of high density storage devices. The effect of geometry on quantization of spin waves in small structures when the feature size becomes comparable to the wavelength of the spin waves has been addressed in this section by employing conventional X-band FMR, and BLS spectroscopy.

4.2.4.1. FMR study

FMR study was carried out by employing conventional FMR setup at 9.4 GHz at room temperature. The FMR results for Theta_Py10_3 are summarized in Fig 4.33. The results from the patterned geometry are compared with the result from uniform film (reference sample). One can see that in the case of reference sample (uniform film), we have observed single line corresponds to uniform resonance mode. The resonant microwave absorption of 10nm Py film occurs at a magnetic field of 102 mT and rotation of sample in the plane

parallel to external magnetic field did not show any significant changes in the resonance line confirming that sample has negligible in-plane anisotropy (also confirmed from LMOKE analysis). In the case of basic square ADL (Theta_Py10_3), Fig. 4.33 (a) shows the spectra for different in-plane angles. To explain these angular dependences we split our discussion

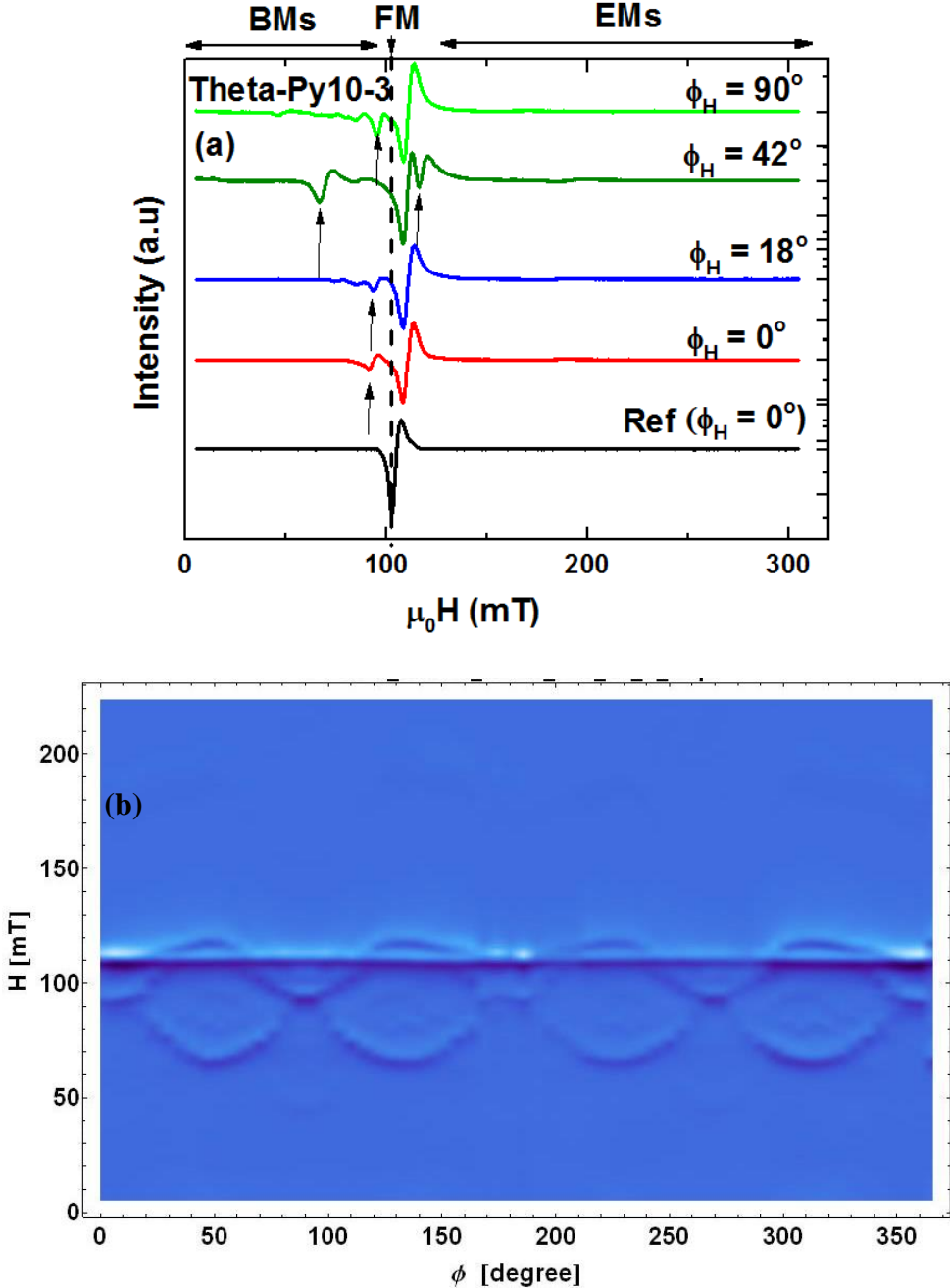


Figure 4.33: FMR spectra for different in-plane angles: (a) Theta_Py10_3, (b) 2D plots of observed resonance modes as function of in-plane angle.

into three parts: firstly we will describe angular dependence of the most intensive SW

excitation, i.e., fundamental mode (FM), secondly then the bulk SW excitations (BMs) and finally SW excitations at high resonance fields (edge modes (EMs)).

The bulk SWs are observed in fields lower than the main resonance line. The small amplitude excitations observed at fields larger than FM field are attributed to the SW localized at the edge of the antidots, i.e., edge modes (EM) as will be further discussed later.

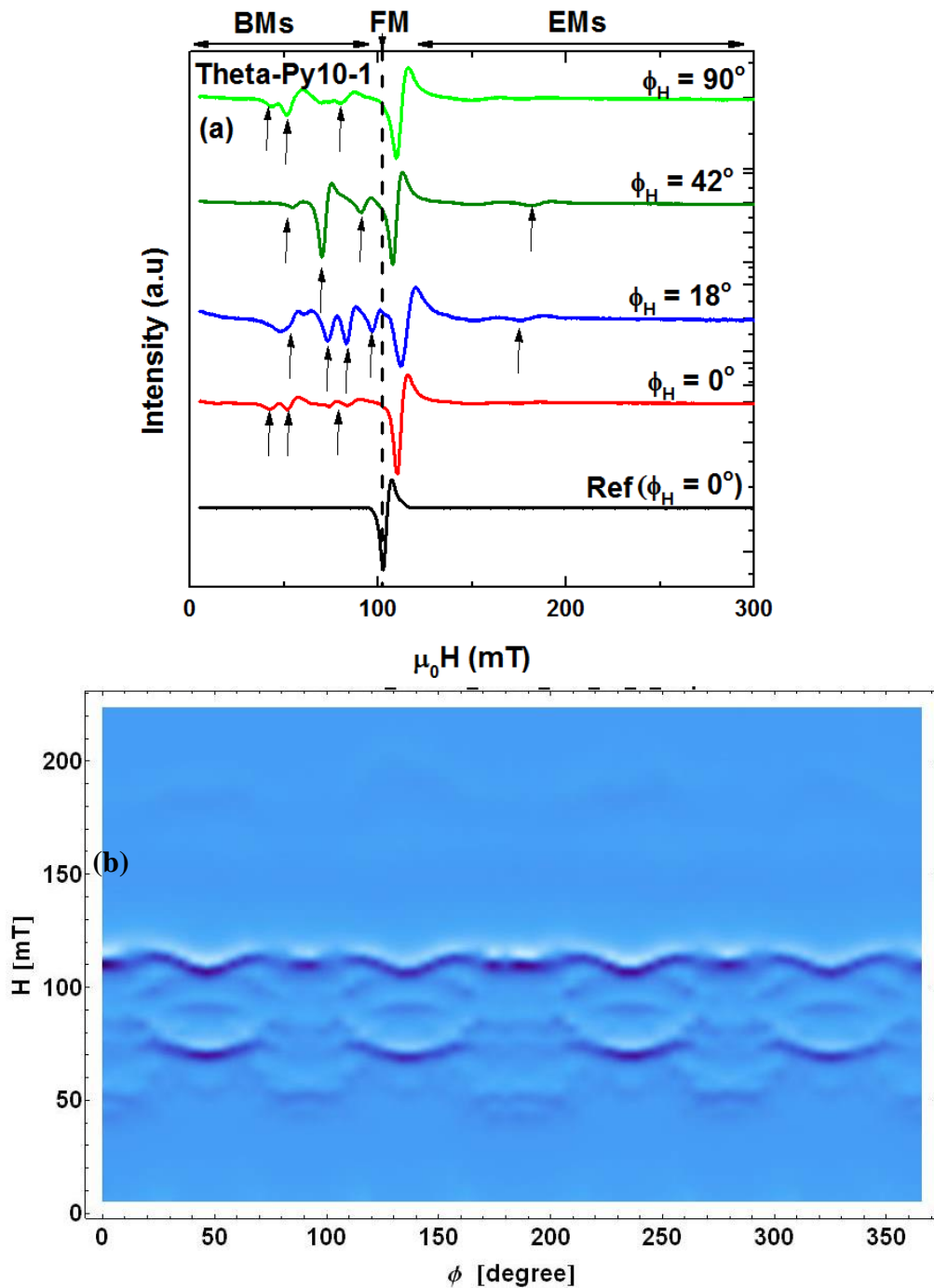


Figure 4.34. FMR spectra for different in-plane angles: (a) Theta_Py10_1, (b) 2D plots of observed resonance modes as function of in-plane angle.

For applied field parallel along the sides of the square ADL, additional resonance lines in the low field regime can be seen while for applied field for inplane angles of around 30-50° additional resonance line around 115 mT can be clearly seen, Fig. 4.33(a).

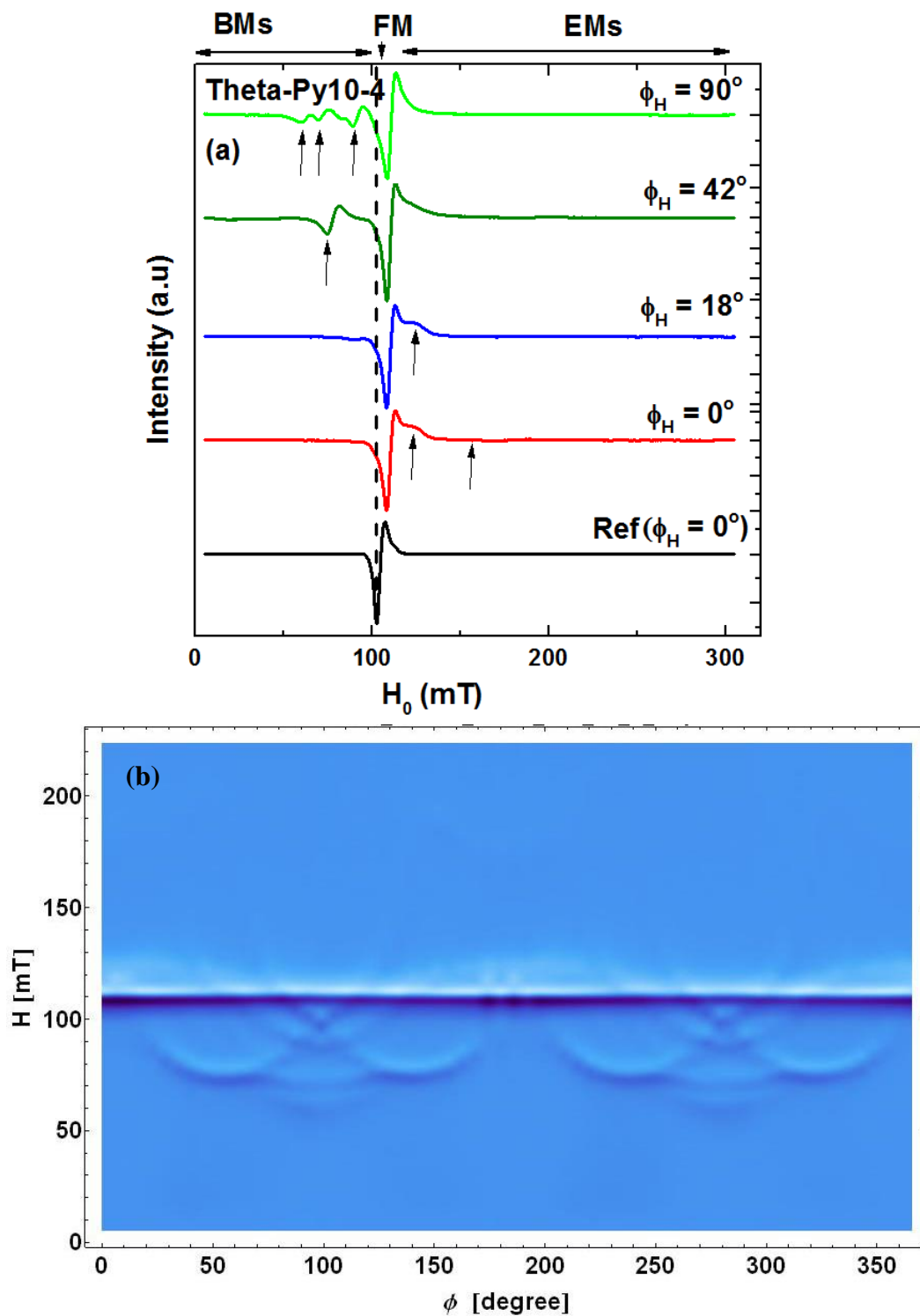


Figure 4.35 FMR spectra for different in-plane angles: (a) Theta_Py10_4, (b) 2D plots of observed resonance modes as function of in-plane angle.

Figure 4.33(b) shows the complete 2D plots of the observed resonance modes for basic square ADL where presence of four-fold symmetry confirm our LOMOE results. One can also see the strong resonance line with no in-plane dependence (from the un-patterned region of the sample, as the patterned sample is located inside the collar of un-patterned region). Similar effect of collar/ area which surrounds the patterned region has also been observed in Ref. [Gon15]. The resonance peak for patterned samples occurs at slightly higher magnetic field in comparison to the reference sample due to the demagnetizing effects [Jun02].

Figure 4.34 summarized the FMR results for the sample with additional antidot in the basic square unit cell. A change of the in-plane direction of the external field leads to a drastic change of the ferromagnetic resonance spectra. For an in-field angle of $\phi_H = 0^\circ$ (Fig. 4.34 (a)), the most intensive lines are observed around lower field values 42, 51, and 78 mT while in the case of square lattice additional resonance line was observed around 90 mT. For in-field angle of $\phi_H = 18^\circ$, several resonance peaks below uniform resonance line are observed at magnetic field values of 75, 72, 83, and 96 mT. Furthermore it has also been observed that there are couples of additional resonance lines in the high magnetic field regime appeared around 150, and 175 mT. For $\phi_H = 42^\circ$ which is along the diagonal of the square (Fig. 4.22), main resonance lines in the low magnetic field regime appear around 51, 70, and 90 mT. The additional resonance peaks in the high field regime are also observed around 150, and 180 mT. While being a geometric configuration resonance peaks at $\phi_H = 90^\circ$ are almost same as $\phi_H = 0^\circ$. The oscillation of uniform resonance mode appearance could be connected to the dipolar interaction between different antidots [Jun02]. The resonance peaks in the low and high magnetic field regime will be discussed later in details.

Figure 4.35 shows the summary of the FMR results for the more complex system (wave-like) patterns. $\phi_H = 0^\circ$ defines the angle in which field is applied perpendicular to the wave-like patterns. One can see that more intense resonance peak is hybridized with fundamental mode (uniform mode). Additionally a weak resonance line in high magnetic field regime is also observed around 170 mT. This resonance is closer to the resonance observed for Theta_Py10_3 and can be attributed due to the larger antidots. For $\phi_H = 42^\circ$, additional resonance peak around 74 mT is observed. This peak is much similar to the observed for square ADL (Fig. 4.33 (a)). While in the case of $\phi_H = 90^\circ$ when field is along the wave-like patterns (perpendicular in LMOKE configuration), intense FMR spectra in the low magnetic

field regime is observed with resonance peaks around 60, 70, and 90 mT. If ones compares with Fig. 4.33 (a), and 4.34 (b), we can infer that in wave-like patterns the observed resonance lines are combination from smaller and larger antidots. The observed resonance lines can be classified into three categories:

Fundamental mode (FM): FM is the SW excitation with the largest FMR intensity in the spectra. We can see in Fig. 4.33(a), and Fig. 4.35(b) that the FM does not change its field position or damping with rotating direction of the magnetic field. However, the variation of the FM field position with ϕ_H is observed in Theta_Py10_1 (Fig. 4.34). This can be possibly due to the interaction of FM excitation due to the larger antidots and smaller antidots. We have noticed that this dependence on ϕ_H is not monotonous in the range between 0 and 42 degree.

Bulk modes (BMs): For modes with the resonance fields lower than FM the most pronounced dependences on the magnetic field orientation are observed in all three samples. In Theta_Py10_3 for various in-plane angles we can separate two resonances lines, one at smaller angles ($\phi_H < 20$ degree) and for large angles another bulk excitation becomes intensive around 67mT. For both of them the variation of its magnetic field position with the change of the magnetic field orientation is observed.

In Theta_Py10_1, the strong variations of the bulk excitations are observed. The plenty of BM excited at intermediated frequencies and two pronounced lines for $\phi_H = 45^\circ$. For this angle, the applied field is parallel to the side of the square lattice which is almost at the same resonance line as it was observed in Theta_Py10_3 mostly probably due to the larger antidots. Additional low intensity resonance line below this resonance line could be connected due to the smaller antidot.

In wave-like patterns sample (Theta_Py10_4) it has been observed that at smaller in-plane angles ($\phi_H < 40^\circ$) the BM are not visible in FMR measurements. . For $\phi_H = 42^\circ$, additional resonance peak around 74 mT is observed. This peak is much similar to the observed for square ADL (Fig. 4.33(a)). While in the case of $\phi_H = 90^\circ$ when field is along the wave-like patterns (perpendicular in LMOKE configuration), intense FMR spectra in the low magnetic field regime is observed with resonance peaks around 60, 70, and 90 mT. If ones compares with Figure 4.33 (a), and 4.34 (b), we can infer that in wave-like patterns the observed resonance lines are due to the combined effect from smaller and larger antidots.

Edge modes (EMs): It is widely accepted that many properties of the material are determined by the surface, and interface. Similarly edges of patterned magnetic thin film are expected to play an important role in the magnetic behavior of patterned elements because of the exchange and dipole-dipole interaction [McM06]. Their intensity in the measured FMR spectra is much lower than the intensity of the fundamental uniform mode, thus they are hardly visible in Fig. 4.33 (a), Fig. 4.34 (b), and Fig. 4.35 (b). In Fig.4.36 we have magnified the FMR spectra to see the effect of shape of the nanostructures on these EMs.

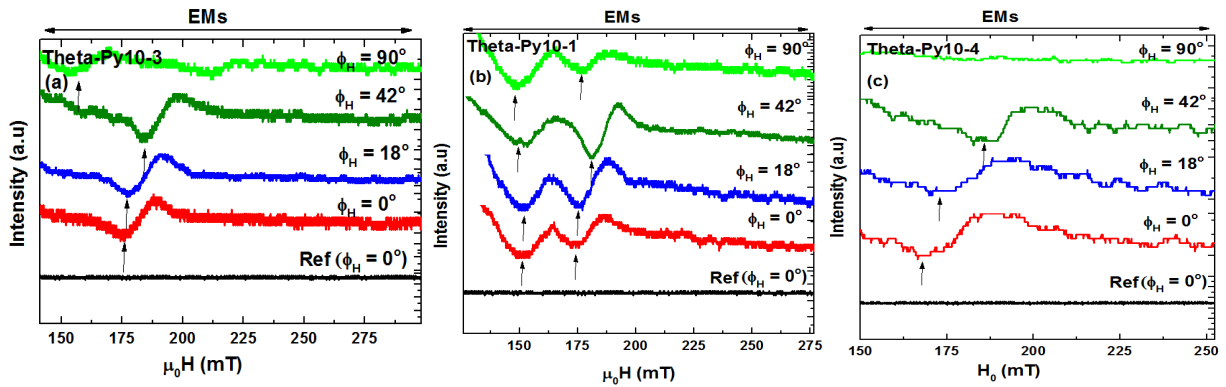


Figure 4.36. Magnified FMR spectra in high field regime for different in-plane angles: (a) Theta_Py10_3, (b) Theta_Py10_1, and (c) Theta_Py10_4.

Figure 4.36 shows the magnified FMR spectra in the high field regime for three different samples. For the Theta_Py10_3, only single EM is visible in Fig. 4.36(a), while for Theta_Py10_1, two EMs are visible. In Theta_Py10_3 with change of the in-field angle ϕ_H from 0 to 45° the resonance field of EM increases. We can suppose that this is the effect of the static demagnetizing field from the neighboring antidots, because with increasing ϕ_H the distance between antidots decreases (for ϕ_H from 0 to 45° edge to edge separation decreases from approximately 448 to 200 nm). The demagnetizing field value increases which pushes the resonance field of the SW excitations to lower values (because the demagnetizing field is oriented according with the external field). However, this is opposite to the observation from Fig. 4.36. Thus other mechanism needs to be considered. When we look for the spectra of Theta_Py_3 taken at 90° , and compare it with 0° , we can see significant difference – i.e., the EM in the former is at lower resonance field than for 0° (Fig. 4.36 (a)). In the ideal array of circular antidots, these two spectra should have identical spectra. The existent difference points at non circular shape of antidots, which is also visible in the SEM images shown in Fig. 4.22 (a), and LMOKE results (Fig. 4.26). The lower resonance field at $\phi_H = 90^\circ$ can indicate sharp corner (This assumption needs further verification).

Two EM are clearly revealed for Theta_Py10_1 (Fig. 4.36). The agreement between $\phi_H = 0$ and 90° points that in this square lattice sample have regular arrays rather than elliptical-like circular antidots. The resonances at higher fields (around 174, 175 and 181 mT for $\phi_H = 0^\circ, 18^\circ$ and 44° respectively) we can attribute to the EM of the larger antidots, as similar dependences are observed for Theta_Py10_3 (Fig. 4.36 (a)) with resonance lines around 176, 178, 184 for $\phi_H = 0^\circ, 18^\circ$ and 44° respectively. A slight increase in resonance lines can be attributed due to the dipolar interaction between different antidots. The additional resonance line can also be seen below the above discussed EM. This SW is most probably connected with smaller antidots, as it is not observed in Theta_Py10_3. Its resonance field is almost independent on the field orientation, which can suggest that observed excitation have more uniform profile.

For wave-like patterns Theta_Py10_4 sample, the high field regime is very similar to the Theta_Py10_3, where resonance lines around 168, 174, 186 mT for $\phi_H = 0^\circ, 18^\circ$ and 44° are respectively observed. A deeper look of Fig. 4.34 (a) shows that additional mode at 42° at slightly higher magnetic field than the FM which describe its nature as EM or its origin in the backward spin waves known from the homogeneous thin film. We will come back to this issue during discussion of the micromagnetic simulation results.

The experimental results are further verified through the micromagnetic simulation by using MuMax [Van11]. For uniform antidots (square lattice) the radius of the antidot was selected 400 nm comparable to the SEM analysis (Table 4.2) while the lattice constant (period p) was set to 650 nm, number of cells was 256 so cell size and grid is about 2.5 nm. Periodic boundary conditions with 8 times repetitions along with built-in function edge smooth to overcome staircase effects were selected. $M_s = 860 \text{ kAm}^{-1}$, exchange constant $A = 13 \times 10^{-12} \text{ Jm}^{-1}$, Damping constant 0.001, Max excitation field $5.413 \times 10^{-2} \text{ T}$ (in sin function), Max frequency $f = 45 \times 10^9 \text{ Hz}$. Simulation time is about 25 ns. For all simulations the above parameters were kept constant except change in cell size and for the wave like patterns it is 1.78nm.

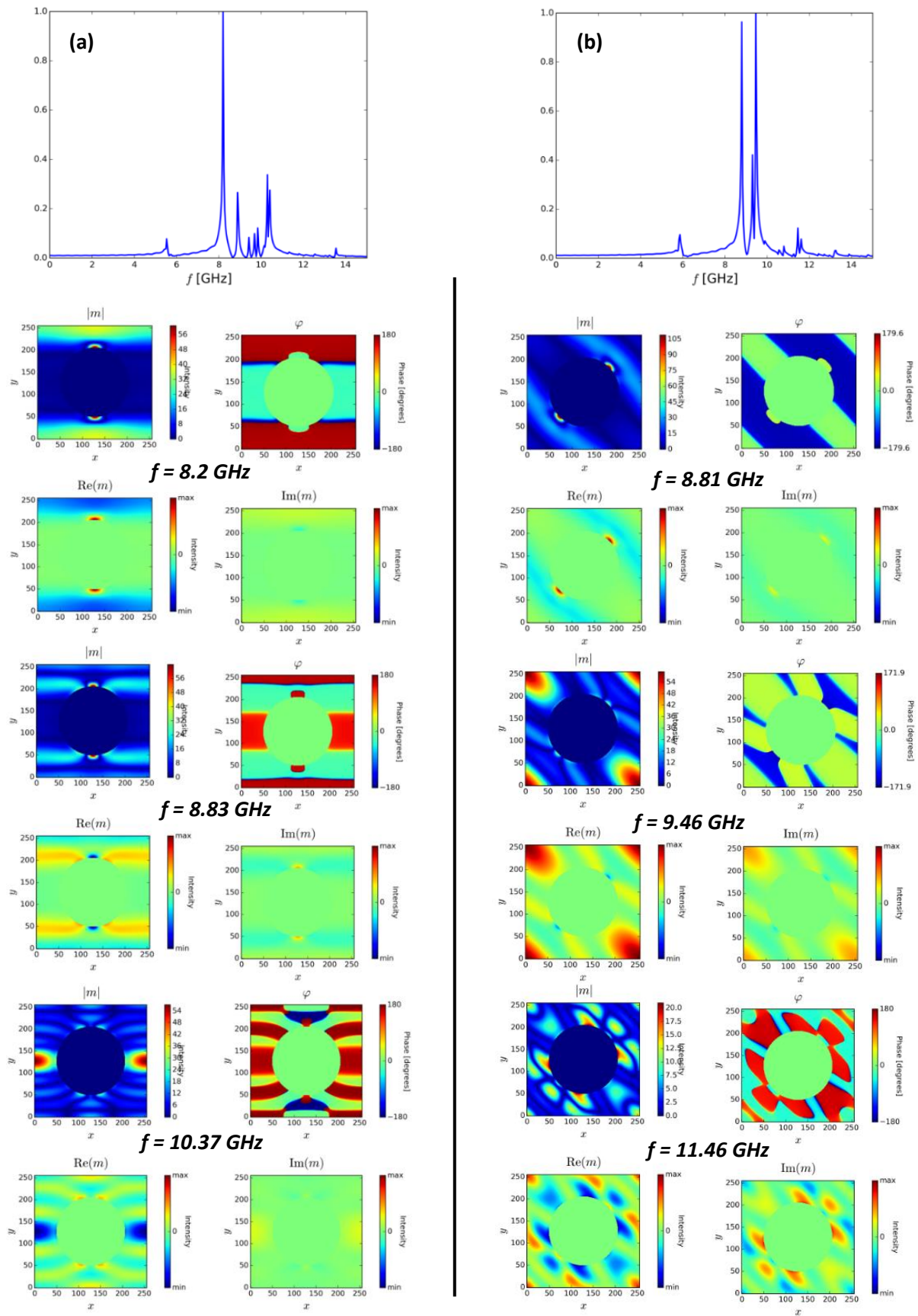


Figure 4. 37. Calculated spectra in frequency domains for (a) $\phi_H = 0^\circ$ and (b) $\phi_H = 44^\circ$ for sample Theta_Py10_3.

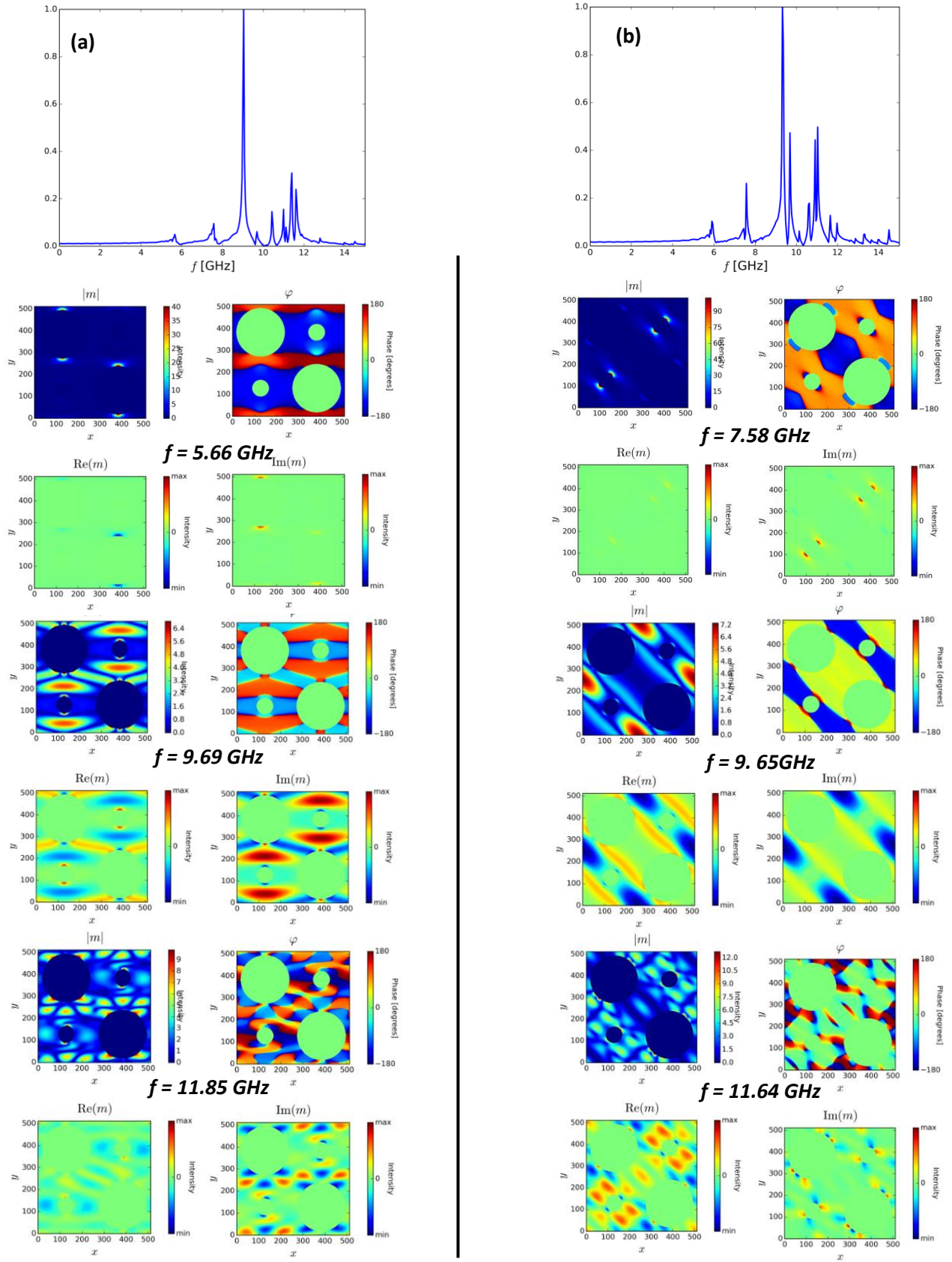


Figure 4. 38. Calculated spectra in frequency domains exemplary observed spin wave modes for (a) $\phi_H = 0^\circ$ and (b) $\phi_H = 44^\circ$ for sample Theta_Py10_1.

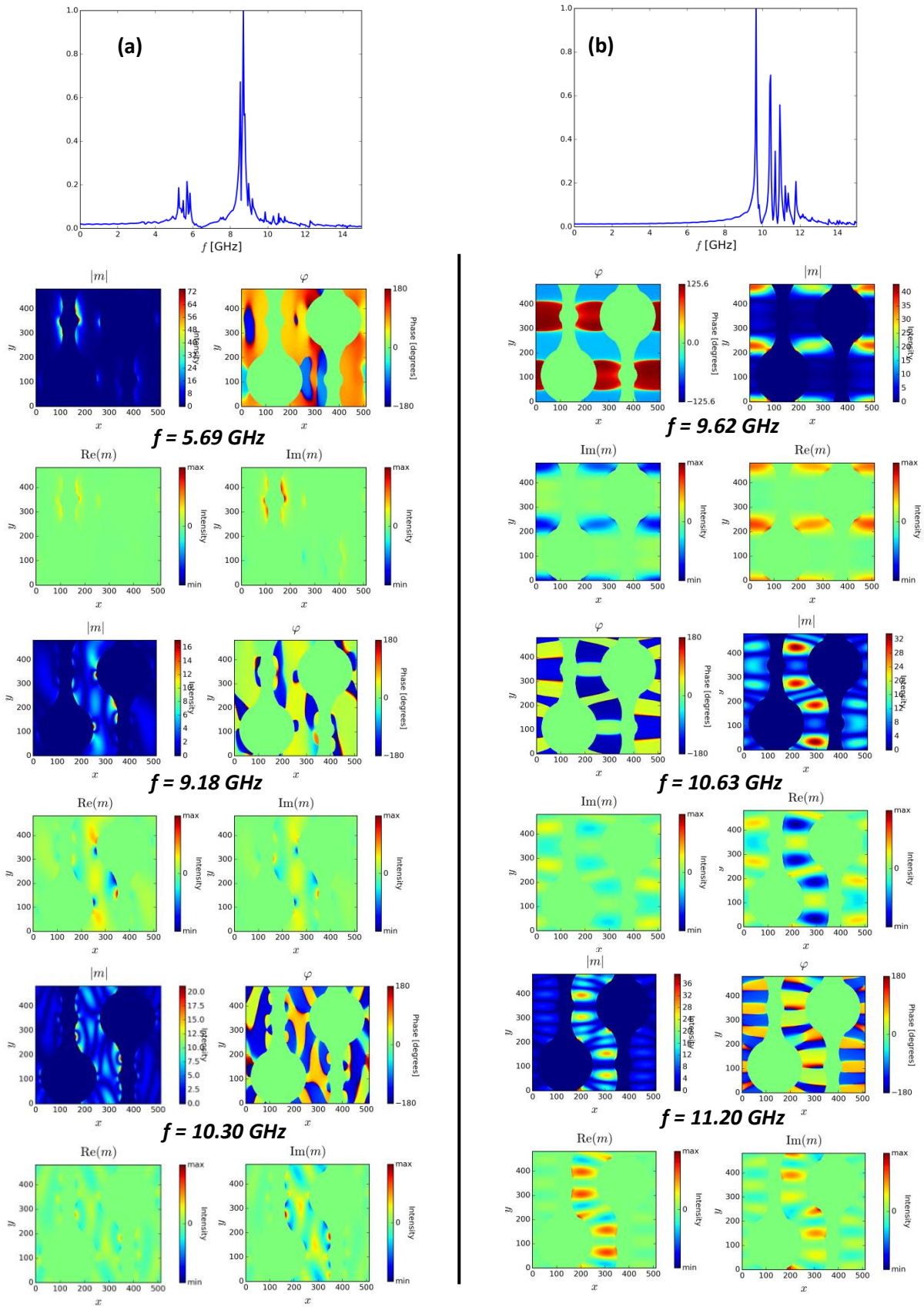


Figure 4.39 Calculated spectra in frequency domains and exemplary observed spin wave modes for (a) $\phi_H = 0^\circ$ and (b) $\phi_H = 87^\circ$ for sample Theta_Py10_4.

Figure 4.37, Fig. 4.38, and Fig. 4.39 shows the calculated frequency spectra and exemplary spin waves modes for certain frequencies for samples Theta_Py10_3, Theta_Py10_1, and Theta_Py10_4 respectively. In addition to the large corresponding to the fundamental mode, satellite peaks are also observed on both sides of the FM, similar to the observed in experimentally. The quantitative discrepancy in position of the peaks to the experimental data could be related with the exact shape of the antidots since they are very sensitive to the exact values of the parameters used in the calculations. However qualitatively the calculated results, Fig. 4.40 are in very good agreement with the experimental results already shown in Fig. 4.33 (b), 4.43 (b), and 4.35 (b) for Theta_Py10_3, Theta_Py10_1, and Theta_Py10_4 respectively.

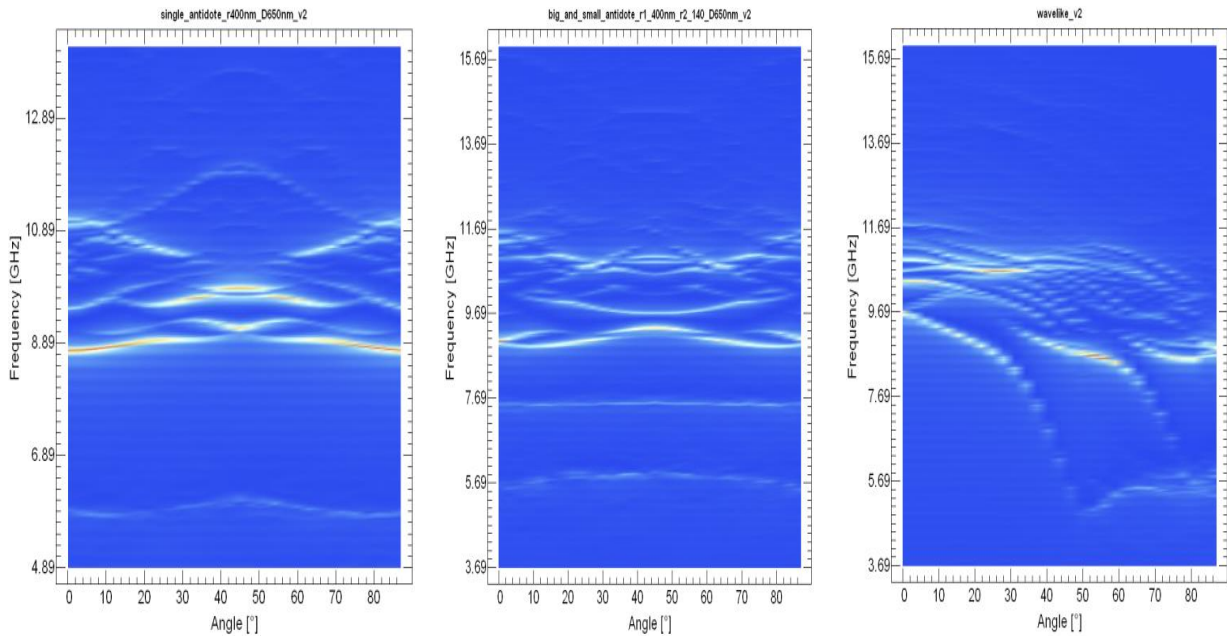


Figure 4.40 Calculated frequency spectra for different in-plane angles (ϕ_H)_2D plot for (a) Theta_Py10_3, (b) Theta_Py10_1, and (c) Theta_Py10_4.

When the magnetization is saturated along the diagonal of the square ADL (longer distance between two antidots), the majority of the magnetic film area will be subjected to have an additional internal field opposite to the external field, which will cause this area to resonate at a higher applied field. The resonance frequencies ($\sim 10.5\text{GHz}$ and $\sim 12\text{GHz}$) around $\phi_H = 44^\circ$ orthogonal to each other with almost identical oscillatory amplitude. Such resonance can be from uncoupled resonances emanating from different parts of the sample defined by the local dipolar field [Yu03]. Figure 4.40 (a) shows the 2D plots of calculated frequencies clearly shows that square ADL have four fold symmetry and in agreement with the literature [Yu03, Mar07]. One low lying frequency mode can be seen in the FFT plot around 5.9 GHz

and qualitatively agree with experimental FMR data where one resonance mode at high magnetic field regime was observed. One can see that with addition of antidot inside the square ADL leads to the drastic change in calculated spectra, Fig. 4.39 (b). One additional resonance line around 7.69 GHz (high magnetic field regime in FMR) appears which was absent in the case of Fig. 4.40 (b). For magnetic field applied parallel to the sides of the ADL square leads to the couple of low lying frequencies modes (high magnetic regime in FMR). This data is qualitatively agreed with the experimental data where one can see several resonance lines in the high magnetic field regime when the field is along the sides of the ADL square. FFT spectra Fig. 4.37 (a) shows several frequencies in the above the FM (low magnetic field regime in FMR). Similarly experimental we have observed several resonant lines in the low magnetic field regime. After comparison of calculated FFT spectra for $\phi_H = 44^\circ$, we can conclude that resonance mode around 11.64 GHz gets intensive as compared to the $\phi_H = 0^\circ$ which suggest dipolar interaction between different holes are playing role. There is one more pronounced feature that low frequency mode around 7.58 GHz is more pronounced and could be related to the edge modes as it can also be seen from power and phase images of this mode.

In the complex geometry wave-like patterns, Theta_Py10_4, the calculated FFT spectrum along with exemplary frequencies are summarized in Fig. 4.39. One can see few frequencies modes on both side of the FM, especially when the field is perpendicular to the wave-like patterns, low lying frequency mode is observed (Fig. 4.39(a)) which is absent in the case when the field is applied parallel to the wave-like patterns (Fig. 4.39 (b)). This is also consistent with the FMR experimental data where one resonance line in the high magnetic field regime was observed when the field is perpendicular to the wave-like patterns (Fig. 4.36 (c)). This mode could be assigned as EM because of difference in demagnetizing field due to the different values of nonmagnetic materials (holes). When the field is applied parallel to the wave-like patterns few well defined frequencies modes are visible connected to the uniform distribution of magnetization along the wave-like patterns and can be named as BMs.

Summary

The observed increase in H_c after patterning was similar for all studied three geometries. From the in-plane dependence of H_c we can conclude that ADL induces an in-plane anisotropy. The induced easy and hard axes become the directions along which the antidots

are furthest apart and closest to each other respectively. The two step-hysteresis loop from LMOKE measurements from ADL with additional antidot inside the square ADL, suggests two steps reversal process. The magnetic domains are pinned around the smaller antidots and they require larger reversal field to switch which is visible also from LMOKE hysteresis. With the addition of hole/holes (antidot/antidots), the contribution of the surface energy becomes larger and blade-like magnetic domains formation appeared. The sudden jump in magnetization can be connected to the switching of the domains around the narrower regions. The dynamics study from FMR confirms the in-plane magnetic anisotropies observed from LMOKE measurements. Addition of antidot inside the square ADL leads to the additional resonances lines both in the high and low magnetic field regime. With the help of micromagnetic simulations, we have sorted out different excitations modes such as FM, bulk and edge modes. The quantitative discrepancy in position of the peaks to the experimental data could be related with the exact shape of the antidots since they are very sensitive to the exact values of the parameters used in the calculations, however qualitatively results are in good agreement with the experimental results.

4.3. Thin films of Pt/Co/Pt

4.3.1. Sample fabrication:

Epitaxial films were grown by MBE system under a base pressure of 10^{-10} Torr. The deposition process was monitored in-situ by reflection high-energy electron diffraction (RHEED) and Auger electron spectroscopy (AES). A 20-nm-thick Mo(110) buffer layer was first grown at 1000 °C on an epitaxially sapphire $\text{Al}_2\text{O}_3(11\bar{2}0)$ substrate ($8 \times 10 \text{ mm}^2$ in lateral size). It was followed by subsequent room temperature deposition of (i) a 20-nm-thick Pt(111) underlayer, (ii) a Co(0001) magnetic layer 3.3 nm, and (iii) a 5-nm-thick Pt(111) cover layer (see Fig. 4.41). Multi-irradiated stripes ($8 \times 0.9 \text{ mm}^2$) were fabricated by using Ga^+ ions with energy $E = 30 \text{ keV}$. Irradiation dose range covers both first and second out-of-plane magnetization states as described already in the previous literature [Maz12]. The scheme of the sample fabrication is shown in Fig. 4.41. The fluences used to modify the samples are mentioned in the table 4.3.

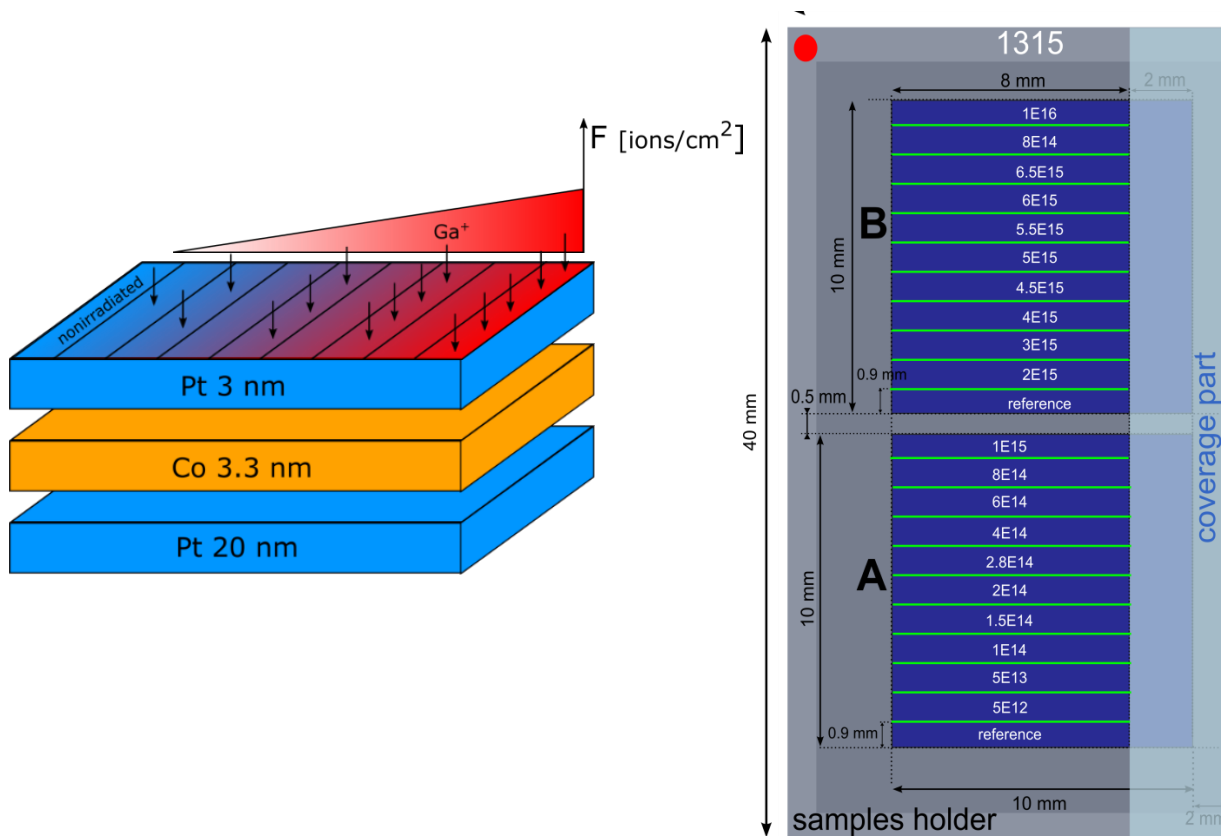


Figure 4.41: Schematic diagram for sample irradiation process

Table 4.3: Fluence Vs log of Fluence

Fluence (F)	Log F
5.00E+12	1.27E+01
5.00E+13	1.37E+01
1.00E+14	1.40E+01
1.50E+14	1.42E+01
2.00E+14	1.43E+01
2.80E+14	1.44E+01
4.00E+14	1.46E+01
6.00E+14	1.48E+01
8.00E+14	1.49E+01
1.00E+15	1.50E+01
2.00E+15	1.53E+01
3.00E+15	1.55E+01
4.00E+15	1.56E+01
4.50E+15	1.57E+01
5.00E+15	1.57E+01
5.50E+15	1.57E+01
6.00E+15	1.58E+01
6.50E+15	1.58E+01
8.00E+15	1.59E+01
1.00E+16	1.60E+01

4.3.2. Statics measurements

4.3.2.1. PMOKE measurements

Results of remanence images obtained in PMOKE configuration are shown in Fig. 4.42. The details of the experimental setup can be found in the experimental section (3.2.2). From these images it is clearly visible that two branches with out-of-plane magnetization are present for particular fluences. For branch1 fluence (F) = 2.8×10^{14} ions/cm² and for branch 2, fluence (F) = 5×10^{15} ions/cm². This is confirmed by PMOKE hysteresis loop measurements performed on non-irradiated region (reference) shown in Fig. 4.43.

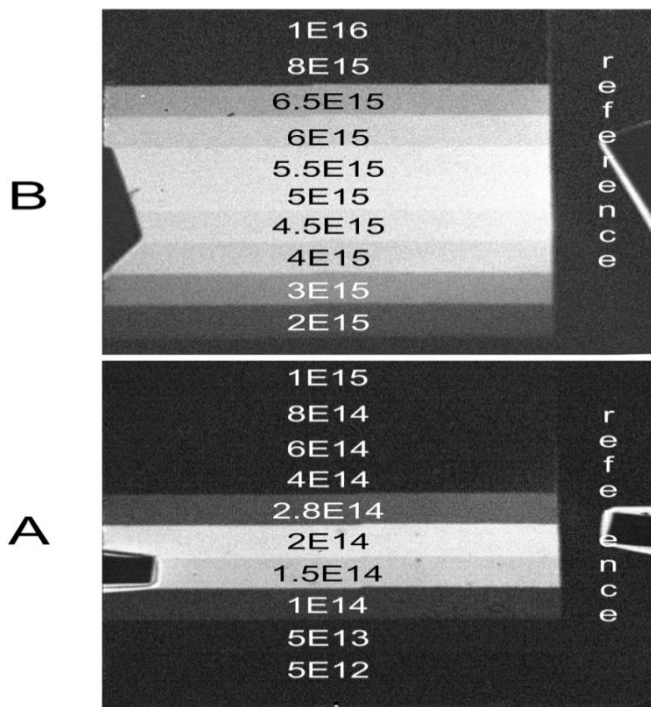


Figure. 4.42: Remnant image of samples A and B. The image was taken at field $H_{\perp} = \pm 4\text{KOe}$

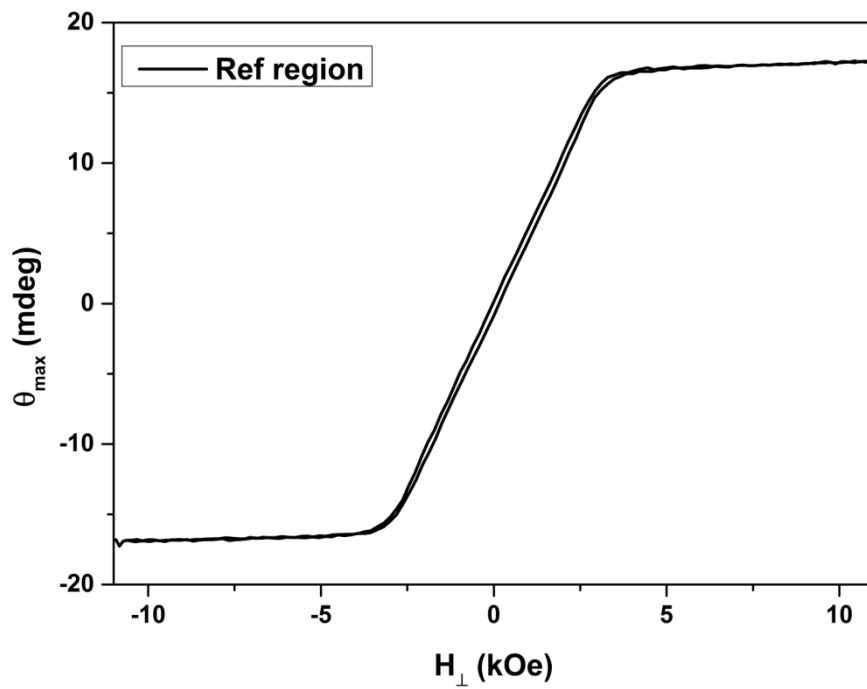


Figure. 4.43: Hysteresis loops measured in PMOKE configuration on reference region (non-irradiated area).

Exemplary hysteresis loops for selected irradiated fluence are shown in the following:

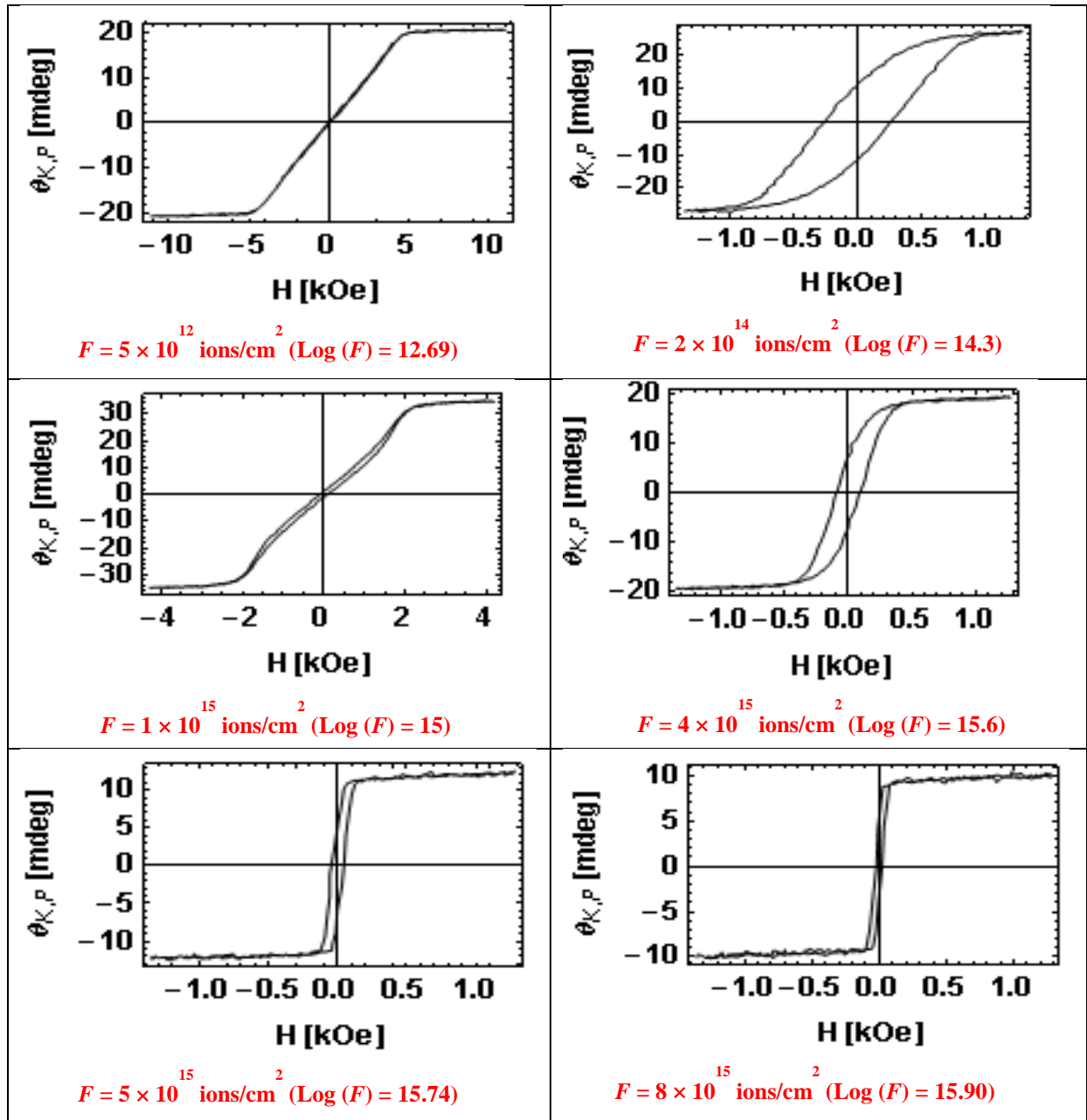


Figure. 4.44: Hysteresis loops at selected fluences (mentioned in the each figure) are shown. One can see the evolution of hysteresis (square-like hysteresis) shows the creation of out-of- plane magnetization state.

Magnetic parameters calculated from PMOKE measurements are shown in the following:

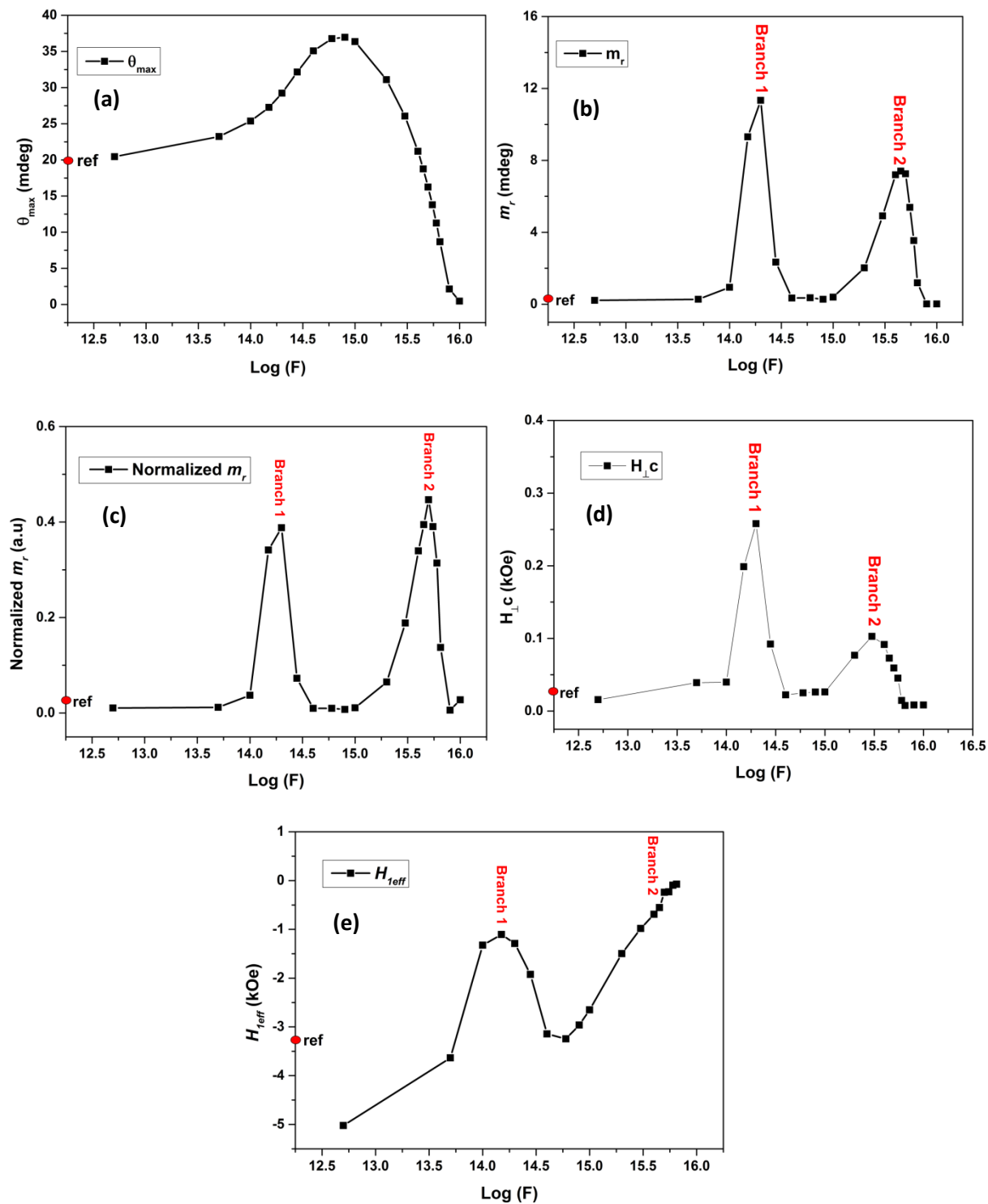


Figure 4.45: Estimated magneto-optical and magnetic parameter: a) maximum Kerr rotation; b) remanence; c) normalized remanence; d) coercivity; e) effective anisotropy field $H_{1\text{eff}}$. Red points on the vertical axis corresponds to the values for the non-irradiated sample (reference)

One can see the F -dependent magnetization behavior in Fig. 4.45. One can see that branches 1 (1st out of plane magnetization state) and 2 (2nd out of plane magnetization state) (Fig. 4.51 (b-e)) are found for fluence ($F1$) $\approx 2.5 \times 10^{14}$ ions/cm² and fluence ($F2$) $\approx 5.2 \times 10^{15}$ ions/cm², respectively. Moreover, as depicted in Fig. 4.45(a), the polar Kerr rotation value substantially increases under ion irradiation. When F increases up to 3.1×10^{14} ions/cm², the magnetization rotates first from an easy-plane to an out-of-plane orientation. At higher fluence, $F = 9.3 \times 10^{14}$ ions/cm², magnetization falls back again into the film plane. Surprisingly, a further increase of the fluence, up to 4.6×10^{15} ions/cm², induces again a reorientation of the magnetization towards the out-of-plane direction. Finally, for $F > 7 \times 10^{15}$ ions/cm², the irradiated sample becomes superparamagnetic.

4.3.2.2. LMOKE measurements

The LMOKE measurements were carried out by employing laser of wavelength 532nm. The details of the experimental setup are described in the experimental section (3.2.2).

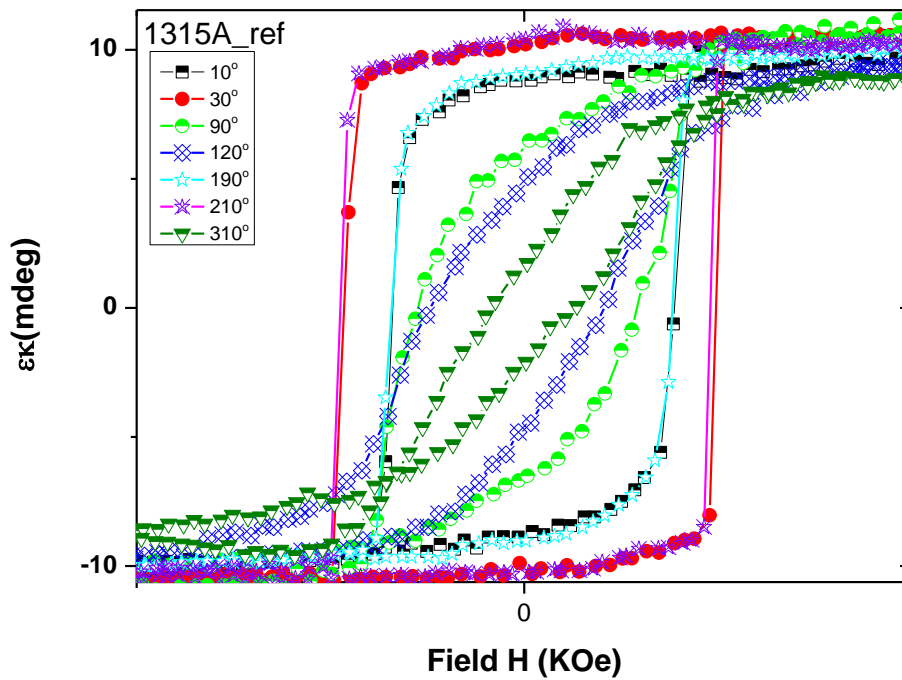


Figure. 4.46: Exemplary hysteresis loops (Hysteresis loops taken at applied magnetic field 1 KOe) for different in-plane angles. One can clearly see the anisotropy.

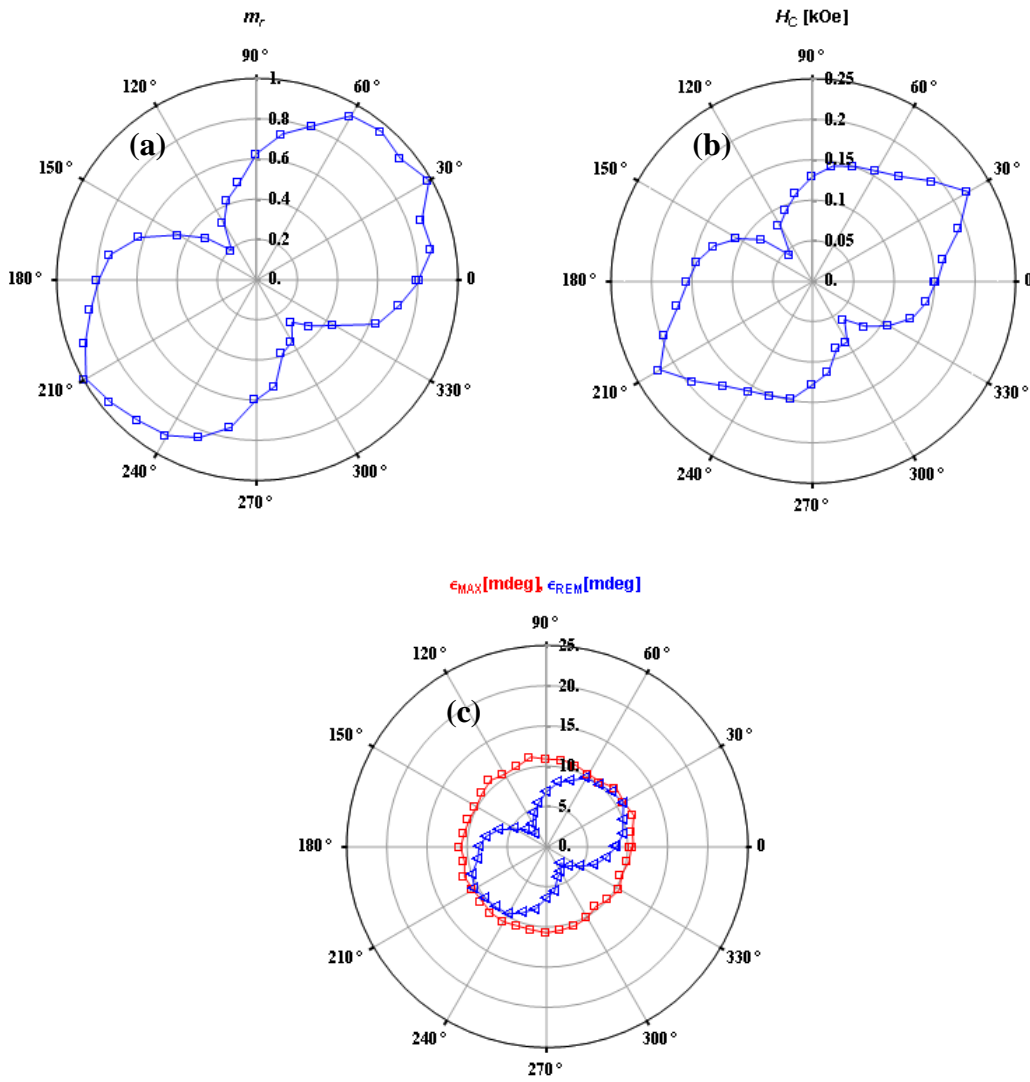


Figure. 4.47: Angular dependence of (a) Kerr rotation, (b) remanent magnetization, and (c) coercivity.

4.3.3. Dynamics measurements

The effect of Ga^+ irradiation on dynamics of magnetization has been carried out by BLS spectroscopy in backscattering geometry. For single thin magnetic Fe or Co layers of thickness d typically smaller than $\approx 30 \text{ \AA}$ the only spin wave mode accessible in BLS scattering experiment ($\omega/2\pi \leq 100 \text{ GHz}$) is the dipolar type, so called Damon-Eshbach (DE) mode [Dam61]. This mode exists if an external field is applied parallel to the film surface (perpendicular to the scattering geometry) as shown in Fig. 3.19. The DE mode is a surface mode, i.e., the mode energy is localized near the film surface and precession amplitude decays perpendicular to the film with a decay length of the order of $2\pi/q_{\parallel}$, which is in the range of

$\approx 3000 \text{ \AA}$ in a BLS scattering experiment [Hil00]. By neglecting anisotropies and the weak exchange contribution, the mode frequency for propagation perpendicular to the applied field is described as follows [Hil00]:

$$\left(\frac{\omega}{\gamma}\right)^2 = H(H + 4\pi M_s) + (2\pi M_s)^2(1 - e^{-2q_{\parallel}d}) \quad (4.3.1)$$

Where $\omega = 2\pi f$ is frequency, H is applied external field, M_s is saturation magnetization, q_{\parallel} is transferred q -vector, and d is the film thickness.

After simplify above equation becomes:

$$\left(\frac{\omega}{\gamma}\right)^2 = \left[\frac{1}{M_s} \frac{\partial^2 E_{an}}{\partial^2 \theta} + 4\pi M_s \left(1 - \frac{1}{2} q_{\parallel} \cdot d\right) + H \right] \cdot \left[(K_U \sin^2 \theta) (4\pi M_s \cdot \frac{1}{2} q \cdot d + H) \right] \quad (4.3.2)$$

The effective anisotropy field can be calculated as [Hil99]:

$$H_{1eff} = \frac{-\left(\frac{\omega}{\gamma}\right)^2 + H^2}{H + 2\pi M_s q_{\parallel} d} \quad (4.3.3)$$

Where $\omega = 2\pi f$ f is observed frequency, M_s - saturation magnetization, H - external applied field, d - thickness of sample, q_{\parallel} - wave-vector and defined already in Fig. 3.19.

All BLS measurements were performed by employing experimental setup described in 3.3.2. A static magnetic field was applied in the film-plane perpendicular to the transferred wave vector scattering plane, i.e. in the Damon-Eshbach (DE) geometry. The measurements were performed for various magnetic field values and at different angles of incidence of the probing light beam, *i.e.* the angle between the direction of the incident laser beam and the film normal θ , as shown in Fig. 3.19.

In all BLS measurements single spin wave excitation known as DE mode was observed which

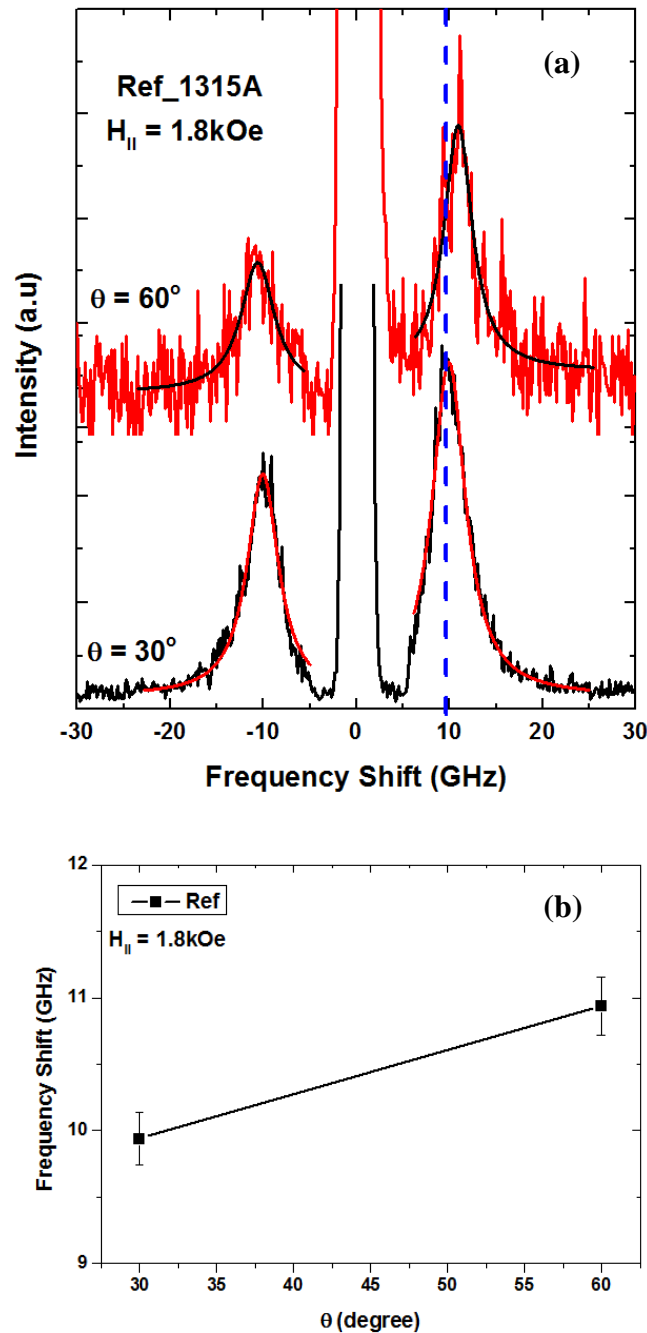


Figure. 4.48: (a) BLS spectra for from reference region for scattering angles of $\theta = 30^\circ$, and 60° . (b) Dependence of observed spin wave excitation on scattering angle.

showed dispersion characteristics on scattering angle. BLS spectra from reference region for scattering angles θ of 30° and 60° are shown in Fig. 4.48 (a). The difference in signal (for $\theta = 30^\circ$ and 60°) is due to the different accumulation times (~ 11 hrs for $\theta = 30^\circ$). Frequency of excitation mode was calculated through fitting of experimental spectrum by lorentzian function

with (f-) and (f+) frequencies corresponds to stoke and antistoke modes, respectively One can see that there is shift in frequency towards high frequency side with increase in incident angles, Fig. 4.48(b).

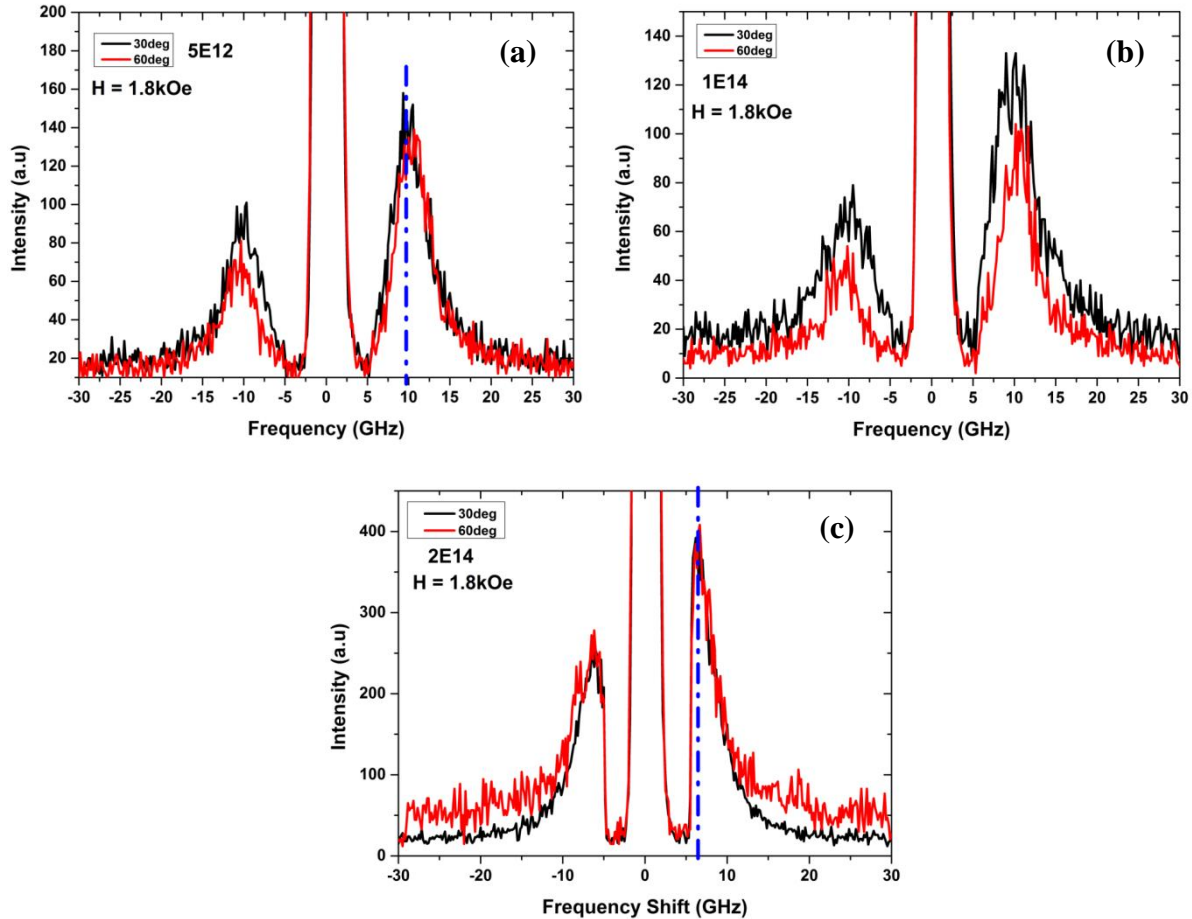


Figure. 4.49: (a) BLS spectra for scattering angles $\theta = 30^\circ$, and 60° . (a) fluence 5E12 (b) fluence 1E14, and (c) fluence 2E14.

The main objective of the presented research was to explore the effect of fluence on the spin wave excitations, so scattering angle and applied magnetic field ($\theta = 30^\circ$, $H = 1.18$ kOe respectively) were kept constant in all measurements.

Figure 4.49 shows the BLS spectra for different fluences: (a) = 5E12-inplane magnetization state, (b) 1E14-close to the out of plane-magnetization branch1, and (c) 2E14-out-of-plane magnetization branch1 (see remanent image Fig.4.42). There is a increase in the observed spin wave excitation mode with the incident angle confirming DE mode behavior. Figure 4.50 shows the dependence of observed spin wave excitation as a function of log of fluence ($\log(F)$). One can see that there that with the increase in the fluence there is a decrease in the

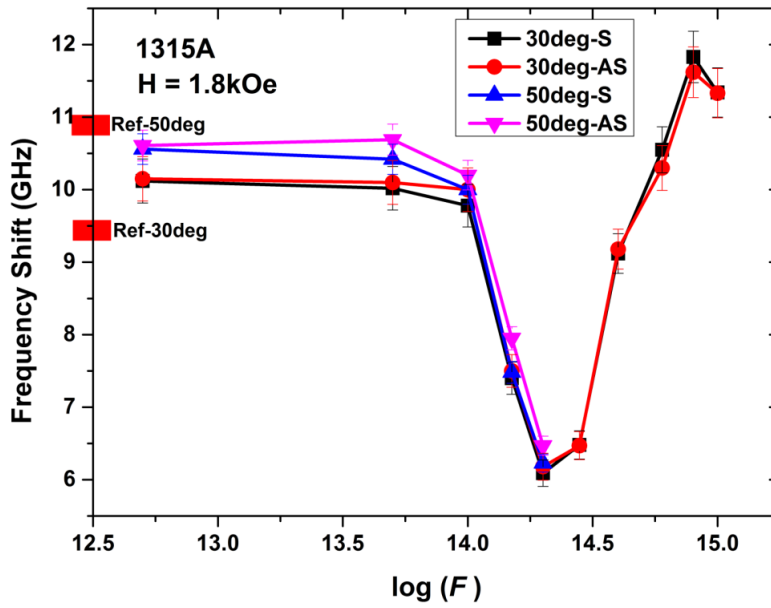


Figure. 4.50: Dependence of observed frequencies on fluence of Ga^+ ions. Stokes (S), anti-Stokes (AS) and values from reference area are also shown

dispersion behavior. Figure 4.51(a) shows the overall dependence of spin wave excitation for the whole coverage of fluence. One can see two minima in observed spin wave excitation which corresponds to the two out-of-plane magnetization states (See Fig. 4.42). Effective anisotropy field calculated by Eq. (4.3.3) is summarized in Fig. 4.51(b). The results from PMOKE and BLS are compared which are in good agreement. The irradiation changes only anisotropy (Maz12), perhaps also somehow, the magnetization saturation and exchange interactions. In any case the spin waves shall preserve the change of frequency with the change of the wavevector. However, the slope of the dispersion curve can be different (as can be seen in Fig. 4.50), and in some limited range of the wave vector the dispersion relation can be almost horizontal line.

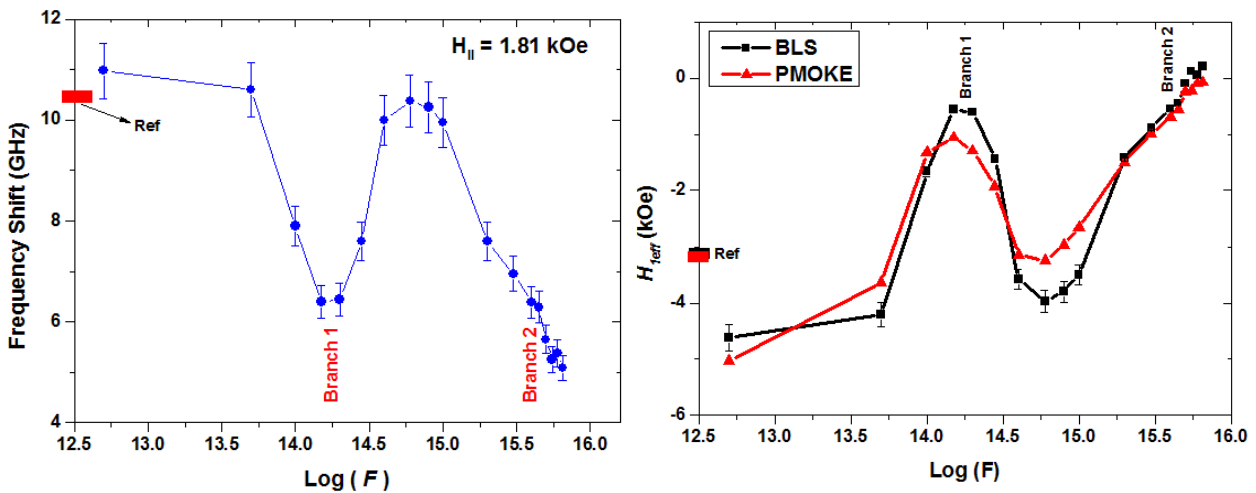


Figure. 4.51: (a) : Dependence of observed frequencies on fluence of Ga^+ ions , (b) Effective anisotropy calculation (black filled square (BLS) and red filled triangles (PMOKE) as function of fluence of Ga^+ ions.

As Maziewski et.al [Maz12] have shown that there is change in magnetic anisotropy with the increase in fluence. The reasons why frequency of the observed spin wave excitation changes with anisotropy and observed smaller dispersion relation at higher fluence can be explained by Fig. 4.52. We have shown dispersion characteristics with different magnetic anisotropies values calculated by using Eq. (1) from Ref. [Zha15] (neglecting DMI values). Curve in blue is for $M_s = 1 \times 10^6$ A/m, $A = 1 \times 10^{-11}$ J/m; anisotropy field = 0.8 T, film thickness 3.5 nm; gamma 180GHz/T; while for for red curve higher anisotropy field of 1.2 T is used [Zha15]. One can see that the change in the observed spin wave excitation with fluence is similar to observed experimental results (Fig. 4.50). The slope for the red line is very small as compared

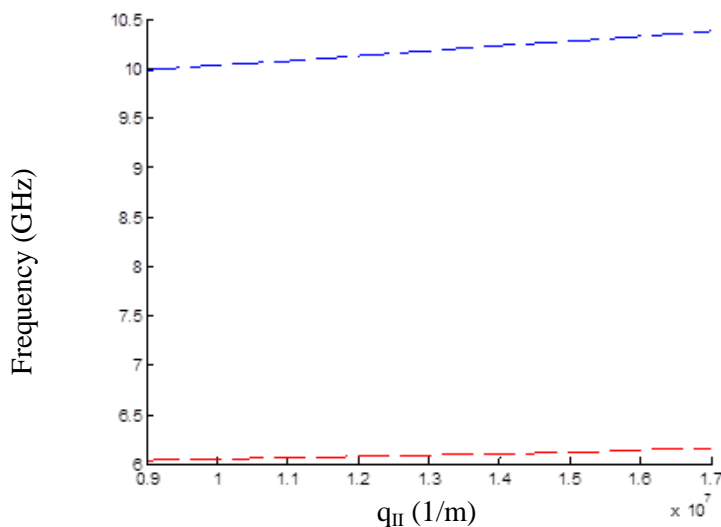


Figure. 4.52: Dispersion characteristics for different magnetic anisotropy (red dotted line 0.8T , and blue dotted line 1.2T)

to the blue line (smaller anisotropy field) consistent with the observed results (Fig. 4.50).

Summary

By selecting appropriate fluence of the irradiated two out-of plane magnetization states were induced. These out-of-plane magnetization states can be connected to the different magnetic anisotropy due to the formation of new alloys such as $\text{Co}_{50}\text{Pt}_{50}$, (L_{10} phase) and $\text{Co}_{0.25}\text{Pt}_{0.75}$, are responsible for inducing PMA in the branches 1 and 2 respectively [Maz12]. There is a remarkable effect of fluence on the spin wave excitation where two minima correspond to the two-of-plane magnetization states (due to the different magnetic anisotropy). Effective field (H_{eff}) calculated from BLS measurements matches quite well the values estimated from the PMOKE. Our study suggest that tuning the frequency of spin wave through fluence of irradiated ions can leads to the fabricating of potential magnonic crystals based on changes in magnetic anisotropy.

5. Conclusions

The statics and dynamics of magnetization in patterned Py, and ion-irradiated Fe₆₀Al₄₀, and Co nanostructures has been studied by employing magneto-optical Kerr effect microscopy (MOKE) and three spectrometries: Brillouin light scattering (BLS), X-band ferromagnetic resonance (FMR) and vector network analyzer ferromagnetic resonance (VNA-FMR).

Thin films of disordered Fe₆₀Al₄₀ alloy with depth varying magnetization (depending on energy (E) of irradiated ions) showed that magnetic domain patterns and magnetization reversal mechanisms strongly depends on E . It is observed that for $E \leq 5$ keV, MR is dominated through nucleation centers while for $E > 5$ keV, MR is carried through domain wall propagation. DE and SSW modes are identified; for $E < 15$ keV, only the DE mode is detected, for $15 \leq E < 20$ keV, a lower frequency SSW is induced, and for $E \geq 20$ keV, the DE mode is observed to lie in-between two SSW modes. In conclusion, with analytical calculation the transient magnetization at the A2/B2 interface acts as the asymmetric SW pinning site.

The systematic inclusion of additional antidot structures in the basic square antidot lattice in Py samples showed that one can control the magnetic anisotropy (four-fold in square antidot lattice, eight-fold when additional antidot is included inside the square lattice, and two-fold in wave-like patterns) through the patterning. The easy (when the antidots are at larger distance) and hard axis (when the antidots are at larger distance) are visible from LMOKE hysteresis. The presence of in-plane magnetic anisotropies are further confirmed by FMR measurements and fundamental, bulk and edge modes are classified with the support of the MuMax calculations. Our findings suggest that the inclusion of additional antidot inside the basic square unit cells leads to the additional resonances lines both at low field and high field regime connected to the bulk modes and edge modes respectively. For wavelike patterns (field perpendicular to the wavelike patterns), the clear difference in high field regime is due to the edge modes because of difference in demagnetizing field distribution at the different edges of the wave-like patterns.

In Pt/Co/Pt nanostructures, two minima in the thermally excited spin waves excitations as function of fluence are connected to changes in magnetic anisotropy responsible for creation of two out-of-plane magnetization states. The estimation of the effective field calculation is in

good agreement with the PMOKE studies. Our study suggests that tuning the frequency of spin wave through fluence of irradiated ions can lead to the fabricating of potential magnonic crystals based on magnetic anisotropy changes.

6. References

- [Ade04]. A. O. Adeyeye, and N. Singh, “Large area patterned magnetic nanostructures”, *J. Phys. D: Appl. Phys.*, **4**, 1153001 (2008).
- [Ade08]. A. O. Adeyeye, S. Goolaup, N. Singh, W. Jun, C. C. Wang, S. Jain, and D. Tripathy, “Magnetic_Reversal Mechanisms in Ferromagnetic Nanostructures”, *IEEE. Trans. Magn.*, **44**, 1935 (2008).
- [Ake04]. J. Akerman, P. Brown, M. DeHerrera, M. Durlam, E. Fuchs, D. Gajewski, M. Griswold, J. Janesky, J. J. Nahas, and S. Tehrani, “Demonstrated reliability of 4-mb MRAM”, *Device and Materials Reliability, IEEE Transactions on*, **4**, 428 (2004).
- [Bad06]. S. D. Bader, “Colloquium: Opportunities in nanomagnetism”, *Rev. Mod. Phys.*, **78**, (2006).
- [Bal14]. R. Bali, S. Wintz, F. Meutzner, R. Hübner, R. Boucher, A. A. Ünal, S. Valencia, A. Neudert, K. Potzger, J. Bauch, F. Kronast, S. Facsko, J. Lindner, and J.Fassbender, “Printing nearly-discrete magnetic patterns using chemical disorder induced ferromagnetism,” *Nano. Lett.* **14** (2), 435(2014).
- [Ber10]. H. Bernas, *Material Science with Ion Beams, Topics in Applied Physics*, 116 Springer-Verlag, Berlin, (2010).
- [Bil07]. C. Bilzer, T. Devolder, P. Crozat, C. Chappert, S. Cardoso, P. P. Freitas, *J. Appl. Phys.* **101** (7), 074505 (2007).
- [Blo30]. F. Bloch, *Zur theorie des ferromagnetismus, Zeitschrift für Physik* **61**, 206 (1930).
- [Blu01]. Stephen Blundell “*Magnetism in Condensed Matter*”, Oxford University Press Inc., New York, (2001).
- [Bro02]. F.J.A. den Broeder, W. Hoving, P.J.H. Bloemen: “Magnetic anisotropy of multilayers”, *J. Magn. Magn. Mater.* **93**, 562–570 (2002).
- [Bru97]. J. H. Brunning, *SPIE*, **3049**, 14-27 (1997).
- [Bur11]. E. Burgos, E. Sallica Leva, J. Gómez, F. Martínez Tabares, M. Vásquez Mansilla, and A. Butera, *Phys. Rev* **83**, 174417 (2011).
- [Cam00]. J. Camarero, J. J. De Miguel, R. Miranda and A. Hernando, “Thickness-dependent coercivity of ultrathin Co films grown on Cu(111),” *J. Phys. Condens. Matter* **12**, 7713-7719 (2000).
- [Car00]. G. Gubbiotti, L. Albini, G. Carlotti, M. De Crescenzi, E. Di Fabrizio, A. Gerardino, O. Donzelli, F. Nizzoli, H. Koo, and R. D. Gomez, “Finite size effects in patterned magnetic permalloy films”, *J. Appl. Phys.*, **87**, 5633 (2000).

- [Car14]. G. Carlotti, G. Gubbiotti, M. Madami, S. Tacchi, F. Hartmann, M. Emmerling, M. Kamp and L. Worschech, “From micro- to nanomagnetic dots: evolution of the eigenmode spectrum on reducing the lateral size”, *J. Phys. D: Appl. Phys.*, **47**, 265001 (2014).
- [Car99]. G. Carlotti, and G. Gubbiotti, “Brillouin scattering and magnetic excitations in layered structures”, *Rivista Del Nuovo Cimento*, **22**, (1999).
- [Cas04]. F. J. Castaño, K. Nielsch, C. A. Ross, J. W. A. Robinson, and R. Krishnan, “Anisotropy and magnetotransport in ordered magnetic antidot arrays”, *Appl. Phys. Lett.*, **85**, 2872, (2004).
- [Cha01]. G. S. Chang, Y. P. Lee, J. J. Y. Rhee, J. Lee, K. Jeong, and C. N. Whang, *Phys. Rev. Lett.* **87**, 067208 (2001).
- [Cha98]. C. Chappert, H. Bernas, J. Ferre, V. Kottler, J.-P. Jamet, Y. Chen, E. Cambril, T. Devolder, F. Rousseaux, V. Mathet, and H. Launois, “Planar patterned magnetic media obtained by ion irradiation,” *Science* **280**, 1919-1922 (1998).
- [Coc91]. J. F. Cochran, W. B. Muir, J. M. Rudd, B. Heinrich, Z. Celinski, and Tan-Trung Le-Tran, W. Schwarzacher, W. Bennett, and W. F. Egelhoff, Jr., “Magnetic anisotropies in ultrathin Fe(001) films grown on Cu(001) substrates”, *J. Appl. Phys.* **69**, 5206 (1991).
- [Cul09]. B. D. Cullity, and C. D. Graham, “Introduction to Magnetic materials”, John Wiley & Sons, Inc., Hoboken, New Jersey, 2009.
- [Dam61]. R. W. Damon and J. R. Eshbach, *J. Phys. Chem. Solid*, **19**, 308 (1961).
- [Dem01]. S. O. Demokritov, B. Hillebrands, and A. N. Slavin, *Phys. Rep* **348**, 441–489 (2001).
- [Dem13]. S. O. Demokritov and A. N. Slavin, “Magnonics: From Fundamental to Applications”, Springer, 2013.
- [Dev00]. T. Devolder, *Phys. Rev. B*, **62**, 5794 (2000).
- [Ebe97]. U. Ebels, A. O. Adeyeye, M. Gester, R. P. Cowburn, C. Daboo, and J. A. Bland, “Anisotropic domain evolution in epitaxial Fe/GaAs (001) wires”, *Phys. Rev. B*, **56**, pp. 5443-5451, (1997).
- [Far98]. M. Farle, *Rep. Prog. Phys.* **61**, 755 (1998).
- [Fas04]. J. Fassbender, D. Ravelosona, and Y. Samson, “Tailoring magnetism by light-ion irradiation,” *J. Phys. D: Appl. Phys* **37**, R179-R196 (2004).
- [Fas06]. J. Fassbender, A. Mucklich, K. Potzger, W. Moller, “Mixing and subsequent amorphization of ultrathin Ni₈₁Fe₁₉/Ta bilayers by 30 keV Ni implantation,” *Nucl. Instrum. Methods B* **248**, 343 (2006).

[Fas08]. J. Fassbender, and J. McCord, “Magnetic patterning by means of ion irradiation and implantation”, *J. Magn. Magn. Mat.*, **320**, 579 (2008).

[Fas08a]. J. Fassbender, M. O. Liedke, T. Strache, W. Möller, E. Menéndez, J. Sort, K. V. Rao, S. C. Deevi, and J. Nogués, “Ion mass dependence of irradiation-induced local creation of ferromagnetism in Fe₆₀Al₄₀ alloys,” *Phys. Rev. B* **77**, 174430 (2008).

[Fat62]. E. Fatuzzo, “Theoretical considerations on the switching transient in ferroelectrics,” *Phys. Rev* **127**, 6 (1962).

[Fea02]. I. Ruiz-Feal, L. Lopez-Diaz, A. Hirohata, J. Rothman a, C.M. Guertler, J.A.C. Bland, L.M. Garcia, J.M. Torres, J. Bartolome, F. Bartolome, M. Natali c , D. Decanini c , Y. Chen, “Geometric coercivity scaling in magnetic thin film antidot arrays”, *J. Magn. Magn. Matr.*, **242-245**, 597 (2002).

[Fel67]. E. Feldtkeller, K.U. Stein: Verbesserte Kerr-Technik zur Beobachtung magnetischer Domanen. *Z. Angew. Phys.* **23**, 100–102 (1967).

[Fer97]. J. Ferré, V. Grolier, P. Meyer, S. Lemerle, A. Maziewski, E. Stefanowicz, et al, “Magnetization-reversal processes in an ultrathin Co/Au film”, *Phys. Rev. B*, vol. 55, pp. 15092 (1997).

[Fer99]. J. Ferré, C. Chappert, H. Bernas, J. P. Jamet, P. Meyer, O. Kaitasov, S. Lemerle, V. Mathet, F. Rousseaux and H. Launois, *J. Magn. Magn. Mater* , 198-199, 191 (1999).

[Fid96]. J. Fidler, T. Schrefl, “Overview of Nd-Fe-B magnets and coercivity”, *J. Appl. Phys.*, **79**, 5029 (1996).

[Gau13]. N. Gaur, S. Kundu, S. N. Piramanayagam, S. L. Maurer, H. K. Tan, S. K. Wong, S. E. Steen, H. Yang, and C. S. Bhatia,, “Lateral displacement induced disorder in L10-FePt nanostructures by ion-implantation,” *Sci. Rep* **3**, 1907 (2013).

[Gie007]. F. Giesen, J. Podbielski, and D. Grundler, *Phys. Rev. B* **76**, 014431 (2007).

[Gie05]. Giesen, J. Podbielski, T. Korn, and D. Grundler, *J. Appl. Phys.* **97**, 10A712 (2005).

[Gil04]. T. Gilbert, *Classics in magnetics A phenomenological theory of damping in ferromagnetic materials*, *IEEE Transactions on Magnetics* **40**, 3443 (2004)].

[Gio01]. L. Giovannini, R. Zivieri, G. Gubbiotti, G. Carlotti, L. Pareti, G. Turilli, “”Theory of Brillouin cross section for scattering from magnetic multilayers: Second-order magneto-optic effect in Ni/Cu bilayers and trilayers, *Phys. Rev. B*, **63**, 1 (2001).

[Gre62]. A. Green, M. Prutton: Magneto-optic detection of ferromagnetic domains using vertical illumination. *J. Sci. Instrum.* **39**, 244–245 (1962).

[Gri46]. J. H. E. Griffiths, Anomalous high-frequency resistance of ferromagnetic metals, *Nature* **158**, 670 (1946).

- [Gue02]. I. Guedes, M. Grimsditch, V. Metlushko, P. Vavassori, R. Camley, B. Ilic, P. Neuzil and R. Kumar, “Domain formation in arrays of square holes in an Fe film”, *Phys. Rev. B*, **66**, 014434 (2002).
- [Gue03]. I. Guedes, M. Grimsditch, V. Metlushko, P. Vavassori, R. Camley, B. Ilic, P. Neuzil and R. Kumar, “Magnetization reversal in an Fe film with an array of elliptical holes on a square lattice”, *Phys. Rev. B*, **67**, 024428 (2003).
- [Gur96]. A. G. Gurevich and G. A. Melkov, *Magnetization Oscillations and Waves* (CRC Press, Boca Raton, New York, 1996).
- [Gur96]. A. G. Gurevich, G. A. Melkov, *Magnetization oscillations and waves*, CRC Press, New York (1996).
- [Hai06]. L. Haiyan, Ph.D dissertation (“Brillouin scattering study of magnons in magnetic nanostructures”), NUS, Singapore (2006).
- [Hei28]. W. Heisenberg, Zur theorie des ferromagnetismus, *Zeitschrift für Physik* **49**, 619 (1928).
- [Hel01]. O. Hellwig, D. Weller, A. J. Kellock, J. E. E. Baglin and E. E. Fullerton, “Magnetic patterning of chemically-ordered CrPt3 films,” *Appl. Phys. Lett* **79**, 1151 (2001).
- [Hel34]. G. Heller and H. A. Kramers, *Proc. K. Akad. Wet.* **37**, 378 (1934).
- [Her04]. R. Hertel, W. Wulfhekel, and J. Kirschner, *Phys. Rev. Lett.* **93**, 257202 (2004).
- [Her51]. C. Herring, and C. Kittel, *Phys. Rev.* **81**, 869 (1951).
- [Her98]. A. Hernando, X. Amils, J. Nogues, S. Surinach, M. D. Baro, and M. R. Ibarra, “Influence of magnetization on the reordering of nanostructured ball-milled Fe-40 at. % Al powders,” *Phys. Rev. B* **58**, R11864 (1998).
- [Hil87]. B. Hillebrands, P. Baumgart, and G. Güntherodt, *Phys. Rev. B* **36**, 2450 (1987)
- [Hil93]. B. Hillebrands, J. H. Hazer, G. Güntherodt, J. R. Dutcher, “Study of Co-based multilayers by Brillouin light scattering”, *J. Mag. Soc. Jpn*, **17**, 17 (1993).
- [Hri02]. B. Heinrich, R. Urban, G. Woltersdorf, *Magnetic relaxation in metallic films: Single and multilayer structures*, *J. Appl. Phys.* **91**, 7523 (2002).
- [Hub09]. Alex Hubert, and Rudolf Schäfer, “*Magnetic Domains*”, Springer, Berlin Heidelberg, New York, (2009).
- [Hub67]. A. Hubert: Der Einfluß der Magnetostriktion auf die magnetische Bereichsstruktur einachsiger Kristalle, insbesondere des Kobalts. *Phys. Stat. Sol.* **22**, 709–727 (1967).
- [Hyn01]. R. Hyndman, P. Warin, J. Gierak, J. Ferré, J. N. Chapman, J. P. Jamet, V. Mathet and C. Chappert, *J. Appl. Phys.* **90**, 3843 (2001).

- [Jun02]. S. Jung, B. Watkins, L. DeLong, J. B. Ketterson, and V. Chandrasekhar, "Ferromagnetic resonance in periodic particle arrays", *Phys. Rev. B*, **66**, 132401 (2002).
- [Jun13]. M. B. Jungfleisch, T. An, K. Ando, Y. Kajiwara, K. Uchida, V. I. Vasyuchka, A. V. Chumak, A. A. Serga, E. Saitoh, B. Hillebrands, Heat-induced damping modification in yttrium iron garnet/platinum hetero-structures, *App. Phys. Lett*, **102**, 062417 (2013).
- [Kam70]. V. Kambersk'y, On the Landau-Lifshitz relaxation in ferromagnetic metals, *Canad. J. Phys*, **48**, 2906 (1970).
- [Kam75]. V. Kambersky, C. Patton, Spin-wave relaxation and phenomenological damping in ferromagnetic resonance, *Phys. Rev. B*, **11**, 2668 (1975).
- [Kap13]. A. Kapelrud, A. Brataas, Spin Pumping and enhanced Gilbert damping in thin magnetic insulator films, *Phys. Rev. Lett*, **111**, 097602 (2013).
- [Khi07]. A. Khitun, D. E. Nikonov, M. Bao, K. Galatsis, and K. L. Wang, *Nanotechnology* 18, 465202 (2007).
- [Khi08]. A. Khitun, M. Bao, and K. L. Wang, *IEEE Trans. Magn.* 44, 2141 (2008).
- [Kis03]. M. Kisielewski, Z. Kurant, M. Tekielak, W. Dobrogowski, A. Maziewski, A. Wawro, and L. T. Baczewski, "Magneto-optical micromagnetometry of ultrathin Co wedges," *Phys. Stat. solid (a)* **196**, 1, 129-132 (2003).
- [Kit47]. C. Kittel, Interpretation of anomalous Larmor frequencies in ferromagnetic resonance experiment, *Physical Review* 71, 270 (1947).
- [Kit48]. C. Kittel. "On the theory of ferromagnetic resonance absorption". *Phys. Rev.*
- [Kit53]. C. Kittel, E. Abrahams, Relaxation process in ferromagnetism, *Rev. Mod. Phys*, **25**, 233 (1953).
- [Kra91]. P. Krams, B. Hillebrands, G. Güntherodt, K. Spörl and D. Weller, *J. Appl. Phys.* 69, 5307 (1991).
- [Kro07]. H. Kronmuller, and S. Parkin, "Handbook of magnetism and advances magnetic materials", Vol 4, (Wiley, New York, 2007).
- [Kro91]. H. Kronmuller, "Science and Technology of Nanostructured Materials," p. 657. Plenum, New York, (1991).
- [Kru10]. V. V. Kruglyak, S. O. Demokritov, and D. Grundler, "Magnonics", *J. Phys. D: Appl. Phys*, **43** 244001 (2010).
- [Lab89]. M. Labrune, S. Andrieu, F. Rio, and P. Bernstein, "Time dependence of the magnetization process RE-TM alloys," *J. Magn. Magn. Mater* **80**, 211-218 (1989).

- [Lan35]. L. Landau, E. Lifshits, On the theory of the dispersion of magnetic permeability in ferromagnetic bodies, *Physikalische Zeitschrift der Sowjetunion* **8**, 153 (1935).
- [Lax94]. V. S. Lvov, *Wave Turbulence under parametric excitation*, Springer, Berlin, 1994.
- [Lee08]. K. S. Lee and S. K. Kim, *J. Appl. Phys.* **104**, 053909 (2008).
- [Len11]. B. Lenk, H. Ulrichs, F. Garbs, M. Münzenberg, “The building blocks of magnonics”, *Phys. Rep.* **507**, 107 (2011).
- [Lo13]. C. K. Lo, “Instrumentation for ferromagnetic resonance spectrometer”, Chap. 2, INTECH, 2013.
- [Lod04]. J. C. Lodder, “Methods for preparing patterned media for high-density recording”, *J. Magn. Magn. Mate.* **227-276**, 1692-1697 (2004).
- [Mak86]. A. Maksymowicz, *Phys. Rev. B* **33**, 6045 (1986).
- [Man15]. R. Mandal, S. Barman, S. Saha, Y. Otani, and A. Barman, “Tunable spin wave spectra in two-dimensional Ni₈₀Fe₂₀ antidot lattices with varying lattice symmetry”, *J. Appl. Phys.* **118**, 053910 (2015).
- [Mar07]. O. N. Martyanov, V. F. Yudanov, R. N. Lee, S. A. Nepijko, H. J. Elmers, R. Hertel, C. M. Schneider, and G. Schönense, “Ferromagnetic resonance study of thin film antidot arrays: Experiment and micromagnetic simulations”, *Phys. Rev. B*, **75**, 174429 (2007).
- [Mat08]. Mathias Getzlaff, “Fundamental of Magnetism”, Springer-Verlag Berlin Heidelberg (2008).
- [Maz12]. A. Maziewski, P. Mazalski, Z. Kurant, M. O. Liedke, J. McCord, J. Fassbender, J. Ferré, A. Mougin, A. Wawro, L. T. Baczewski, A. Rogalev, F. Wilhelm, and T. Gemming, “Tailoring of magnetism in Pt/Co/Pt ultrathin films by ion irradiation,” *Phys. Rev. B*, **85**, 054427 (2012).
- [Maz13]. P. Mazalski, “Ph. D dissertation”, University of Bialystok, Poland, (2013).
- [Mc08]. J. McCord, L. Schultz, and J. Fassbender, “Hybrid soft-magnetic lateral exchange spring films prepared by ion irradiation,” *J. Adv. Mater* **20**, 2090 (2008).
- [McG05]. D. McGrouther, J. N. Chapman, “Nanopatterning of a thin ferromagnetic CoFe film by focused-ion-beam irradiation,” *Appl. Phys. Lett* **87**, 022507 (2005).
- [McM06]. R. D. McMichael, and B. B. Marnaville, “Edge saturation and dynamic edge modes in ideal and nonideal magnetic film edges”, *Phys. Rev. B*, **74**, 024424 (2006).
- [McM95]. J. McCord, H. Brendel, A. Hubert, S.S.P. Parkin: Hysteresis and domains in magnetic multilayers. *J. Magn. Magn. Mat.* **148**, 244–246 (1995).
- [Men09]. E. Menendez, M. O. Liedke, J. Fassbender, T. Gemming, A. Weber, L. J. Heyderman, K. V. Rao, S. C. Deevi, S. Surinach, M. D. Baro, J. Sort, and J. Nogues, “Direct magnetic patterning due to the generation of ferromagnetism by selective ion irradiation of paramagnetic FeAl alloys,” *Small*, **5**(2), 229-234 (2009).

- [Mis87]. R. K. Mishra, "Microstructure of hot-pressed and die-upset NdFeB magnets", J. Appl. Phys, **62**, 967 (1987).
- [Mis88]. R. K. Mishra, E. G. Brewer, R. W. Lee, "Grain growth and alignment in hot deformed Nd-Fe-B magnets", J. Appl. Phys, **63**, 3528 (1988).
- [Mos99]. A. Moser and D. Weller, IEEE Trans.Magn. **35**, 4423 (1999).
- [Nib03]. J. P. Nibarger, R. Lopusnik, Z. Celinski, and T. J. Silva, Appl. Phys. Lett. **83**, 93 (2003).
- [Nis15]. T. Nishinga, "Handook of crystal growth", Vol III, Elsevier, 225 Wyman Street, Waltham, MA 02451, USA.
- [Obr13]. B. Obry, Design der Spinwellenpropagation durch eine magnetische Strukturierung einund zweidimensionaler Systeme, Ph.D. thesis, Department of Physics, TU Kaiserslautern, Germany (2013)].
- [Pat84]. C. F. Patton, Magnetic excitations in solids, Physics Reports **5**, 251 (1984).
- [Ped10]. Pedro M. S. Monteiro and D. S. Schmool, Phys. Rev. B **81**, 214439 (2010).
- [Ped10]. Pedro M. S. Monteiro and D. S. Schmool, Phys. Rev. B **81**, 214439 (2010).
- [Pod05]. J. Podbielski, F. Giesen, M. Berginski, N. Hoyer, and D. Grundler, Superlattices and Microstructures **37**, 341 (2005).
- [Pod06]. J. Podbielski, F. Giesen, and D. Grundler, Phys. Rev. Lett. **96**, 167207 (2006).
- [Pus79]. H. Puzkarski, Prog. Surf. Sci **9**, 191 (1979).
- [Pus79]. H. Puzkarski, Prog. Surf. Sci **9**, 191 (1979).
- [Ram76]. O. G. Ramer and C. H. Wilts, Phys. Stat. Sol. (b) **73**, 443 (1976).
- [Ram88]. R. Ramesh, G. Thomas, B. H. Ma, "Magnetization reversal in nucleation controlled magnets. II. Effect of grain size and size distribution on intrinsic coercivity of Fe-Nd- B magnets", J. Appl. Phys, **64**, 6416 (1988).
- [Rap04] T. G. Rappoport, P. Redlinski, X. Liu, G. Zaránd, J. K. Furdyna, and B. Jankó, Phys. Rev. B **69**, 125213 (2004).
- [Rap04]. T. G. Rappoport, P. Redlinski, X. Liu, G. Zaránd, J. K. Furdyna, and B. Jankó, Phys. Rev. B **69**, 125213 (2004).
- [Sag87]. M. Sagawa, S. Hirosawa, H. Yamamoto, S. Fujimura, Y. Matsuura, "Nd-Fe-B permanent magnet materials", Jpn. J. Appl. Phys, **26**, 785 (1987).

- [San10]. J. R. Sandercook, “Operator manual of TANDEM FABRY-PEROT INTERFEROMETER TFP-1”, 2010.
- [Sch12]. H. Schultheiss, K. Vogt, B. Hillebrands, Direct observation of nonlinear four-magnon scattering in spin-wave microconduits, *Physical Review B* **86**, 2 (2012).
- [Sch86]. F. Schmidt, A. Hubert: Domain observations on CoCr layers with a digitally enhanced Kerr microscope. *J. Magn. Magn. Mat.* **61**, 307–320 (1986).
- [Sch87]. L. Schultz, J. Wecker, E. Hellstern, “Formation and properties of NdFeB prepared by mechanical alloying and solid-state reaction”, *J. Appl. Phys.* **61**, 3583 (1987).
- [Sch88]. L. Schultz, K. Schnitzke, J. Wecker, “Mechanically alloyed isotropic and anisotropic Nd-Fe-B magnetic material”, *J. Appl. Phys.* **64**, 5302 (1988).
- [Sel02]. D. J. Sellmyer, C. P. Luo, Y. Qiang, and J. P. Liu, Magnetism of Nanophase Composite Films, *Handbook of Thin Film Materials* H. S. Nalwa. Academic press, 2002.
- [She02]. J. Shen, and J. Krischner, “Tailoring magnetism in artificially structured materials: the new frontier”, *Surf. Sci.* **500**, 300 (2002).
- [Sin04]. N. Sing, S. Goolaup, A. O. Adeyeye, “fabrication of large area nanomagnets”, *Nanotechnology*, **15**, 1539-1544 (2004).
- [Sko03]. R. Skomski, “Nanomagnetics_Topical review”, *J. Phys. Cond. Matt*, **15**, R841 (2003).
- [Sor06]. J. Sort, A. Concustell, E. Menéndez, S. Surinach, K. V. Rao, S.C. Deevi, M. D. Baró, and J. Nogués, “Periodic Arrays of Micrometer and Sub-micrometer Magnetic Structures Prepared by Nanoindentation of a nonmagnetic intermetallic compound,” *Adv. Mater.* **18**, 1717 (2006).
- [Spa70]. M. Sparks, *Phys. Rev. B* **1**, 3869 (1970).
- [Sta09]. D. Stancil and A. Prabhakar, *Spin Waves: Theory and Applications* (Springer, 2009).
- [Sta09]. D. Stancil and A. Prabhakar, *Spin Waves: Theory and Applications* (Springer, 2009).
- [Stu03]. P. Stuart, X. Jiang, K. Christian, A. Panchula, K. Roche, and S. Mahesh, “Magnetically engineered spintronic sensors and memory”, *Proceedings of the IEEE*, **91**, (2003).
- [Suh98]. H. Suhl, Theory of the magnetic damping constant, *IEEE Trans. Magn.* **34**, 1834 (1998)].
- [Sun05]. J. Z. Sun, B. Ozyilmaz, W. Chen, M. Tsoi, A. D. Kent, Spin-transfer-induced magnetic excitation: The role of spin-pumping induced damping, *J. Appl. Phys.* **97**, 10C714 (2005).
- [Tac14]. S. Tacchi, S. Fin, G. Carlotti, et.al, *Phys. Rev. B.* **89**, 024411 (2014).

- [Tah14]. N. Tahir, R. Gieniusz, A. Maziewski, R. Bali, M. P. Kostylev, S. Wintz, H. Schultheiss, S. Facsko, K. Potzger, J. Lindner, J. Fassbender, “Magnetization reversal of disorder-induced ferromagnetic regions in Fe₆₀Al₄₀ thin films,” *IEEE. Trans. Magn* **50**, 11 (2014).
- [Tah15]. N. Tahir, R. Gieniusz, A. Maziewski, R. Bali, K. Potzger, J. Lindner, and J. Fassbender, “Evolution of magnetic domain structure formed by ion-irradiation of B2-Fe_{0.6}Al_{0.4},” *Opt. Exp* **23** (13), 16575 (2015).
- [Tah15a]. N. Tahir, R. Bali, R. Gieniusz, S. Mamica, J. Gollwitzer, T. Schneider, K. Lenz, K. Potzger, J. Lindner, M. Krawczyk, J. Fassbender, and A. Maziewski, “Tailoring dynamic magnetic characteristics of Fe₆₀Al₄₀ films through ion irradiation”, *Phys. Rev. B*, Accepted. (2015).
- [Tre61]. D. Treves: Limitations of the magneto-optic Kerr technique in the study of microscopic magnetic domain structures. *J. Appl. Phys* **32**, 358–364 (1961).
- [Tri10]. D. Tripathy, P. Vavassori, J. M. Porro, A. O. Adeyeye, and N. Singh, “Magnetization reversal and anisotropic magnetoresistance behavior in bicomponent antidot nanostructures”, *Appl. Phys. Lett*, **97**, 042512 (2010).
- [Ulr00]. W. Ulrich, S. Beiersdorfer and H. J. Mann, *Proc. SPIE*, **13-24**, 4146 (2000).
- [Vas07]. S. V. Vasiliev, V. V. Kruglyak, M. L. Sokolovskii, and A. N. Kuchko, *J. Appl. Phys.* **101**, 113919 (2007).
- [Vav02]. P. Vavassori, G. Gubbiotti, G. Zangari, C. T. Yu, H. Yin, H. Jiang, and G. J. Mankey, “Lattice symmetry and magnetization reversal in micron-size antidot arrays in Permalloy film”, *J. Appl. Phys.*, **10**, 7992 (2002).
- [Vog11]. A. Vogel, S. Wintz, T. Gerhardt, L. Boklage, T. Strache, Mi-Y. Im, P. Fischer, J. Fassbender, J. McCord, and G. Meier, “Field- and current-induced domain-wall motion in permalloy nanowires with magnetic soft spots,” *Appl. Phys. Lett* **98**, 20250 (2011).
- [Vos78]. J. L. Vossen, W. Kern (Eds.), *Thin Film Processes*. Academic Press, 1978, and reference therein.
- [Wan06]. C. C. Wang, A. O. Adeyeye, and N. Singh, “Magnetic antidot nanostructures: effect of lattice geometry”, *Naotech*, **17**, 1629 (2006).
- [Was12]. K. Wasa, I. Kanno, and H. Kotera, “Handbook of sputtering deposition technology”, 2nd edition, Elsevier, 225 Wyman Street, Waltham, 02451 New York (2012), USA.
- [Wec87]. J. Wecker, L. Schultz, “Coercivity after heat treatment of overquenched and optimally quenched Nd-Fe-B”. *J. Appl. Phys.*, **62**, 990 (1987).
- [Wes00]. J. H. Westbrook and R. L. Fleischer, *Intermetallic Compounds Volume 3, Structural Applications of Intermetallic Compounds*, John Wiley and Sons, New York, 2000.

- [Wig61]. P. E. Wigen, C. F. Kool, M. R. Shanabarger, and T. D. Rossing, *Phys. Rev. Lett* **9**, 206 (1961).
- [Woo00]. R. Wood, “The feasibility of magnetic recording at 1 terabit per square inch”, *IEEE. Trans. Magn.* **36**, 36(2000).
- [Yos04]. A. Yoshihara, W. D. Li, O. Kitakami, and Y. Shimada, “Brillouin light scattering from collective spin waves in Fe–Al–O granular films”, *J. Magn. Magn. Mat.* **268**, 257-263 (2004).
- [Yu00]. C. T. Yu, H. Jiang, L. Shen, P. J. Flanders, and G. J. Mankey, “The magnetic anisotropy and domain structure of permalloy antidot arrays”, *J. Appl. Phys.* **87**, 6322 (2000).
- [Yu03]. C. Yu, M. J. Pechan, G. J. Mankey, “Dipolar induced, spatially localized resonance in magnetic antidot arrays”, *Appl. Phys. Lett*, **83**, 3948 (2003).
- [Yu04]. C. Yu, M. J. Pechan, and W. A. Burei, “Lateral standing spin waves in permalloy antidot arrays”, *J. Appl. Phys.* **95**, 6648 (2004).
- [Zha15]. V. L. Zhang, K. Di. H. S. Lim, S. C. Ng, M. H. Kuok, J. Yu, J. Yoon, X. Qiu, and H. Yang, “In-plane angular dependence of the spin-wave nonreciprocity of an ultrathin film with Dzyaloshinskii-Moriya interaction”, *Appl. Phys. Lett*, **107**, 022402 (2015).
- [Zho13]. Y. Zhou, H. J. Jiao, Y. Chen, G. E. W. Bauer, and J. Xiao, *Phys. Rev. B* **88**, 184403 (2013).
- [Zho13]. Y. Zhou, H. J. Jiao, Y. Chen, G. E. W. Bauer, and J. Xiao, *Phys. Rev. B* **88**, 184403 (2013).
- [Zuk92]. J. Zuk, H. Kief, M. J. Clouter, “Brillouin scattering study of surface acoustic waves in crystalline GaP”, *J. Appl. Phys.* **72**, 3504 (1992).

6. List of publications

(Related to Dissertation)

1. **N. Tahir**, R. Bali, R. Gieniusz, S. Mamica, J. Gollwitzer, T. Schneider, K. Lenz, K. Potzger, J. Lindner, M. Krawczyk, J. Fassbender, and A. Maziewski, “Tailoring dynamic magnetic characteristics of Fe₆₀Al₄₀ films through ion irradiation”, **Phys. Rev. B**, **92**, 144429 (2015).
2. **N. Tahir**, R. Gieniusz, A. Maziewski, R. Bali, K. Potzger, J. Lindner, and J. Fassbender, “Evolution of magnetic domain structure formed by ion-irradiation of B2-Fe_{0.6}Al_{0.4}”, **Optics Express**, **23** (13), 16575 (2015).
3. **N. Tahir**, R. Gieniusz, A. Maziewski, R. Bali, M. P. Kostylev, S. Wintz, H. Schultheiss, S. Facsko, K. Potzger, J. Lindner, J. Fassbender, “Magnetization reversal of disorder-induced ferromagnetic regions in Fe₆₀Al₄₀ thin films,” **IEEE. Trans. Magn**, **50**, 11 (2014).

(Other topics)

1. S. Y. Zhou, M. C. Langner, Y. Zhu, Y.-D. Chuang, M. Rini, T. E. Glover, M. P. Hertlein, A. G. Cruz Gonzalez, **N. Tahir**, et. al, “Glass-like recovery of antiferromagnetic spin ordering in a photo-excited manganite Pr_{0.7}Ca_{0.3}MnO₃”, **Scientific Reports**, **4**, 4050 (2014).
2. **N. Tahir**, Altaf Karim, Kristin A. Person, et.al, “Possible Source of Room Temperature Ferromagnetism in Co-Doped ZnO Nanorods”, **J. Phys. Chem. C**, **117**, 8968-8973, (2013)
3. J. Liu, M. Kargarian, M. Kareev, B. Gray, P. J. Ryan, A. Cruz, **N. Tahir**, et.al, “Heterointerface engineered electronic and magnetic phases of NdNiO₃ thin films”, **Nature Communication**, **4**, 2714 (2013).
4. Yi-De Chuang, D. Doering, A. G Cruz, **N. Tahir**, N. C. Andresen, et.al, Resonant soft-X-ray scattering endstation for time-resolved pump-probe measurements at LCLS, **SPIE Optical Engineering + Applications**, 85040G-85040G-8 (2012).

5. M. H Burkhardt, M. A Hossain, S. Sarkar, Y-D Chuang, AG Cruz Gonzalez, A Doran, A Scholl, AT Young, **N. Tahir**, et.al, Imaging the first-order magnetic transition in $\text{La}_{0.35}\text{Pr}_{0.275}\text{Ca}_{0.375}\text{MnO}_3$, **Physical Review Letters** 108 (23), 237202 (2012).
6. SY Zhou, Y Zhu, MC Langner, Y-D Chuang, P Yu, WL Yang, AG Cruz Gonzalez, **N Tahir**, et.al, “Ferromagnetic enhancement of CE-type spin ordering in (Pr, Ca) MnO_3 ”, **Physical Review Letters** 106 (18), 186404 (2011).
7. **N. Tahir**, S. T. Hussain, M. Usman, S. K. Hasanain, A. Mumtaz, Effect of vanadium doping on structural, magnetic and optical properties of ZnO nanoparticles, **Applied Surface Science** 255 (20), 8506-8510 (2009).
8. M. S. Rafique, **N. Tahir**, Influence of 250keV Ge ions fluence on electrical and optical properties of SiC, **Vacuum** 81 (9), 1062-1067 (2007).

Manuscripts under preparation

1. N. Tahir et.al, Collective spin wave excitations in the square lattice magnonic Wave-like Py Structures (under preparation).
2. N. Tahir et.al, Effect of antidot lattice geometry on magnetization reversal mechanisms. (under preparation).
3. N. Tahir, et.al, Irradiation driven changes of spin wave excitations in Pt/Co/Pt ultrathin films.

6.1. Proceedings in conferences

(Related to Ph. D dissertations)

1. **N. Tahir**, P. Mazalski, et.al, Magneto-optical studies of Ga⁺ irradiated ultrathin Co films. Abstract book IEEE 2013 summer school, June 9-14, Assisi, Italy, p. 21 (37).
2. **N. Tahir**, P. Mazalski, et.al, BLS and Kerr effect studies of Ga⁺ irradiated Pt/Co/Pt trilayers. Joint European Magnetic Symposia (JEMS 2013), Rhodes, Greece, August 25-30, 2013.
3. **N. Tahir**, R. Gieniusz, et.al, Dynamic behavior of magnetic regions formed due to chemical disorder. Abstracts of IEEE International Magnetics Conference, INTERMAG Europe May 4-11(2014), Dresden, Germany.
4. M. Jakubowski, Z. Kurant, **N. Tahir**, et.al, FIB nano-fabrication of the Pt/Co/Pt magnonic crystal. 14th European Conference Physics of Magnetism 2014 (PM'14), June 23-27 (2014).
5. **N. Tahir**, R. Gieniusz, et.al, Study of Static and Dynamic of Magnetization in Ne⁺ irradiated Fe₆₀Al₄₀ thin Films, 22th International Colloquium on Magnetic Films and Surfaces (ICMFS2015) July 12-17, Krakow, Poland.
6. **N. Tahir**, N, R. Gienius, et.al, Collective spin wave excitations in the square lattice magnonic Wave-like Py Structures. 22th International Colloquium on Magnetic Films and Surfaces (ICMFS2015) July 12-17, Krakow, Poland.
7. **N. Tahir**, R. Gieniusz, et.al, Spin wave excitations in periodic arrays of wave-like Py structures, 4th International workshop on Magnonics: From Fundamentals to Applications, August 02-06, Seon, Germany. (**Oral presentation**).

(Other Topics)

1. M. S. Rafique, M. K. Rahman, M. Imran, K. Waqas, **N. Tahir**, S. Ahmad, M. Shahbaz Anwar, "Laser Irradiation Effect on Materials", Proceeding of First International conference on Frontiers of Advanced Engineering Materials at Lahore, PP. 458–465, 2004.

Acknowledgements

I am sincerely thankful to everyone who directly or indirectly contributed to the realization of dream of my family. My time here (Bialystok) has been a truly rewarding experience, and is a result of the support and guidance of several people during the course of my research. I would like to take this opportunity to thank all of them at this juncture.

First and foremost, I am grateful to Prof. dr. hab. Andrzej Maziewski for showing trust in me and giving me opportunity to be a part of this team. His guidance and supervision have been like burning torches in my hands to enlighten the path of my Ph.D journey. His impressive knowledge which helped to solve numerous problems and often contributed to a better comprehension of many physical concepts. Moreover, his proofreads are greatly acknowledged. Thanks for helping me to prepare my results, organize my research activities and interpretation of the results. Thanks you!

I am grateful to my supervisor dr. hab. Ryszard Gieniusz for his guidance and giving a fantastic opportunity to work on Brillouin Light Scattering, and FMR setups. Thanks to him for proof reading of my thesis and valuable suggestions. I highly appreciated his great efforts. Thanks again!

I am thankful to dr. hab. Marek Kisielewski prof. UwB, and dr. hab. Andrzej Stupakiewicz prof. UwB, for their great encouragement and moral support during my stay in the lab. Thanks!

I would extend my gratitude to dr. hab. Maria Tekielak prof. UwB for her great support to help me for Kerr microscopy measurements. I am very much appreciated mgr Wojciech Dobrogowski, for taking care of my computer issues, and his support for writing lab-view to study the magnetization reversal mechanisms. I have enjoyed my stay in the lab due to the presence of colleagues who have been good friends and pillars of support throughout these years. Thanks to dr. Iosif Sveklo, dr Zbigniew Kurant, dr Jan Kisielewski, dr Piotr Mazalski, dr. Vladimir Bessonov, Sergey Parchenko, Krzysztof Szerenos. Special, thanks to Urszula Guzowska for her great help in every matter we have faced in Bialystok, without her presence life in Poland may not be easy. Again thanks for being friendly and keeping cooperative atmosphere within the team.

I would like to extend my thanks to our collaborators and all coauthors of my publications. Thanks to Prof. J. Fassbender, dr. Rantej Bali and their team for fabricating FeAl samples. I appreciated their timely response during the ping pong to finalize the manuscripts.

This thesis would not have possible without the analytical support. Thanks to Prof. Maciej Krawczyk, Mateusz Zelent, Jaroslaw Klos, S. Mamica from Adam Mickiewicz University Poznan for their great theoretical supports to interpret and model experimental results. The whole team has been exceptionally kind.

Special thanks to Prof. A. O. Adeyeye and his team for fabricating high quality nanopatterns of Py and scientific discussions. His response has been really fast.

I am really thankful to other team members prof. nzw. dr hab. Andrzej Wawro, and mgr inż. Marcin Jakubowski from IFPAN, Warsaw for preparation of Pt/Co/Pt samples and fruitful discussions. Their hospitality has been great since very first day of our arrival to Poland.

I would like to thanks to dr. Tomasz Wojciechowski from IFPAN, Warsaw for his support in scanning electron microscopy measurements.

I would like to extend my gratitude to my all family for their prayers and unquestioning support (especially my mother and father).

At the last but not least, I am really thankful to my wife (Faiqa), my sons (Muhammd Ashhar Khan, and Muhammad Razan Khan) for their love, great moral support during this time. They always have been a source of encouragement for me whenever I felt down.

At the end I would like to acknowledge the financial support for this work by Foundation for Polish Science within the Team Programme co-financed by the EU European Regional Development Fund, OPIE 2007-2013.

Thanks again to all.

Nadeem Tahir

30 October 2015,

Bialystok.